

POURIANEJAD, SAJEDEH, Ph.D. Studying of Two-Dimensional Interfacial Interactions. (2022)

Directed by Dr. Tetyana Ignatova. 89 pp.

Two-dimensional (2D) materials and their van der Waals (vdW) heterojunctions offer the opportunity to combine layers with different opto-electrical properties to advance novel functional materials. Heterostructures comprised of graphene and 2D MoS<sub>2</sub> is a realized contender for a wide range of optoelectronic devices. This is owing to graphene's high transparency and configurable Fermi level, as well as the tunability of 2D MoS<sub>2</sub>'s photoluminescent (PL) properties. In this dissertation, we investigated 2D interfacial interactions such as: graphene in contact with different polymers, 2D MoS<sub>2</sub> with external doping, and the lateral charge redistribution created by the graphene - MoS<sub>2</sub> heterojunction. For this purpose, we studied the adhesion properties of graphene and its transfer support polymer, which led to the development of a modified polymer support. In addition, we fabricated graphene and 2D MoS<sub>2</sub> heterostructures and evaluated the magnitude and direction of the internal charge transfer (i.e., electron or hole). Furthermore, we studied the influence of external doping on 2D MoS<sub>2</sub>, which resulted in PL enhancement. Moreover, we examined local nanometer scale non-uniformities of graphene-MoS<sub>2</sub> heterostructures, which led to the development of a multimodal biosensor for detecting doxorubicin (DOX). The optical and electronic structure of the materials, as well as doping and strain configuration, were probed by Confocal Raman microscopy and photoluminescence. The surface morphology of 2D MoS<sub>2</sub> and graphene were imaged by scanning electron microscopy (SEM). To correlate the work function difference to charge-related phenomena, Kelvin probe force microscopy (KPFM) was carried out. We quantified the effect of local charge and defect distribution on the characteristics of 2D materials and this led to the fabrication of a device that has biosensing applications. Such 2D optical devices have the potential to become ultra-small sensing platforms, making major contributions to medical diagnosis and treatment; pollution control; and safety control.

STUDYING OF TWO-DIMENSIONAL INTERFACIAL INTERACTIONS

by

Sajedeh Pourianejad

A Dissertation Submitted to  
the Faculty of The Graduate School at  
The University of North Carolina at Greensboro  
in Partial Fulfillment  
of the Requirements for the Degree  
Doctor of Philosophy

Greensboro  
2022

Approved by

---

Committee Chair

*Dedicated to my dear Mom and Dad who taught me to go after my dreams, be patient and never give up.*

APPROVAL PAGE

This dissertation written by Sajedah Pourianejad has been approved by the following committee of the Faculty of The Graduate School at The University of North Carolina at Greensboro.

Committee Chair \_\_\_\_\_  
Tetyana Ignatova

Committee Members \_\_\_\_\_  
Joseph Starobin

\_\_\_\_\_  
Jianjun Wei

\_\_\_\_\_  
Dennis LaJeunesse

\_\_\_\_\_  
Date of Acceptance by Committee

\_\_\_\_\_  
Date of Final Oral Examination

## ACKNOWLEDGMENTS

I acknowledge the Joint School of Nanoscience and Nanoengineering (JSNN), a member of the Southeastern Nanotechnology Infrastructure Corridor (SENIC) and National Nanotechnology Coordinated Infrastructure (NNCI), which is supported by the National Science Foundation (Grant ECCS-1542174). Home written code developed in our group by Kirby Schmidt and Anthony Trofe for advanced Raman map analysis. DFT calculation has been carried out by Jared Averitt. MoS<sub>2</sub> samples have been synthesized by Dr. Frederick Aryeetey in Dr. Shyam Aravamudhana's research group.

# Contents

|          |   |           |
|----------|---|-----------|
| <b>1</b> | <b>Introduction</b>   | <b>1</b>  |
| 1.1      | The Advent of Two-Dimensional Materials . . . . .                               | 1         |
| 1.2      | General Goals of Research . . . . .   | 2         |
| <b>2</b> | <b>Background</b>   | <b>3</b>  |
| 2.1      | Graphene . . . . .  | 3         |
| 2.1.1    | Properties . . . . .  | 3         |
| 2.1.2    | Synthesis . . . . .   | 6         |
| 2.2      | Two-dimensional MoS <sub>2</sub> . . . . .                                      | 7         |
| 2.2.1    | Properties . . . . .  | 7         |
| 2.2.2    | Synthesis . . . . .   | 10        |
| 2.3      | 2D device fabrication and associated challenges . . . . .                       | 11        |
| 2.4      | Organization of 2D materials in Van der Waals heterostuctures . . . . .         | 12        |
| 2.5      | Applications of two-dimensional materials and their heterostructures . . . . .  | 14        |
| <b>3</b> | <b>Aim one: Advancement of two-dimensional materials transfer methods</b>       | <b>17</b> |
| 3.1      | Task one: Dry transfer method . . . . .   | 17        |
| 3.1.1    | Materials and methods . . . . .   | 18        |
| 3.1.2    | Characterization: . . . . .   | 19        |
| 3.1.3    | Results and Discussion . . . . .  | 19        |
| 3.1.4    | Conclusions . . . . .   | 20        |
| 3.1.5    | Recommendations for Future research . . . . .                                   | 20        |
| 3.2      | Task two: Novel approach for PMMA-assisted graphene transfer . . . . .          | 20        |
| 3.2.1    | Materials and methods . . . . .   | 21        |
| 3.2.2    | Characterization . . . . .  | 22        |
| 3.2.3    | Results and Discussion . . . . .  | 23        |
| 3.2.4    | Conclusions . . . . .   | 28        |
| 3.2.5    | Recommendations for Future research . . . . .                                   | 28        |
| 3.3      | Task three: Optimization of interaction on graphene-polymer interface . . . . . | 28        |
| 3.3.1    | Method and Materials . . . . .  | 32        |

|          |  |           |
|----------|--|-----------|
| 3.3.2    | Characterization . . . . .   | 34        |
| 3.3.3    | Results and discussions: . . . . .   | 34        |
| 3.3.4    | Conclusions . . . . .  | 43        |
| 3.3.5    | Recommendations for Future research . . . . .  | 44        |
| <b>4</b> | <b>Aim two: Internal charge doping effects in vdW hybrid structures</b>  | <b>45</b> |
| 4.1      | Task one: Fabrication of graphene-MoS <sub>2</sub> vdW hybrids. . . . .  | 45        |
| 4.1.1    | Method and Materials . . . . .   | 45        |
| 4.1.2    | Characterization: . . . . .  | 47        |
| 4.1.3    | Results and Discussions . . . . .  | 47        |
| 4.1.4    | Conclusions . . . . .  | 50        |
| 4.1.5    | Recommendations for Future Research . . . . .  | 50        |
| 4.2      | Task two: Investigating internal charge doping effect in vdW hybrid structures. . . . .                          | 50        |
| 4.2.1    | Method . . . . .   | 50        |
| 4.2.2    | Results and Discussion . . . . .   | 53        |
| 4.2.3    | Conclusions . . . . .  | 57        |
| 4.2.4    | Recommendations for Future research . . . . .  | 58        |
| <b>5</b> | <b>Aim three: External doping on two dimensional interface</b>   | <b>59</b> |
| 5.1      | Task one: Study the chemical doping and photo etching interaction in 2D MoS <sub>2</sub> . . . . .               | 59        |
| 5.1.1    | Materials and Methods . . . . .  | 61        |
| 5.1.2    | Characterizations . . . . .  | 61        |
| 5.1.3    | Results and Discussion . . . . .   | 61        |
| 5.1.4    | Conclusions . . . . .  | 65        |
| 5.1.5    | Recommendations for Future research . . . . .  | 66        |
| 5.2      | Task two: Studying 2D vdw interaction with external doping and developing design of nanoscale biosensor. . . . . | 66        |
| 5.2.1    | Materials and Methods . . . . .  | 67        |
| 5.2.2    | Characterization . . . . .   | 67        |
| 5.2.3    | Results and Discussion . . . . .   | 67        |
| 5.2.4    | Conclusions . . . . .  | 72        |
| 5.2.5    | Recommendations for Future research . . . . .  | 73        |

# List of Tables

|     |   |    |
|-----|---|----|
| 3.1 | Summary of topography properties of the samples . . . . .   | 39 |
| 3.2 | Contact angle of water droplet on Graphene, PMMA, PCPs/PMMA 1:6, PCPs/PMMA 1:4 . . . . .            | 39 |
| 3.3 | Surface tension and surface energy, work adhesion between G-polymer                                 | 40 |
| 3.4 | Hydrogen bond length of PCPs on graphene (Fig. 3.16 (a)) . . . . .                                  | 42 |
| 3.5 | Hydrogen bond length of PMMA Dimer on graphene (Fig. 3.16 (b)) .                                    | 42 |
| 3.6 | Hydrogen bond length of PMMA Dimer and PCPs on graphene (Fig. 3.16 (c)) . . . . .                   | 43 |
| 3.7 | Hydrogen bond length between PCPs and PMMA Dimer (Fig. 3.16 (c))                                    | 43 |
| 3.8 | Hydrogen bond length between PCPs and PMMA Dimer (Fig. 3.18) .                                      | 43 |
| 4.1 | Sample preparation and abbreviation. . . . .  | 46 |
| 5.1 | CPD of as-grown and doped Mos <sub>2</sub> flakes . . . . .   | 63 |
| 5.2 | CPD of as-grown and doped Mos <sub>2</sub> flakes . . . . .   | 64 |
| 5.3 | The PL fit parameters for Fig. 5.4 (d): upper/lower row corresponds to PL with/without DOX. . . . . | 68 |
| 5.4 | Measured GERS enhancement factors for major fingerprint Raman lines of DOX. . . . .                 | 68 |

# List of Figures

|     |   |    |
|-----|---|----|
| 2.1 | Graphene lattice and band structure: a) hexagonal honeycomb lattice of graphene, b) binding between the carbon atoms in the graphene lattice, c) the triangular sublattices A and B, d) the first hexagonal Brillouin zone exhibiting two inequivalent groups of Dirac points, and e) the energy-momentum spectrum of the graphene band structure. Note the rotation of k-axes with respect to (d) and (f) Raman spectroscopy of Graphene. Reprinted with permission from [1] . . . . . | 5  |
| 2.2 | Optical image of CVD grown graphene on Cu foil (Ignatova, T., unpublished). . . . .   | 7  |
| 2.3 | (a) MoS <sub>2</sub> band structures, crystals and the crystal structure of monolayer MoS <sub>2</sub> showing a layer of molybdenum atoms (blue) sandwiched between two layers of sulfur atoms (yellow). (b) Band structure diagram of (left) bulk and (right) monolayer MoS <sub>2</sub> showing the crossover from indirect to direct bandgap accompanied by a widening of the bandgap. (c) 2H crystal structure of MoS <sub>2</sub> . Reprinted with permission from [2,3]          | 9  |
| 2.4 | Helium Ion Microscopy images of MoS <sub>2</sub> . The scale bars in (a and d) are 5 μm, in (b) 50 μm, in (c) 500 nm [4]. . . . .   | 11 |
| 2.5 | (a) Schematic of a two-terminal device with the graphene/MoS <sub>2</sub> heterostructure with graphite as the electrical contact [5]. (b) Schematic image of graphene /WS <sub>2</sub> /MoS <sub>2</sub> /graphene heterostructure photodetector.(i) the side view and (ii) the top view [6]. . . . .  | 15 |
| 3.1 | Schematic of electrochemical transfer process with H <sub>2</sub> bubbles. . . . .  | 19 |
| 3.2 | (a) Optical image and (b) SEM image of graphene transferred from Cu foil to SiO <sub>2</sub> /Si by polysiloxane film. (c) graphene transferred by PMMA. (d) Raman spectroscopy of graphene transferred from Cu foil to SiO <sub>2</sub> /Si by dry method.scale bars are 900μm for (a) and 5μm (b) and (c). . . . .  | 20 |

|      |   |    |
|------|---|----|
| 3.3  | Schematic diagram of Soxhlet-assisted graphene transfer. (a) Graphene on Cu foil, (b) Graphene spin-coated with PMMA, (c) Cu foil removal by electrochemical method and subsequent transfer on SiO <sub>2</sub> /Si substrate, (d) Graphene attached on SiO <sub>2</sub> /Si-PMMA composite, (e) Soxhlet apparatus setup for PMMA removal, (f) Ultra-clean graphene on target substrate. . . . .  | 22 |
| 3.4  | Optical microscopy images of graphene films from (a) conventional transfer and (b) Soxhlet assisted technique. . . . .  | 23 |
| 3.5  | Micro-Raman spectroscopy scans in X- and Y-directions on the graphene transferred by conventional and Soxhlet methods. . . . .  | 24 |
| 3.6  | Width maps of fitted peaks obtained from Raman characterization (10×10 μm <sup>2</sup> ) of graphene transferred with (a,b,c) conventional PMMA method; (d,e,f) Soxhlet assisted PMMA method. . . . .   | 25 |
| 3.7  | Characterization of transferred graphene films on SiO <sub>2</sub> /Si substrates. SEM images of (a) Conventional transfer method. (b) Soxhlet transfer method. Color framed insets represent zoomed areas. AFM profile of (c) Conventional transfer method. (d) Soxhlet transfer method, scale bare is 1μm. Inset: The AFM line profile graph for both transfer techniques.  | 26 |
| 3.8  | Corresponding maps of plotted results of Raman characterization (10×10 μm <sup>2</sup> ) of graphene transferred with (a ,b, c) conventional PMMA method; (d, e, f) Soxhlet assisted PMMA method. . . . .   | 27 |
| 3.9  | (a) Correlation map of the Raman G and 2D peak positions of graphene transferred with conventional PMMA technique (blue) and Soxhlet assisted PMMA technique (red); (b), (c) Histogram of 2D/G ratio with the same color code indicating the sample quality in general. (d), (e) Histogram of D/G ratio with the same color code as a signature of defect amount. . . . .   | 27 |
| 3.10 | a) Surface tension, b) Adhesion energy, c) Contact angle . . . . .  | 29 |
| 3.11 | Graphene transfer schematic . . . . .   | 32 |
| 3.12 | Chemical structures, formula and isosurface of electron density overlaid with color map of electric potential from DFT computations. Chemical structures and formula of a) PMMA and b) PCPs. Isosurfaces of c) PMMA and d) PCPs. The shape and size of the surface show electron density cloud of existence up to 95% probability. Red regions of isosurfaces represent most electro-negative regions while blue regions represent relatively electro depleted regions and green regions having a neutral charge. Carbon atoms in grey, hydrogen atoms in white and oxygen atoms in red. Graphene structure e) with 54 sp <sup>2</sup> hybridized carbon atoms. . . . . | 33 |

|      |  |    |
|------|--|----|
| 3.13 | SEM images of graphene transferred by (a)PMMA, (b)PCPs/PMMA 1:6, (c)PCPs/PMMA 1:4, (d)PCPs/PMMA 1:2 . . . . .  | 35 |
| 3.14 | Raman map for doping of (a) graphene transferred by PMMA and (b) graphene transferred by 1:4. Raman map for strain of (c) graphene transferred by PMMA and (d) graphene transferred by 1:4. (e) 2D center vs Width plot. (f) correlation plot of G peak vs 2D peak. . . .                      | 36 |
| 3.15 | Decreasing of polymer residues in graphene transferred because of using mixed polymer of PCPs/PMMA instead of PMMA. SEM (a and b), AFM (c and d) and line profile of samples: S1 and S2, respectively. scale bars are 2 $\mu\text{m}$ and 1 $\mu\text{m}$ in SEM and AFM images, respectively. | 38 |
| 3.16 | Contact angle of DI water droplet on (a) graphene, (b) PMMA film, (c) PCPs/PMMA 1:6 and (d) PCPs/PMMA 1:4. . . . .   | 39 |
| 3.17 | Attachment of PCPs and PMMA on hexagonal graphene flake with hydrogen-functionalized edges. Carbon atoms in grey, hydrogen atoms in white and oxygen atoms in red . . . . .  | 41 |
| 3.18 | Optimized geometry according to DFT calculations of PMMA and PCPs. Carbon atoms in grey, hydrogen atoms in white and oxygen atoms in red. . . . .  | 42 |
| 4.1  | (a) and (b) Optical and SEM image of S1, respectively, and Raman spectroscopy of graphene (c) before and (d) after transfer on MoS <sub>2</sub> . . .  | 47 |
| 4.2  | SEM images of S2: (a) before transfer of graphene, (b) after transfer of graphene, and Raman spectroscopy of S2: (c) MoS <sub>2</sub> , (d) MoS <sub>2</sub> covered by graphene and, (e) graphene and graphene on MoS <sub>2</sub> . . . . .  | 48 |
| 4.3  | (a) SEM image and (b) Raman spectroscopy of S3. . . . .  | 49 |
| 4.4  | SEM images of S4 (a) before transferring graphene (b) after transferring graphene. (c) and (d) are Raman spectroscopy of MoS <sub>2</sub> before and after graphene coverage. . . . .  | 49 |
| 4.5  | KPFM of Graphene-SiO <sub>2</sub> /Si (a), electronic band structure energy diagram of graphene (c), KPFM of MoS <sub>2</sub> -SiO <sub>2</sub> /Si (d), and electronic band structure energy diagram of MoS <sub>2</sub> . . . . .  | 54 |
| 4.6  | SEM image (a), AFM map (b), and KPFM map (c) of Graphene-MoS <sub>2</sub> -SiO <sub>2</sub> /Si. Corresponding line profile of AFM and KPFM (d) and (e), respectively. Electronic band structure energy diagram of heterostructure of graphene and MoS <sub>2</sub> (f). . . . .               | 55 |
| 4.7  | SEM image (a), AFM map (b), and KPFM map (c) of Graphene-MoS <sub>2</sub> -SiO <sub>2</sub> /Si. Corresponding line profile of AFM and KPFM (d) and (e), respectively . . . . .  | 57 |

|     |  |    |
|-----|--|----|
| 5.1 | (a) Scanning Electron Microscopy image (SEM) of MoS <sub>2</sub> sample (b) AFM and height profile lines (c) KPFM surface potential map of sample as-prepared and CPD profile lines (d) KPFM surface potential map after chemical doping and CPD profile lines. . . . .  | 62 |
| 5.2 | (a) SEM of MoS <sub>2</sub> sample. (b) KPFM map of as-prepared sample. (c) KPFM surface potential map with sample after both photodoping (laser illumination) chemically dopant treatments. . . . .   | 64 |
| 5.3 | (a) Photoluminescence (PL) spectral map of as-prepared sample (b) after photo-chemical doping. (c) PL spectra showing PL intensity before (d) after photo-chemical doping. . . . .   | 65 |
| 5.4 | Multiplexed detection of doxorubicin drug. (a) Schematics of multi-mode detection by the combination of MoS <sub>2</sub> photoluminescence, DOX GERS, and Raman shift of monolayer graphene. (b) GERS signal of DOX/monolayer graphene (red), vs. reference Raman spectra of DOX/DMSO solution (cyan) and monolayer graphene (gray); red (cyan) arrows mark DOX (DMSO) lines. (c) Modulation of MoS <sub>2</sub> PL spectrum: with DOX (red) and w/o DOX (cyan); inset shows DOX molecular structure. (d) Fitting of measured PL spectra from (c): A/B-exciton and trion (A <sup>-</sup> ) lines are shown; modulation of peak position ( $\Delta\omega$ ) and intensity ( $\Delta P$ ) are indicated using A-exciton fit; inset shows the schematics of optical subbands of MoS <sub>2</sub> . (e-f) Typical Raman spectra of monolayer graphene: with DOX (red) and before incubation (blue); G- and 2D-line intensities were normalized to unity. (g-h) Correlation plots and partial distribution functions for peak position and width for G- and 2D-lines, measured locally, at diffraction limited spots across the sample; same color code as in (e-f); clear line red-shift and broadening are detected with DOX. . . . . | 70 |
| 5.5 | Stability test of MoS <sub>2</sub> /graphene vertical heterostructure. SEM (a,e) and sSNOM (b-d,f-h) images of two MoS <sub>2</sub> islands, randomly selected, coated with monolayer graphene. The island (a) shows nearly zero degradation after 242 days in ambient – from (b) to (c), neither after 705 days – from (b) to (d); the island (e) was selected near a tear in monolayer graphene and shows (g) partial oxidation near the central micro-crystallite of molybdenum after 242 days, followed by (h) almost complete oxidation of MoS <sub>2</sub> surface after 705 days. All scale bars are 1 $\mu\text{m}$ . . . . .  | 71 |

5.6 Correlation of monolayer graphene work function data with sSNOM optical surface impedance. Aligned maps for (a) KPFM and (b) sSNOM (4th harmonic) amplitude. (c) Cross section profiles across the MoS<sub>2</sub> area (KPFM, red and sSNOM, pink) vs. monolayer graphene reference (KPFM, gray), taken along the lines of the same color in (a-b). . . . . 72

# Chapter 1

## Introduction

### 1.1 The Advent of Two-Dimensional Materials

Since the discovery of graphene, and advent of other two-dimensional (2D) layered materials, new perspectives have prompted intense research and significant advances, paving the way for applications in electronics, optoelectronics, photonics, and photovoltaics [7]. 2D materials have relatively inexpensive fabrication procedures, can be integrated with bulk and other 2D materials, and exhibit new physical and chemical properties, which make them unique and promising material [8]. Electrically, 2D materials can exist in the form of insulators (e.g. hBN), semiconductors (e.g. MoS<sub>2</sub> or black phosphorus), semimetals (e.g. graphene or TiS<sub>2</sub>), metals (e.g. VSe<sub>2</sub> or PtTe<sub>2</sub>), and superconductors (e.g. NbSe<sub>2</sub> or TaS<sub>2</sub>) [9].

Stacking of different 2D materials fabricates vertical heterostructures, in which each layer weakly bounds to neighboring layers by van der waals (VdW) force. Heterostructures offer different proprieties compared with the original layers. One of the reasons behind this difference is the possibility of charge redistribution between neighboring layers, leading to tinning the original electrical structure [7, 10]. Study of the 2D materials' interaction with other surfaces, which they are in contact with, is of utmost importance due to achieving a successful fabrication and also tailoring the properties as expected. As one of the common method to synthesis graphene and other 2D materials is chemical vapor deposition (CVD) on metal substrate such as Cu and Ni, transferring the 2D material from growth substrate onto target substrate is vital. A successful transfer wouldn't occur unless we have the knowledge of how 2D materials interact with other materials during transferring. In fact, tailoring the adhesion energy at 2D materials' interface can avoid defect formation in the transfer process.

Moreover, studying the mechanism of the charge redistribution of 2D materials in heterostructures gives the knowledge of how the Fermi level shifts and allows one to determine the energy band alignment between materials, resulting in tailoring

the properties of the combination of the layers. Recently, the area of 2D-based biosensors exhibits a new approach to detect analyte species without the use of label dyes (label-free detection) [11, 12]. In [13], MoS<sub>2</sub> layers are employed to enhance the light absorption providing additional quant of energy for effective charge transfer, while monolayer graphene serves as biorecognition component capturing the target biomolecule through *pi*-stacking force. Stacking the monolayer graphene on MoS<sub>2</sub> allows one to exploit the unique features of these two layers at the same time in graphene/MoS<sub>2</sub> heterostructures [14, 15].

## 1.2 General Goals of Research

In 2D materials, the extremely high surface-area to volume ratio increases the possibility of the interaction with the environment, which creates the opportunity to improve their properties. This research aims to study the two dimension interfacial interaction and introduce novel methods to the fabrication process. It will result in clean 2D materials and explore how the structural modifications effect the electronic structure of 2D vdW materials. In fact, the interaction between two layers in vdW materials could turn into the internal charge doping, resulting in the work function modulation. The capability to tune the work function through doping will provide flexibility in 2D device design. This dissertation includes three aims:

- Aim one: Advancement of two-dimensional materials transfer methods

Task one: Dry transfer method

Task two: Novel approach for PMMA-assisted graphene transfer

Task three: Optimization of interaction on graphene-polymer interface

- Aim two: Internal charge doping effects in vdW hybrid structures.

Task one: Fabrication of graphene-MoS<sub>2</sub> vdW hybrids.

Task two: Investigating internal charge doping effect in vdW hybrid structures.

- Aim three: External doping on two dimensional interface

Task one: Study the chemical doping and photo etching in 2D MoS<sub>2</sub>.

Task two: Studying 2D vdw interaction with external doping and developing design of nanoscale biosensor.

# Chapter 2

## Background

### 2.1 Graphene

#### 2.1.1 Properties

Graphene is an allotrope of carbon arranged in a (2D) hexagonal lattice (Fig. 2.1 (a)) and the first real two-dimensional material isolated from graphite [16]. Each  $sp^2$  hybridized carbon strongly connects to the three nearest neighbors with  $\sigma$  bonds to make graphene the strongest material ever. While, the overlapping of the unhybridized p orbital of two adjacent carbons forms  $\pi$  bonds (Fig. 2.1 (b)). Bravais lattice of graphene consists of two atoms per unit cell as presented in Fig. 2.1 (c). Here,  $a_1$  and  $a_2$  are the lattice vectors:  $a_1 = a/2(3, \sqrt{3})$ ,  $a_2 = a/2(3, -\sqrt{3})$ , and  $a \approx 1.42$  is the distance between carbon atoms. In the reciprocal lattice (Fig. 2.1 (c)), the vectors are  $b_1 = 2\pi/3a(1, \sqrt{3})$  and  $b_2 = 2\pi/3a(1, -\sqrt{3})$  which originated at the  $\Gamma$  point; the center of the first Brillouin zone of graphene. The two points K and K' are placed at the corners of the graphene Brillouin zone which name the Dirac point (Fig. 2.1 (e)). The valence band and conduction band meet each other at the Dirac point, and they are technically known as  $\pi$  and  $\pi^*$  bands, respectively. Among four valence electrons of C atom, the  $\pi$  electron can freely move from valence band to conduction band. The symmetry of the honeycomb lattice cause electrons in graphene to obey the Dirac's equation instead of Schrodinger's. describing relativistic fermions (possessing spin of  $s = \frac{1}{2}$ ). As a result, the electronic band structure of graphen exhibits the *linear dispersion relation*

$$E = \hbar k \sqrt{v_F^2} \quad (2.1)$$

where  $\hbar$  is reduced Planck constant ( $\sim 6.582 \times 10^{-16}$  eV.s),  $k$  is wavevector and  $v_F$  is Fermi velocity,  $v_F \approx c/300$  (m/s), in which  $c$  is the speed of light (Fig. 2.1 (e)). Hence, the suspended graphene (non-doped, non-strained) exhibits extremely high charge carrier mobility ( $(2 \times 10^5 \text{ cm}^2/\text{V} \cdot \text{s})$ ) at room temperature [17]. The

first evidence of massless fermions in graphene was presented in magneto-transport measurements.

The charge carrier concentration ( $n(E)$ ) in graphene can be tuned continuously from electrons to holes up to a concentration of  $n = 10^{13} \text{ cm}^{-2}$ , while the mobility parameter is as high as  $20000 \text{ cm}^2/\text{V}\cdot\text{s}$ . In contrast, some semiconductors show high mobility for only bulk undoped materials and mobility is critically decreased with doping. It makes graphene a perfect material for ambipolar field effect transistor applications [18].

$$n(E)\Big|_{K,K'} = \frac{2|E|}{\pi\hbar^2v_F^2} \quad (2.2)$$

At the Dirac point,  $E = 0$  leads to  $n(E)=0$ .

In the near-infrared and visible wavelengths ranges, the interaction of light and undoped graphene leads to inducing interband electronic transitions. Therefore, the conductivity ( $\sigma$ ) of graphene is independent of frequency ( $\omega$ ) of light and temperature (T) in the proximity of the Dirac point:

$$\sigma(\omega)\Big|_{T\rightarrow 0} = \frac{\pi e^2}{2\hbar} \quad (2.3)$$

where  $e$  is the electron charge. As a result the absorption of graphene is  $A(\omega) = \frac{4\pi}{c}\sigma(\omega) \sim 2.3\%$

Graphene transparency is  $\sim 97.8\%$ , the unusual graphene property makes it visible while laying on a substrate [19].

Inelastic scattering of the incident light from optical phonon, quantized modes of lattice vibrations, (Raman scattering) in graphene resulted in multiple peaks. The G ( $1580 \text{ cm}^{-1}$ ) peak in the Raman spectrum is attributed to the doubly degenerate Raman active optical vibration ( $E_{2g}$ ) at ( $\Gamma$ ) in the center of Brillouin zone. The second order double resonance links the two high symmetry points K and K' at the corners of the Brillouin zone, attributing to 2D peak ( $2690 \text{ cm}^{-1}$ ) (Fig. 2.1 (f)). D peak ( $1350 \text{ cm}^{-1}$ ) is related to Out of plane vibration  $sp^2$  hybridized carbon is silent due to the symmetry restrictions in graphene but pronounced by appearance of defect. extended defect of defects in a graphene can be estimated from the inter grated intensity ration of D and G bands: higher the value, higher the amount of defects in graphene.

Graphene is considered a semimetal because the cone-shaped conduction and valance band meet each other at Dirac point, making a zero band gap. In suspended graphene, the Fermi level coincides the Dirac point, which is separated from the vacuum level by the work function  $\sim 4.6 \text{ eV}$ .

$$WF = V_{vacuum} - E_{Fermi} \quad (2.4)$$

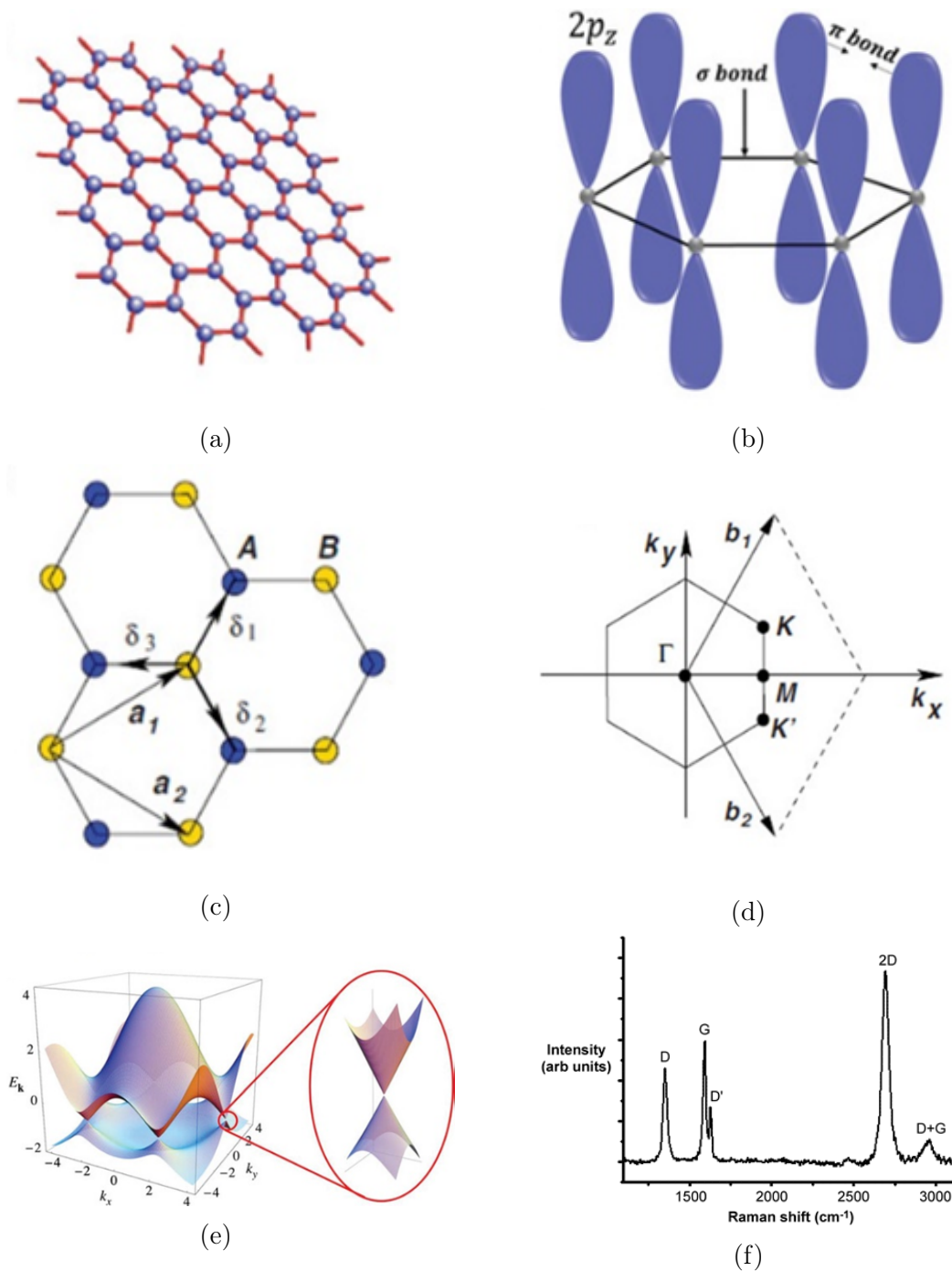


Figure 2.1. Graphene lattice and band structure: a) hexagonal honeycomb lattice of graphene, b) binding between the carbon atoms in the graphene lattice, c) the triangular sublattices A and B, d) the first hexagonal Brillouin zone exhibiting two inequivalent groups of Dirac points, and e) the energy-momentum spectrum of the graphene band structure. Note the rotation of  $k$ -axes with respect to (d) and (f) Raman spectroscopy of Graphene. Reprinted with permission from [1]

Changing the carrier density leads to a shift in the Fermi level, resulting in tuning the work function of graphene. Various methods have been employed to change the carrier density of graphene by external electric field, chemical doping, etc. In fact, p-doping shifts down the Fermi level towards the valence band and increase the work function. While n-doping lifts up the Fermi level towards the conduction band and reduce the work function value. Scanning measurement techniques, such as the Kelvin probe force microscopy (KPFM), are widely used for mapping the surface potential of graphene, containing information about the Fermi level and carrier concentration [20].

### 2.1.2 Synthesis

Mechanical cleaving (exfoliation) of few layers of highly oriented pyrolytic graphite (HOPG) was found to be an easy approach to produce graphene. The relative success caused scientists to introduce other exfoliation methods such as chemical, sonication and ball-milling approaches. However, the very low yield made it not a reliable and cost-effective technique [2]. Chemical vapor deposition (CVD) provides continuous sheet of graphene on transition metal foils, such as copper (Cu) (Fig. 2.2), nickel (Ni), platinum (Pt) and gold (Au). To grow graphene films on Cu foil (25  $\mu\text{m}$  thickness) by CVD method, initially Cu foil is annealed in a furnace under  $\text{H}_2$  gas at  $1000^\circ\text{C}$ . Then the growth of graphene is started by flowing a mixture of hydrocarbon gas such as methane ( $\text{CH}_4$ ) with hydrogen. After creating a continuous layer of graphene the system is cooled down to room temperature [21].

In addition, recently epitaxial graphene growth on silicon carbide (SiC) has gained a great attention as a promising method to obtain reproducible and homogeneous large-area of graphene. In this method with annealing the SiC substrate at temperature  $> 1400^\circ\text{C}$ , SiC decomposes into Si and C; Si partially evaporates and leaves behind the substrate. Then  $\text{sp}^2$  hybridized C leads to form graphene layers on SiC wafer [2, 22].

However, drawbacks of these two methods are: the limited choice of substrate and high vacuum and high temperature, which makes these methods quite expensive. The limited-substrate choice created a new challenge, i.e. transfer of graphene from growth substrates onto target substrates. Thus far, wet chemical and dry chemical techniques have been common methods for transferring epitaxially and CVD grown graphene [23]. In wet process, graphene transfer is directed by etching a metal substrate by solvents, such as iron chloride ( $\text{FeCl}_3$ ), hydrochloric acid (HCl), nitric acid ( $\text{HNO}_3$ ), iron(III) nitrate ( $\text{Fe}(\text{NO}_3)_3$ ) and copper chloride ( $\text{CuCl}_2$ ) or electrochemical bubbling based on direct permeation of H or O ions through the interface of graphene and metal substrate. By contrast in dry method, graphene is transferred by direct delamination technique, using mild heat and pressure combined with mechanical peeling [24].

To prevent the defect formation such as folding, cracking and wrinkling, applying a support layer during transferring of graphene is crucial. We can categorize the graphene transfer methods into 2 groups: transfer with and without polymer support

[25]. In the first method, the most common polymers are poly(methyl methacrylate) (PMMA), poly(lactic acid) (PLA), poly(phthalaldehyde) (PPA), and poly(bisphenol A carbonate) (PC) [26]. Non-Polymer-based graphene transfer includes metal-assisted graphene transfer, small molecules-assisted graphene transfer, hexane assisted graphene transfer, and static charge-based graphene transfer [25].

Therefore, although CVD and epitaxial methods have the potential to grow graphene for industrial applications, more precise studies are required to develop the transfer methods to retain the quality of graphene.

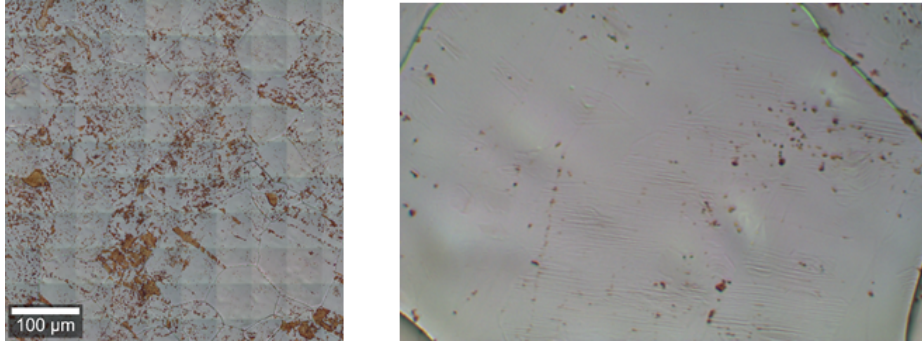


Figure 2.2. Optical image of CVD grown graphene on Cu foil (Ignatova, T., unpublished).

## 2.2 Two-dimensional MoS<sub>2</sub>

### 2.2.1 Properties

Beyond the graphene, 2D transition metal dichalcogenides (TMDCs) materials are the most studied. Their general formula is MX<sub>2</sub> with M, a transition metal (Ti, Zr, Hf, V, Nb, Ta, Mo, W, Tc, Re, Co, Rh, Ir, Ni, Pd, Pt), and X, a chalcogen (S, Se, Te). TMDCs represent a large family of materials including semiconductors, metals and superconductors. 2D semiconductor MoS<sub>2</sub> consists a sublayer of molybdenum (Mo) sandwiched between two sublayer sulfur (S) in a trigonal prismatic symmetry (Fig. 2.3 (a)), for which the unit cell contains S-Mo-S. The layer stacking sequences of 2H-MoS<sub>2</sub> structure is represented as AbA-BaB, in which the lower- and upper-case letters represent Mo and S layers, respectively (Fig. 2.3 (c)). In addition, the lattice constants range from 3.1 Å to 3.7 Å and interlayer spacing is about 6.5 Å [27]. The band structure of MoS<sub>2</sub> shows parabolic dispersion ( $E \propto k^2$ ) in the k-space for the valence and conduction bands [28]. Intrinsic bandgap in 2D MoS<sub>2</sub> changes from an indirect gap of  $E_g \sim 1.3$  eV in bulk to a direct band gap of 1.83 eV in monolayer MoS<sub>2</sub> (Fig. 2.3 (b)). This property results in a remarkable increase ( $\sim$

$10^3 - 10^4$ ) in the photoluminescence efficiency, which is desirable for electronic and opto-electronic applications [7]. The PL in multilayer MoS<sub>2</sub> shows two prominent PL peaks at  $\sim 1.85\text{eV}$  ( $\sim 670\text{ nm}$ ) and  $\sim 1.98\text{ eV}$  ( $\sim 627\text{ nm}$ ), corresponding to the A and B excitonic transitions. Also, negatively charged trion  $A^-$ , consisting of an exciton coupled with one electron, is commonly observed in 2D MoS<sub>2</sub> and has lower binding energy than the exciton. To quantify individual contributions from A and B excitons, PL spectrum can be fitted by three independent Lorentzian peaks (Fig. 2.3 (d)) [29].

The carrier concentration for 2D MoS<sub>2</sub>:

$$n(E) \sim \frac{m^*}{\pi\hbar^2} \quad (2.5)$$

Two vibrational modes of MoS<sub>2</sub> contribute to Raman scattering:  $E_{2g}^1$  ( $\sim 384\text{ cm}^{-1}$ ) due to in-plane vibrations of two S atoms with respect to the Mo atom, and  $A_{1g}$  ( $\sim 404\text{ cm}^{-1}$ ) due to out-of-plane vibrations of S atoms in opposite directions. Both Raman and PL spectra intensities of mono- and few-layer 2D materials depend strongly on their number of layers, the substrate, and internal strain and doping. When the film thickness is increased the position of the  $E_{2g}^1$  mode decreases (red shifts) while the  $A_{1g}$  increases (blue shifts). The  $\Delta$  (distance between  $E_{2g}^1$  and  $A_{1g}$ ) was employed to determine the number of layers so 19, 21, 23, 24 and 26  $\text{cm}^{-1}$  are associated with monolayer, bilayer, trilayer, four layer and bulk MoS<sub>2</sub>, respectively [3] (Fig. 2.3 (e)).

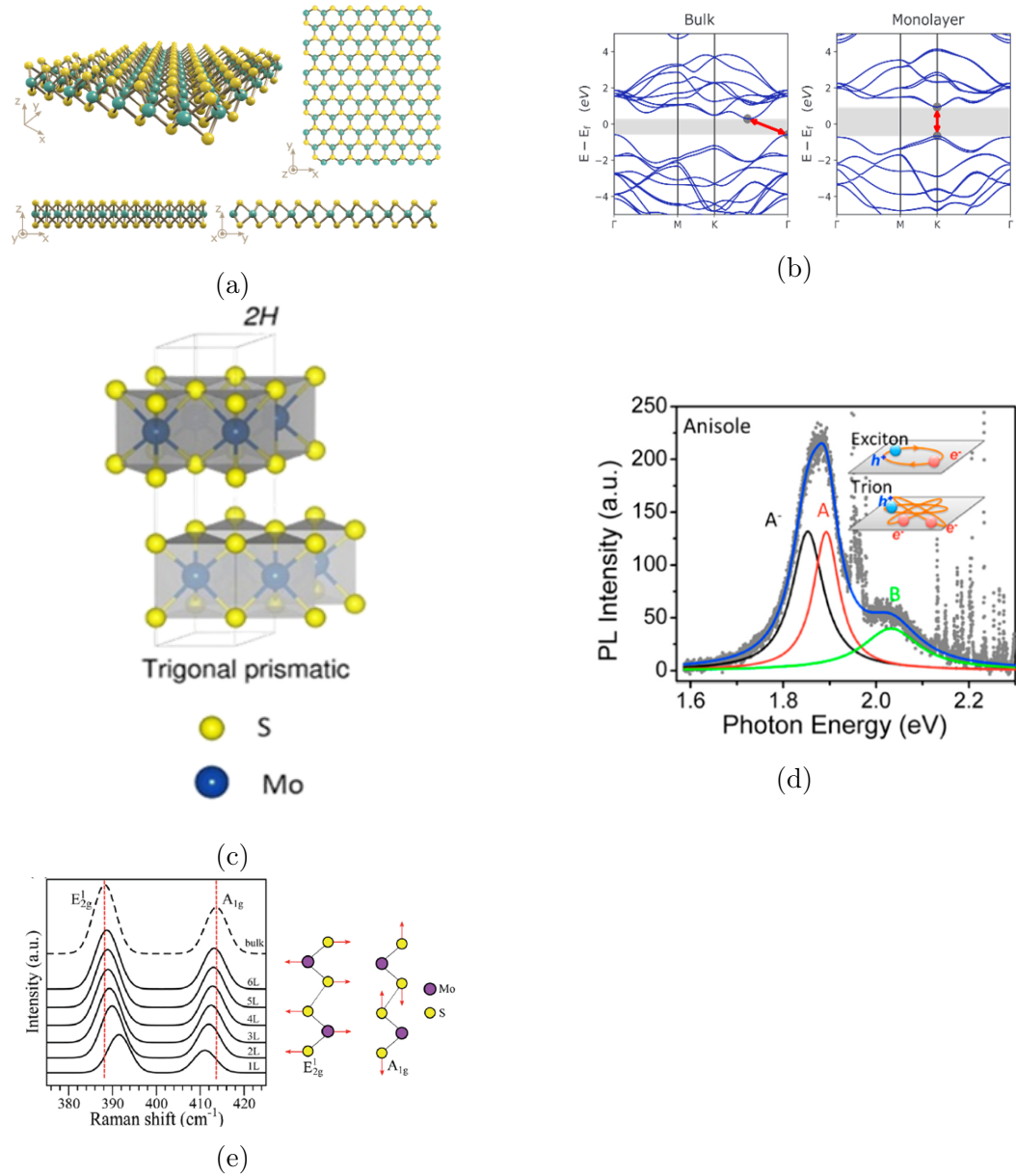


Figure 2.3. (a) MoS<sub>2</sub> band structures, crystals and the crystal structure of monolayer MoS<sub>2</sub> showing a layer of molybdenum atoms (blue) sandwiched between two layers of sulfur atoms (yellow). (b) Band structure diagram of (left) bulk and (right) monolayer MoS<sub>2</sub> showing the crossover from indirect to direct bandgap accompanied by a widening of the bandgap. (c) 2H crystal structure of MoS<sub>2</sub>. Reprinted with permission from [2,3]

### 2.2.2 Synthesis

Many methods have been reported to prepare MoS<sub>2</sub> such as mechanical exfoliation of MoS<sub>2</sub> flake, chemical exfoliation, CVD (sulfurization of Mo based compound or sulfurization of Mo and Mo based oxides), thermal decomposition of (NH<sub>4</sub>)<sub>2</sub>MoS<sub>4</sub> and vapor-solid growth from MoS<sub>2</sub> powder. Despite the great progress in preparation methods, controllable synthesis of 2D TMDCs with a uniform-large scale production remains an open question. Among all synthesis methods, the CVD one is a promising candidate for production of 2D MoS<sub>2</sub> films on a wafer-scale, necessary for practical applications like large scale integrated electronics [30]

In CVD process, 2D MoS<sub>2</sub> is grown under the flow of argon gas in a quartz tube furnace at high temperature. Molybdenum trioxide (MoO<sub>3</sub>) is placed in a high-temperature area of the furnace (600-800°C) and sulfur powder is put in a low-temperature area of furnace. The reaction starts while argon gas continuously flows to protect the atmosphere. After evaporation of two precursors, the sulfur vapor is driven by argon gas through molybdenum source. The reaction of sulfur and molybdenum vapor leads to grow 2D MoS<sub>2</sub> on a substrate, placed upside-down closeby MoO<sub>3</sub>. When the reaction is completed, argon is pumped to cool it to room temperature [31]. The stoichiometric ratio of Molybdenum to sulfur plays a key role in the morphology and shape of 2D MoS<sub>2</sub>: the ratio of 1:1 causes to grow the hexagon shape flakes and an uneven ratio will give rise to triangles, as the SEM images of MoS<sub>2</sub> shown in Fig. 2.4 [4].

The CVD growth of MoS<sub>2</sub> has been mostly performed on specific substrates such as SiO<sub>2</sub>/Si, sapphire and quartz. Hence, to be applicable, transferring MoS<sub>2</sub> is necessary and all of the transfer challenges mentioned for graphene would be considered for MoS<sub>2</sub> as well.

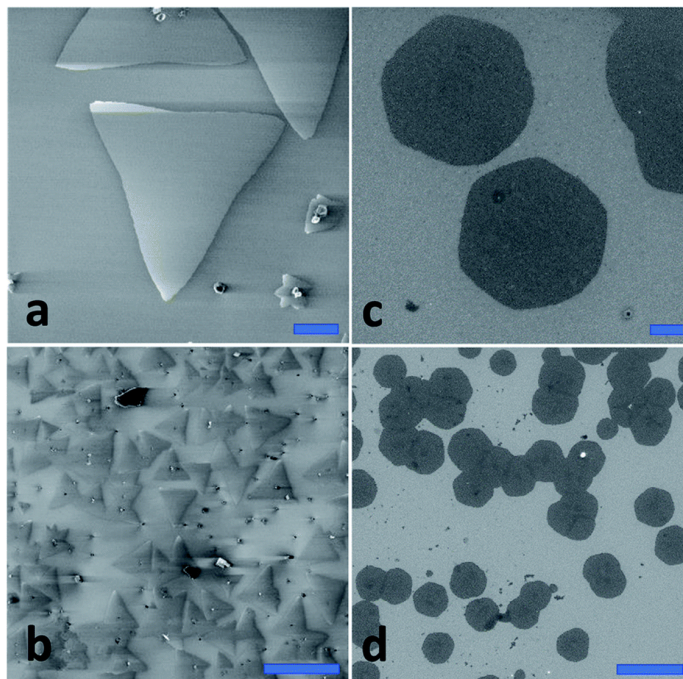


Figure 2.4. Helium Ion Microscopy images of MoS<sub>2</sub>. The scale bars in (a and d) are 5  $\mu\text{m}$ , in (b) 50  $\mu\text{m}$ , in (c) 500 nm [4].

### 2.3 2D device fabrication and associated challenges

PMMA is widely used to support graphene layer and other 2D materials due to its high flexibility, stability, and proper viscosity [32]. However, polymer contamination after cleaning process by organic solvent (e.g., acetone) and graphene wrinkling are two major issues to degrade the quality of transferred graphene [33]. H<sub>2</sub>O/O<sub>2</sub> molecules adsorbed by PMMA lead to p-type doping of graphene [34,35], which adversely affects the carrier mobility and the uniformity of the electrical properties of graphene [36]. The noncovalent binding of COOCH<sub>3</sub> group in PMMA and the network in graphene leads to a strong connection between polymer and 2D material to protect it during transferring [37]. On the other hand, completely removing polymer from 2D material is an open question. To overcome the challenge of removing polymer residues, different methods have been applied such as thermal annealing under forming gas (Ar/H<sub>2</sub>) [38], or vacuum environment, current induced annealing [39], laser cleaning treatment [33], Oxygen (O<sub>2</sub>) plasma treatment [40], and ultraviolet (UV) ozone treatment [41], e-beam treatment (ET) [42].

However, these treatments bring some disadvantages, including increasing the chemical sensitivity and oxidation of graphene surface, leading to more defects and

change of electronic property [43]. Also, graphene comes into closer contact with  $\text{SiO}_2$ , causing of increased coupling between them and leading to inducing heavy hole doping, which subsequently the charge mobility would be degrade [44].

- Contamination and polymer residue removal:

Various transfer techniques have been explored, however the most successful technique is based on organic polymers as the support layer such as PMMA, PC, PVA [26, 45, 46]. Because graphene is only one-atom thick, a supporting layer is crucial for the transfer process to prevent wrinkles and cracks. As a result, preventing transfer-induced defects are very challenging [47, 48]. Kang [47] et al. reported some of the damaged to incomplete removal of PMMA, attributed to the high adhesion potential between PMMA with graphene. Furthermore, impurities in the organic solvents, e.g. acetone and isopropyl alcohol, result in more surface contamination, leading to a negative effect on carrier mobility in graphene [49]. This leads to an unfortunate scenario where repeated washing of the 2D material to achieve more complete removal of the polymer results in greater mechanical damage and contamination by the impurities present in the solvent.

- Modification of support polymer:

During transferring, a polymer layer is required to support graphene against cracking, tearing, and folding. Flexibility and mechanical strength are crucial properties to support the graphene layer. Also, the surface energy between polymer and graphene is of importance to determine the quality of transferred graphene against the residue, cracks, and folds. The adhesion force between elastic solids is proportional to the surface energy according to the modified Hertz theory. The lower the surface energy of the polymer carrier, the weaker the adhesion force with the graphene surface, and thus the easier it will be to remove the polymer by mechanical forces or dissolution, leaving fewer residues [25]. Despite of the fact that PMMA is a flexible and strong polymer film, the high adhesion energy between PMMA and graphene is the main culprit behind the problem of removing the residues. To overcome this issue, Wood et al. examined blend polymers of PMMA/poly(lactic acid) (PLA) and PMMA/poly(bisphenol A carbonate) (PC) [26].

## 2.4 Organization of 2D materials in Van der Waals heterostructures

Van der Waals (vdW) heterostructure are made by stacking different 2D materials on top of each other without concern of the latic matching. Individual layers are attached

by van der Waals (vdW) force, which is a weak force that attracts opposite charge of nearby molecules based on dipole-induced-dipole interaction. Vertical stacking of 2D materials might change their intrinsic properties. Charge redistribution and structural changes are occurring on 2D layers induced by adjacent layers or even more distant layers, resulting in modifying their electronic structures. Hence vdW heterostructure bring about the opportunity to engineer the 2D materials properties and make variety of materials superior than traditional growth [50].

Graphene-MoS<sub>2</sub> vdW heterostructures demonstrate tremendous opportunities and they are studied by many experimental and theoretical research groups. Graphene in 2D heterostructures has been taken to account as an outermost layer due to its excellent mechanical strength and electric properties. Graphene is chemically stable material and other unstable 2D materials can be passivated when they are encapsulated by graphene. On the other hand, MoS<sub>2</sub> has an optical band gap in the spectrum from near-infrared to visible and displays a strong light-matter interaction that makes it unique to optoelectronic and photovoltaic applications [51].

Electronic band structure of single-layer graphene and MoS<sub>2</sub> will change in their heterostructure systems. The tunable band gap leads to modification of optical properties. According to DFT calculations the optical parameters such as absorption coefficient, refractive index, and the reflectance undergo a redshift; however, energy loss spectrum encounters a blueshift [52] that allow chemical and biosensing applications such as surface plasmon resonance (SPR) graphene/MoS<sub>2</sub> biosensors (the sensitivity of the SPR biosensor increases by enhancing light absorption in graphene and quenching effect on the fluorescence of MoS<sub>2</sub>) [53], nonuniformity of optical properties in a heterostructure influences device physics and performance. It happens at the nanometer scale and has not been studied before due to limitation of optical microscopy methods.

Moreover, charge transfer between the encapsulated 2D layers can be very significant and effects on the electronic properties of potential optoelectronic device. Diaz et al, transferred CV grown- graphene on a bulk single crystal of MoS<sub>2</sub>. They reported interface dipole formation, evaluated by photoemission spectroscopy. Their observation indicated p-type doping of graphene resulted in a downward shift of the Fermi-level below the Dirac point by  $\sim 0.09$  eV, and a negative space charge region formed in bulk MoS<sub>2</sub> [54]. Also, Pierucci et al, transferred CVD MoS<sub>2</sub> layer on epitaxial graphene/SiC. They reported a downshift of the Raman 2D band of the graphene, an up shift of the A<sub>1g</sub> peak of MoS<sub>2</sub>. In addition, a significant photoluminescence quenching are observed for both monolayer and bilayer MoS<sub>2</sub> as a result of charge transfer from MoS<sub>2</sub> to epitaxial graphene under illumination [55]. Moreover, Rahul Rao et al, transferred MoS<sub>2</sub> on SiO<sub>2</sub>/Si substrate then transferred graphene on top of MoS<sub>2</sub>, both transfers had been done by exfoliated method. They used a correlation analysis between the G and 2D peaks in graphene and the E<sub>2g</sub><sup>1</sup> and A<sub>1g</sub> Raman peaks in MoS<sub>2</sub>. They showed that graphene (MoS<sub>2</sub>) is p-doped (n-doped) on SiO<sub>2</sub>, i.e, there is a transfer of electrons

from MoS<sub>2</sub> to graphene [56]. Sun et al, reported that graphene has been p-doped when it comes into contact with MoS<sub>2</sub> [57].

## 2.5 Applications of two-dimensional materials and their heterostructures

Recent developments in synthesis and nanofabrication technologies in 2D materials have brought about broad spectrum of applications such as field effect/tunneling transistors, light emitting diodes, light detectors, photovoltaic and energy storage devices, and biosensors [58, 59]. In the following paragraph some applications are discussed in detail.

- Graphene/MoS<sub>2</sub> Field effect/tunneling transistor

The Junction Field Effect Transistor (JFET), is a voltage controlled three terminal semiconductor transistor. The N-channel and P-channel in JFET make it an effective functional device, suitable for applications such as electronically controlled switches, voltage-controlled resistors and amplifiers. Kim et al. [5] proposed a Graphene/MoS<sub>2</sub> JFET (Fig. 2.5 (a)). They exploited the excellent carrier mobility of graphene up to 200,000 cm<sup>2</sup>V<sup>-1</sup>s<sup>-1</sup> at room temperature [60] and direct bandgap of MoS<sub>2</sub> with a high on/off current ratio exceeding 10<sup>8</sup> [61] to make a high carrier mobility and high on/off current ratio in field-effect transistors. Applying a back-gate bias ( $V_g$ ), they tuned the Fermi level of Graphene and modulated the effective Schottky barrier height (SBH) at the interface of the graphene/MoS<sub>2</sub> from 528 meV (n-MoS<sub>2</sub>/p-graphene) to 116 meV (n-MoS<sub>2</sub>/n-graphene). As a result, the carrier mobility was enhanced by a factor of  $\sim 10$  ( $\sim 100$  cm<sup>2</sup>V<sup>-1</sup>s<sup>-1</sup>) compared to that of monolayer MoS<sub>2</sub>.

- Photovoltaics on TMD

2D Materials have opened up completely new avenues for optoelectronic applications where flexibility and transparency is important. Zhou et al., proposed a two-dimensional vertical-stacked type-II heterostructure in which graphene was exploited as top and bottom electrodes and MoS<sub>2</sub>/WS<sub>2</sub> were used as the active semiconductor layers in the middle ((Fig. 2.5 (b)). They revealed the main factor in influencing the photocurrent direction during light irradiation is stack symmetry, which governs type II band alignment (staggered gap) directionality. Comparing with monolayer TMD devices, the photovoltage enhancement was 10 times under the same optical illumination power, because of the efficient charge transfer between WS<sub>2</sub> and MoS<sub>2</sub> and extraction to graphene electrodes. To modulate the photovoltaic effect, they benefited from tuning the band alignment under applying a  $V_g$  and the tunneling-assisted

interlayer charge recombination. They envailed the layer symmetry in vertical-stacked graphene/TMD/graphene ultrathin optoelectronics can be exploited to control the electron flow directions during photoexcitation in tandem cell assembly application [6].

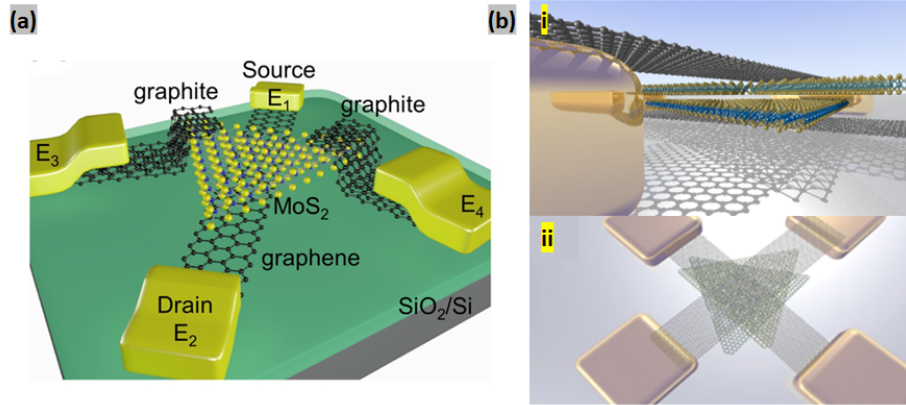


Figure 2.5. (a) Schematic of a two-terminal device with the graphene/MoS<sub>2</sub> heterostructure with graphite as the electrical contact [5]. (b) Schematic image of graphene /WS<sub>2</sub>/MoS<sub>2</sub>/graphene heterostructure photodetector. (i) the side view and (ii) the top view [6].

- 2D aptasensors

The unique structural of graphene allows ssDNA aptamers to bind to graphene surface via electrostatic interaction with DNA bases or via non-covalent  $\pi - \pi$  interaction [62–64]. Hence, biomolecule immobilization under graphene-based aptamer sensors provides an opportunity for detection of a wide range of targets. Graphene as an delivery vehicle for aptamers, can detect biomarkers into living cells or animals [62]. An ultra sensitive and label-free shear horizontal surface acoustic wave (SH-SAW)/single-layer graphene-based aptasensor detected endotoxin, a complex lipopolysaccharides found in cell walls of Gram-negative bacteria [65]. This platform showed a linear relationship with the endotoxin concentration range from 0 to 100 ng/mL, while the detection limit was 3.53 ng/mL. Furthermore, SH-SAW biosensor exceeds its endotoxin sensor counterparts through its the stability and excellent specificity. MoS<sub>2</sub> has already been studied as an aptobiosensor platform due to its conjugation with ssDNA aptamers through spontaneous adsorption via van der Waal interaction between nucleobases of ssDNA and the basal plane of 2D MoS<sub>2</sub> [66, 67]. Kong et al. reported synthesizing a novel aptamer-functionalized MoS<sub>2</sub> fluorescent sensor to detect PSA in human serum with a detection limit of 0.2 ng/mL [68]. Moreover, selectivity and sensitivity of MoS<sub>2</sub>-based aptasensors have been developed through various approaches such as the surface blocking strategy [69] and dual signal amplification strategy [70].

Non-fluorescence property of graphene due to its zero bandgap and degradability of MoS<sub>2</sub> have motivated us to combine them and form a vdW heterostructure system for detecting doxorubicin (DOX), an anthracycline cancer drug. Here, graphene covered MoS<sub>2</sub> to protect it from oxidization. Also graphene Raman shift and graphene enhanced Raman spectra (GERS) of DOX are fingerprint modes of the molecule. Moreover, photoluminescence (PL) shift of single layer MoS<sub>2</sub> made this system an multiplexed detection of DOX [71].

# Chapter 3

## Aim one: Advancement of two-dimensional materials transfer methods

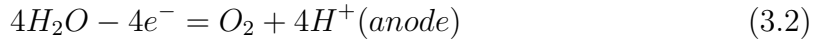
### 3.1 Task one: Dry transfer method

Transferring the CVD-grown 2D material from growth substrate onto a target substrate is desirable for many applications. During the transfer, the quality of 2D materials is threatened by contaminations (e.g., chemical doping) and mechanical damage (e.g., folds, holes and tears). Kang [47] et al. reported some of the damaged to incomplete removal of PMMA, attributed to the high adhesion potential between PMMA with graphene. Furthermore, applying impurities of the organic solvents, e.g. acetone and isopropyl alcohol, result in more surface contamination, leading to a negative effect on carrier mobility in graphene [49]. Therefore, keeping the original quality of 2D materials is synonymous to develop the efficiency of the transfer processes. Wet transfer (e.g., either etching donor substrate or electrochemical delamination) and dry transfer are two major transfer methods. As mentioned, one of the common elements in all transfer procedures is a specific polymer to support the 2D material and prevent from damage formation during the transfer. Having desirable adsorption energy ( $E_{ad.}$ ), high mechanical strength, and easy removable are important properties of this polymer. PMMA is one of the most considerable polymers. Although it has brought about successful results compared with its counterparts, completely removing from the transferred 2D material is a challenge [49]. Because it could degrade the intrinsic electrical and optical properties of the 2D materials. Thus, to overcome this problem we used a novel method that is a combination of wet and dry method. Polyethylene terephthalate polysiloxane stacks adhere to 2D material via noncovalent bond between the film and CVD Graphene/Cu. In this process, H<sub>2</sub> bubbling can

delaminate 1-inch of graphene from the Cu substrate in a few minutes or quicker, whereas in etching transfer usually hours are needed to dissolve the Cu. The catalyst is  $\sim 100\%$  reusable. Peeling off polysiloxane from graphene occurs without any solvent due to the weak adhesion energy between graphene and polysiloxane film, leading to preventing the doping of graphene [72, 73]. Here, to increase the attachment between graphene and the polysiloxane film, we applied mechanical pressure. In addition, by heating up the graphene/polysiloxane film, we increased the possibility of maintaining the quality of graphene by preventing the damage formation through polymer removal stage. This method is appropriate when large-scale transfer is needed and the 2D material is water-resistant.

### 3.1.1 Materials and methods

Graphene (purchased from Graphenea, grown by CVD method on Cu foil) was covered by polysiloxane film. Then, it was put under pressure 1 MPa for 30 min. To delaminate graphene from the Cu foil, the electrochemical method (10V and 1A) has been applied. In this process,  $H_2$  bubbles were generated at the interface between graphene and the substrate (Cu) and caused graphene to detach from Cu. The reduction reaction (equations shown below) of aqueous solution (NaOH) occurred according to the voltage applied between anode (Pt) and the cathode (Cu).



To rinse the polymer film/graphene, it was transferred into DI water and left it for 10 min, this step was repeated twice. Then, the polymer film/graphene was scooped onto a clean  $SiO_2/Si$  substrate. Finally, polysiloxane film was peeled off from graphene after baking on hot plate (at  $100^\circ C$  and for 30 min) (Fig.3.1).

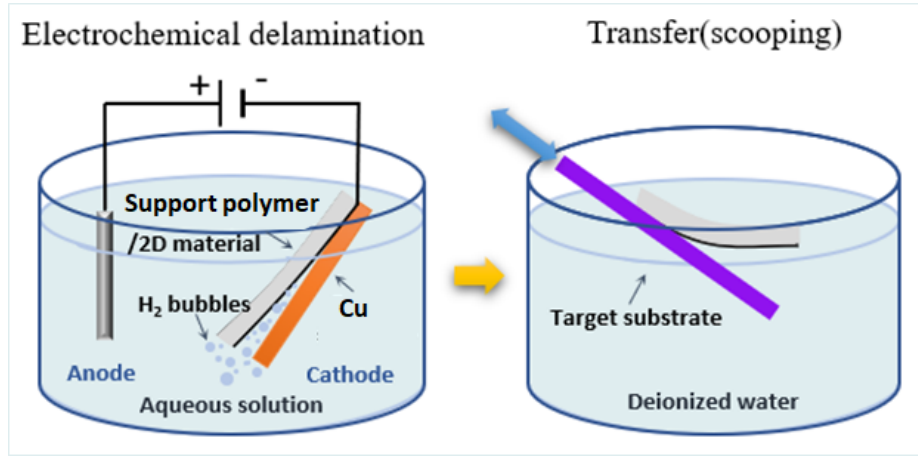


Figure 3.1. Schematic of electrochemical transfer process with  $H_2$  bubbles.

### 3.1.2 Characterization:

The topography of transferred graphene was imaged by Scanning electron microscopy (Zeiss Auriga FIB/FESEM). Raman spectroscopy (Horiba XploRa Raman Confocal system) was carried out to determine the quality of graphene.

### 3.1.3 Results and Discussion

The initial optical image of graphene transferred by polysiloxane film shows an extended-area graphene on  $SiO_2/Si$  (Fig. 3.2 (a)), which is in agreement with previously reported results [72, 73]. The SEM images illustrate that polysiloxane film led to a clean (non-doped) graphene transferred with lower mechanical damage (Fig. 3.2 (b)), which is in contrast with graphene transferred by PMMA (Fig. 3.2 (c)). Raman spectroscopy is a well-established method to scrutinize disorder (defect density), excess charge (doping) and strain in graphene. The intensity ratio of the D and D' peaks ( $I(D)/I(D')$ ) reflects the defects in graphene. These defects can be from  $sp^3$  defects, vacancy-like defects and boundaries in graphene which have a  $I(D)/I(D')$  ratio of 13, 7 and 3.5, respectively [74]. Here, the intensity of D peak ( $1326\text{ cm}^{-1}$ ) is 80.51, while D' peak (can be distinguished from the G peak split) is negligible. Thus, any types of defects in prepared area is insignificant. Both the G peak ( $1572\text{ cm}^{-1}$ ) and the 2D peak ( $2657.19\text{ cm}^{-1}$ ) shifted to a lower wave number (redshift) in response to tension strain and less p-doping which agrees with other reports[56]. The 2D peak responds stronger to strain while the G peak responds stronger to doping (Fig. 3.2 (d)). Also, the intensity ratio of the D and 2D peaks ( $I(2D)/I(D) \sim 4.7$ ) indicates graphene is monolayer [75, 76].

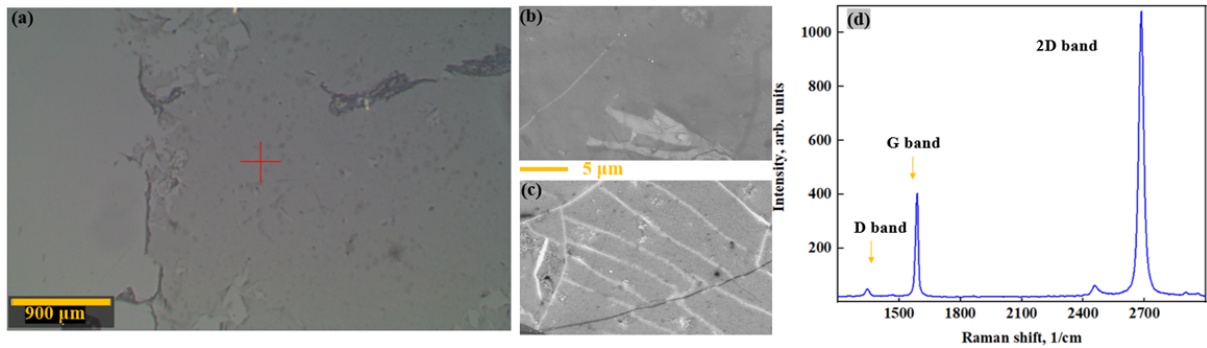


Figure 3.2. (a) Optical image and (b) SEM image of graphene transferred from Cu foil to SiO<sub>2</sub>/Si by polysiloxane film. (c) graphene transferred by PMMA. (d) Raman spectroscopy of graphene transferred from Cu foil to SiO<sub>2</sub>/Si by dry method. scale bars are 900 μm for (a) and 5 μm (b) and (c).

### 3.1.4 Conclusions

In conclusion, dry transfer method is a fast transfer technique suitable for transferring graphene in a large scale as the optical and SEM images show. Also Raman spectra indicate lower amount of polymer residues for dry transfer compared to PMMA transfer method, resulting in higher quality graphene. Described procedure can be apply for any substrate from paper to polymer, which is important for graphene-based sensor fabrication (e.g., graphene wearable sensors).

### 3.1.5 Recommendations for Future research

To attain an understanding of the topography of the sample, atomic force microscopy (AFM) can bring more morphological information in-details. Also, to study the electrical properties of the graphene transferred using conductive-AFM is recommended.

## 3.2 Task two: Novel approach for PMMA-assisted graphene transfer

Two main culprits behind the quality degradation of graphene during transferring are handling process and solvent impurities, e.g. applying acetone and isopropyl alcohol, result in more surface contamination, leading to a negative effect on carrier mobility in graphene [49]. To cope with these issues we applied a novel method, using a specific apparatus to limit the mechanical handling by operator and distill constantly the solvent during removing the polymer. Soxhlet extraction is a technique meets

both requirements due to a continuous (or, rather, automated batch) solid-liquid extraction in a Soxhlet apparatus, which is commonly used in organic, pharmaceutical, and environmental chemistry [77]. Applying Soxhlet method ensures the extraction of all the soluble material from the matrix. Also, soxhlet apparatus is very helpful in synthetic chemistry, where it is vital to separate a poorly soluble product from insoluble byproducts and requires the arduous task encountered during working with polycyclic aromatic compounds [78].

### 3.2.1 Materials and methods

- Graphene Transfer Procedure:

The CVD grown graphene on Cu foil (provided by the 2DCC PSU or purchased from Sigma-Aldrich 773697) was covered by with 4 wt. % PMMA solution (ca. 950,000 g/mol; 99.9% purity), using a spin-coater (Laurell EDC-650-8TFM) at 20,000 rpm for 5 minutes. Thereafter, the sample was thermally treated at 90°C for 5 min and then at 150°C for 2 h. The hydrogen bubbling method (as it was described in chapter 3.1) was applied to delmainate the Cu layer from the coated graphene/PMMA composite. The PMMA/graphene film was rinsed by DI water. To remove excess water trapped in between the SiO<sub>2</sub>/Si substrate and PMMA/graphene film, where further thermal treatments were carried out. Finally, the PMMA support was washed away, using either a Soxhlet apparatus or conventionally by dipping the substrate in reagent grade acetone (Sigma Aldrich, U.S.A; 99.9 %) at 25°C for 2 h.

- Soxhlet operations:

To remove the polymer support from the top layer of graphene, we used the newly developed Soxhlet extraction method. Figure 3.3 shows the apparatus consisting of a glass chamber equipped with a siphoning tube, vapor tube, and reflux condenser. The sample was inserted in the extraction chamber and a flat bottom flask was filled with acetone then it was placed in a heating mantle. The given solvent was boiled at a certain temperature ( $\geq 57^\circ\text{C}$ ), one can be sure that the evaporation, condensation, and subsequently refilling up the chamber would be proceeded at a constant temperature. This process was allowed to continue for 4h. Then the sample was extracted and dried by N<sub>2</sub> gas flow. Also, conventional washing/annealing process was carried out to compare its results with ones from soxhlet processes [79].

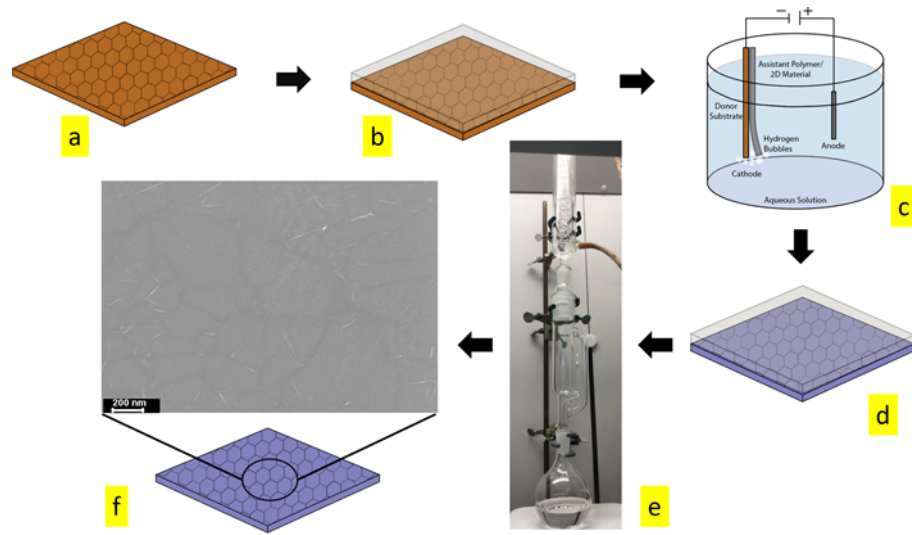


Figure 3.3. Schematic diagram of Soxhlet-assisted graphene transfer. (a) Graphene on Cu foil, (b) Graphene spin-coated with PMMA, (c) Cu foil removal by electrochemical method and subsequent transfer on SiO<sub>2</sub>/Si substrate, (d) Graphene attached on SiO<sub>2</sub>/Si-PMMA composite, (e) Soxhlet apparatus setup for PMMA removal, (f) Ultra-clean graphene on target substrate.

- Soxhlet assisted transfer onto target substrate:

In conventional removal polymer process, impurities inevitably present in the solvent, the sample is exposed to the dust from the atmosphere and the quality of transferred graphene is degraded because of the residues left from the incomplete PMMA removal process (see SEM images in Fig. 3.7 (a,b)). Against the conventional method, Soxhlet procedure dissolves polymer with ultra-pure acetone. The enclosed chamber leads to minimise the exposure of solvent to dust. Also, the negligible sample handling reduces the possibility of sample contaminate. In Soxhlet apparatus, the continuous distillation and extraction processes purify the solvent and minimize the solvent consumption without need for a separate a distillation setup. The sample is exposed to a repeated washing process with freshly distilled solvent, which allows a complete removal of the polymer. Other advantages of applying Soxhlet apparatus are green closed-loop recycling of the solvent and avoiding the need of operating the process in a clean room.

### 3.2.2 Characterization

Raman mapping of samples was performed using a Horiba XploRa Raman Confocal system with an objective lens of 100X. A total of 2000 data points were collected by laser excitation at 532 nm, using the 1200 lines mm<sup>-1</sup> diffraction grating. The

samples were imaged with a scanning electron microscope (Zeiss Auriga FIB/FESEM), using an accelerating voltage of 5 kV and a working distance of 5 mm. AFM topographical images were obtained with an Oxford Research AFM (MFP-3D infinity) instrument using the tapping mode under ambient conditions, and Si tips coated with Al (TAP300AL-G probe, Budget Sensors) was used.

### 3.2.3 Results and Discussion

Optical microscopy image, as a simple and quick characterization, confirms the quality of transferred graphene (Fig. 3.4). Both Soxhlet assisted and conventional transfer techniques showed graphene considerably covered the substrate. Some cracks were observed in both images due to defects occurred during PMMA removal, but they are more negligible in the Soxhlet assisted method [80,81]. Also, a distinct pattern was observed on both samples, which is attributed to the rough surface of Cu. SEM images give further information about the quality of graphene transferred in nanometer scale (Fig. 3.7(a,b) and insets).

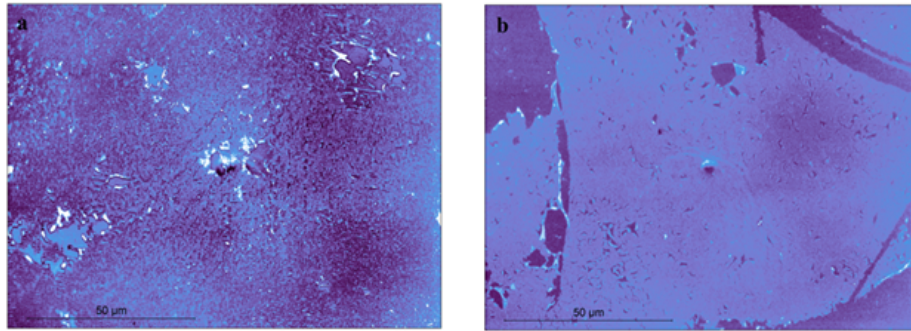


Figure 3.4. Optical microscopy images of graphene films from (a) conventional transfer and (b) Soxhlet assisted technique.

Fig. 3.7 (a) shows the dark dots in magnified areas, representing the impurities introduced by acetone in conventional method, but not in Fig. 3.7 (b) (Soxhlet). Also, the charged features indicate the presence of PMMA residues, specifically around the graphene edges, which are more significant in conventional protocol, proving that conventional method is not as effective as Soxhlet method. Also, it was observed that the grain boundary non-uniformities resulting from CVD growth graphene on Cu are more pronounced for graphene obtained by Soxhlet than conventional transfer method (where residues masked the distribution of these non-uniformities). Moreover, mechanical damages were minimized by the Soxhlet method, which is in contrast with the conventional immersion washing approach where significant folding and cracking was observed in the final graphene film.

Using atomic force microscopy (AFM), we precisely studied the surface topology of the graphene films transferred with both techniques (Fig. 3.7 (c,d)). It was observed the less polymer contamination on the graphene areas of about  $4 \times 4 \mu\text{m}^2$  by the Soxhlet method and the AFM line profile showed the lower surface roughness RMS value. We hypothesize that continuous contact of the PMMA-graphene/SiO<sub>2</sub> substrate with freshly distilled acetone in Soxhlet method would disrupt the strong interactions between PMMA and graphene and help effectively remove PMMA from graphene film [49, 82, 83].

Raman spectra were collected using micro-Raman spectrometer to probe structural and electronic properties of graphene and characterize the effect of PMMA removal of graphene samples transferred either by Soxhlet or conventional methods (Fig. 3.8 (a-f) and Fig. 3.6).

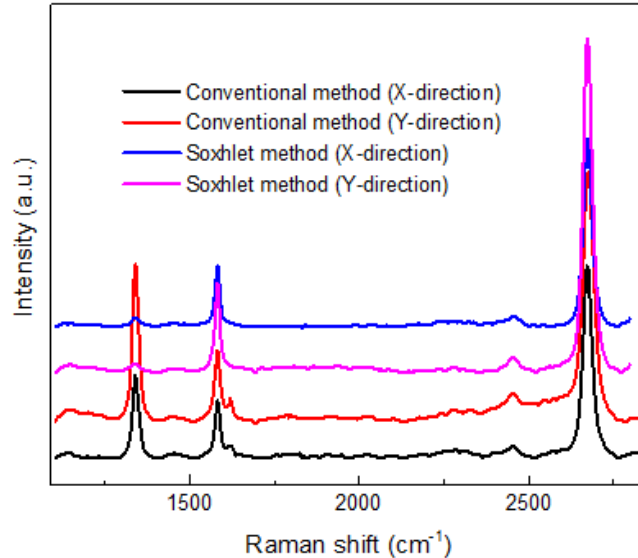


Figure 3.5. Micro-Raman spectroscopy scans in X- and Y-directions on the graphene transferred by conventional and Soxhlet methods.

The scanned area in two spatial directions (X and Y) indicate the presence of significant number of defects/imperfections in graphene transferred by the conventional method. However, the spectra of samples transferred using our Soxhlet method show the D-band peak was negligible (Fig. 3.5). Defect formation in graphene occurs either during the CVD growth [84] or transfer [49] processes. As both graphene transferred samples are identically the same before PMMA removal process, our results proves the significant efficiency of Soxhlet method. The strain and doping levels of graphene can be assessed by Raman spectroscopy data [85, 86].

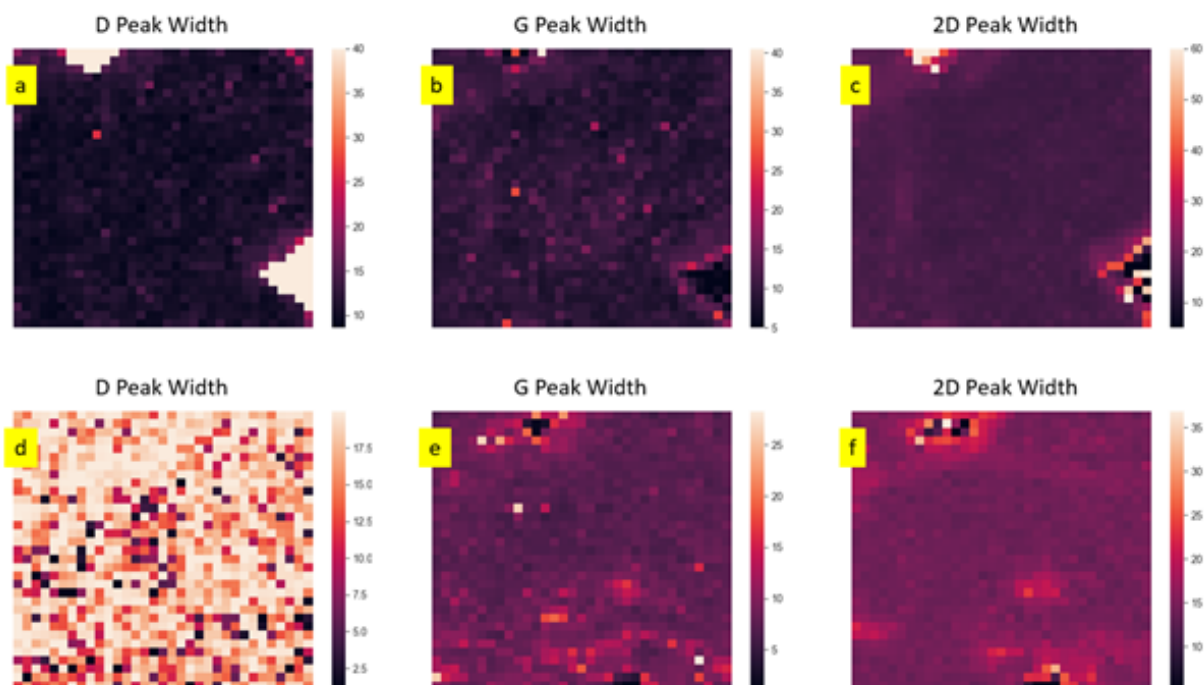
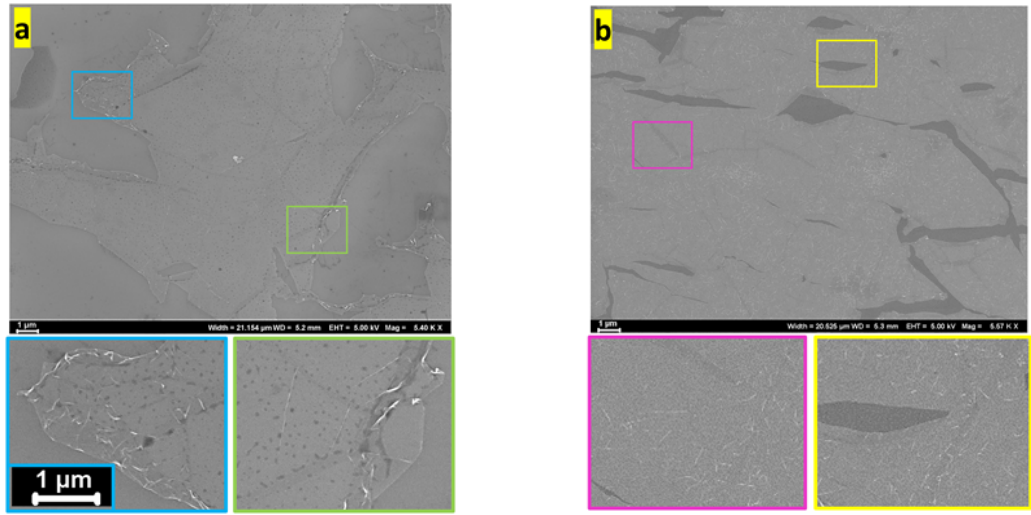


Figure 3.6. Width maps of fitted peaks obtained from Raman characterization ( $10 \times 10 \mu\text{m}^2$ ) of graphene transferred with (a,b,c) conventional PMMA method; (d,e,f) Soxhlet assisted PMMA method.

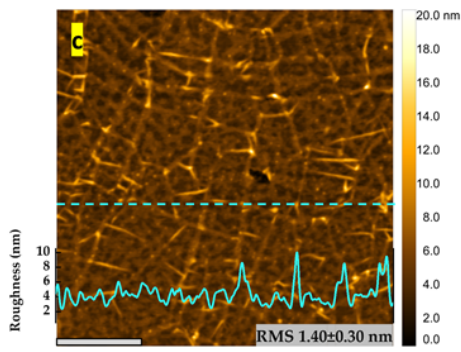
Raman maps ( $10 \times 10 \mu\text{m}^2$ ) shows strong and homogeneous G and 2D bands of graphene for both methods, indicating the consistent results (Fig. 3.8). The previous reports [87–89] about the 2D/G intensity ratio of single ( $>1.6$ ), double ( $\sim 0.8$ ), triple ( $\sim 0.30$ ) and multi layer ( $\sim 0.07$ ) graphene sheets indicate graphen used in this research was monolayer (Fig. 3.9 (b,c)). Also, the full width at half maximum (FWHM) of 2D peak was  $32.4 \text{ cm}^{-1}$  over the whole area of characterization (Fig. 3.6). The correlation of Raman plot between G-2D modes reveals very similar amount of strain and doping for both techniques (Fig. 3.8 (a)). On the other hand, the average D/G intensity ratio of graphene film obtained by the Soxhlet and conventional are  $0.17 \pm 0.07$  and  $0.90 \pm 0.30$ , respectively (Fig. 3.9 (d,e)), which indicates the presence of defects is more pronounced for conventional graphene transfer method.

The proposed method revealed great reproducibility with negligible variation during the structural characterisation. In our lab, the Soxhlet-assisted approach has become the method of choice since it allows many transfers to be carried out concurrently, saving time and reagents while maintaining graphene’s purity and unique properties.

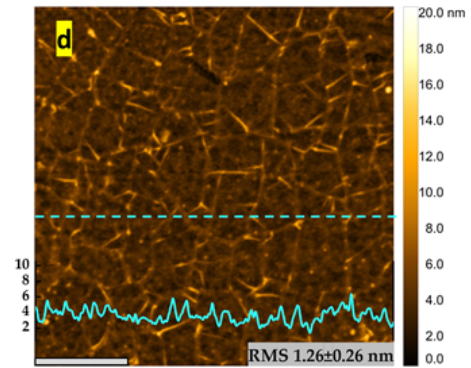


(a)

(b)



(c)



(d)

Figure 3.7. Characterization of transferred graphene films on  $\text{SiO}_2/\text{Si}$  substrates. SEM images of (a) Conventional transfer method. (b) Soxhlet transfer method. Color framed insets represent zoomed areas. AFM profile of (c) Conventional transfer method. (d) Soxhlet transfer method, scale bare is  $1\mu\text{m}$ . Inset: The AFM line profile graph for both transfer techniques.

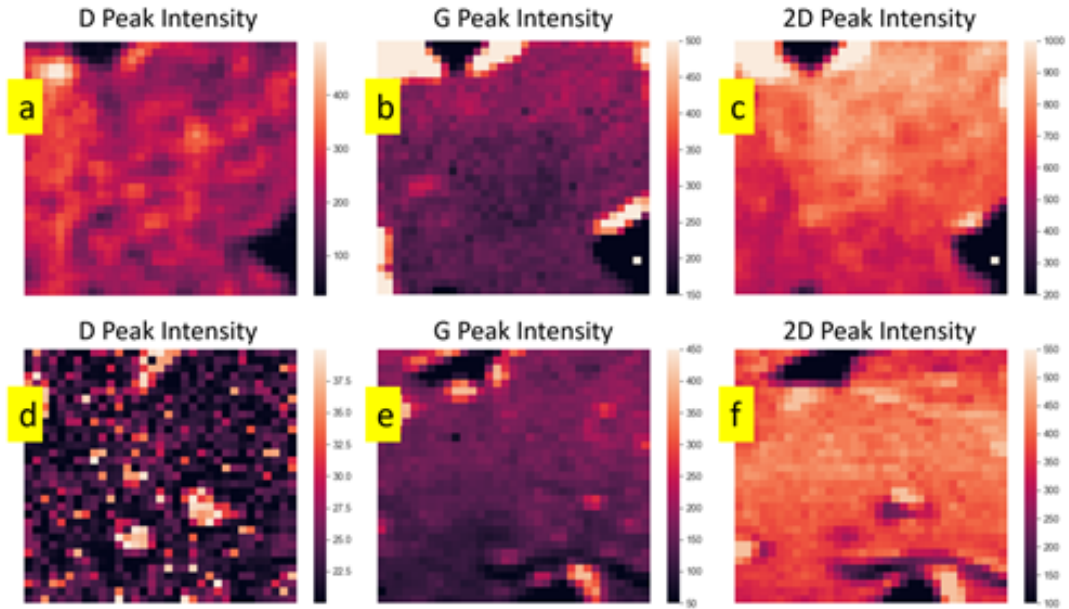


Figure 3.8. Corresponding maps of plotted results of Raman characterization ( $10 \times 10 \mu\text{m}^2$ ) of graphene transferred with (a, b, c) conventional PMMA method; (d, e, f) Soxhlet assisted PMMA method.

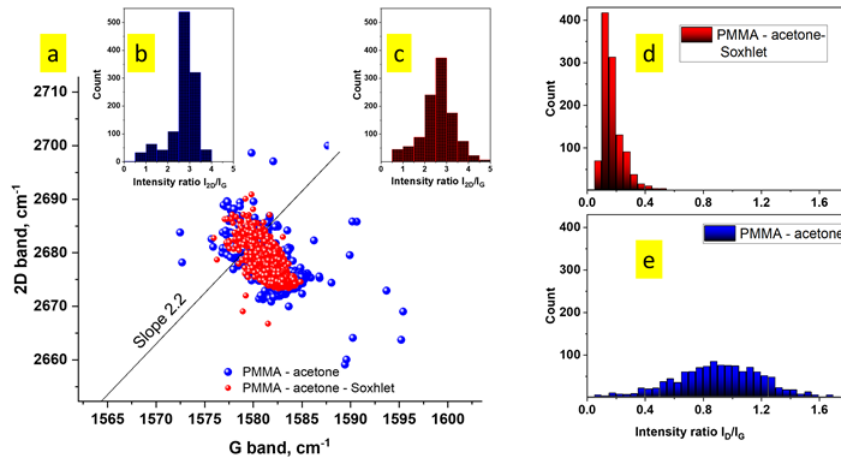


Figure 3.9. (a) Correlation map of the Raman G and 2D peak positions of graphene transferred with conventional PMMA technique (blue) and Soxhlet assisted PMMA technique (red); (b), (c) Histogram of 2D/G ratio with the same color code indicating the sample quality in general. (d), (e) Histogram of D/G ratio with the same color code as a signature of defect amount.

### 3.2.4 Conclusions

In conclusions, the novel Soxhlet-assisted approach allowed us to transfer a graphene film onto a target substrate with minimum surface contamination and damage compared to other methods. Comparing to the sample obtained by the conventional approach, the graphene film transferred by our innovative method has fewer defects, according to a much lower average D/G intensity ratio. Despite of the similar amount of strain and doping in both procedures, more significant polymer removal, minimal structural damage, experimental simplicity and reduced solvent residue use make the Soxhlet method exceed through the conventional procedure. Moreover, this procedure might be suitable for transferring other delicate two-dimensional materials (manuscript has been published by ACS omega journal).

### 3.2.5 Recommendations for Future research

The presented results suggest further study to show the effect of Soxhlet method on other 2D materials ( $\text{MoS}_2$ ,  $\text{WS}_2$ ,  $\text{WSe}_2$ , and etc.) transferred from growth to target substrate. The residues should be quantified by contact-AFM before and after polymer removal steps. Also, to prove that the contamination was resolved from the graphene transferred, conductive-AFM should be employed.

## 3.3 Task three: Optimization of interaction on graphene-polymer interface

The functional groups of PMMA make van der Waals interactions with  $\pi$  network in graphene or covalent bonds with defect sites of graphene, resulting in a strong connection between polymer and the 2D material [33, 90]. Although this attachment supports graphene during transferring by preventing the formation of wrinkle, hole and tear, completely removing the polymer from graphene is an open question. Multiple research groups are working on this issue by applying different removal treatment techniques [91, 92] or by using other polymers as PMMA substitution [26, 49, 93]. However, there is a lack of comprehensive study on the energy of adhesion between graphene and its support polymer. According to the modified Hertz theory [94], the adhesion force between elastic solids is proportional to the surface energy. The lower the surface energy of graphene and surface tension of the polymer, the weaker the adhesion force between the graphene and polymer film, and thus the polymer removes more easily by mechanical forces or dissolution.

Surface tension is proportional to the strength of the cohesive force, which varies with the type of liquid in general. Surface tension  $\gamma$  is defined to be the force  $F$  per

unit length  $L$  exerted by a stretched liquid membrane (Fig. 3.10 (b)):

$$\gamma = \frac{F}{2L} \quad (3.3)$$

in which the units are N/m or mN/m (= dyn/cm in c.g.s units). The work required to increase the surface area by an amount of  $dx$  is called surface energy ( $dW$ ), which equals the increase in Gibbs free energy ( $G$ ) (Fig. 3.10 (a))

$$dW = 2\gamma Ldx = dG \quad (3.4)$$

Gibbs free energy for two systems in contact:

$$dG = -SdT + V_1dP_1 + V_2dP_2 + \sum \mu_i dN_i + \gamma dA \quad (3.5)$$

where  $S$  is entropy,  $T$  is temperature,  $\mu_i$  is chemical potential of species  $i$ ,  $N_i$  is the number of elements of chemical species  $i$ ,  $V_1$  and  $P_1$  are volume and pressure of system 1, and  $V_2$  and  $P_2$  are volume and pressure of system 2 (Fig. 3.10 (b)).

If  $P_1 = P_2 = P$  and  $V_1 = V_2 = V$ ;

$$dG = -SdT + VdP + \sum \mu dN_i + \gamma dA \quad (3.6)$$

$$\left. \frac{dG}{dA} \right|_{T,P,N_i} = \gamma \quad (3.7)$$

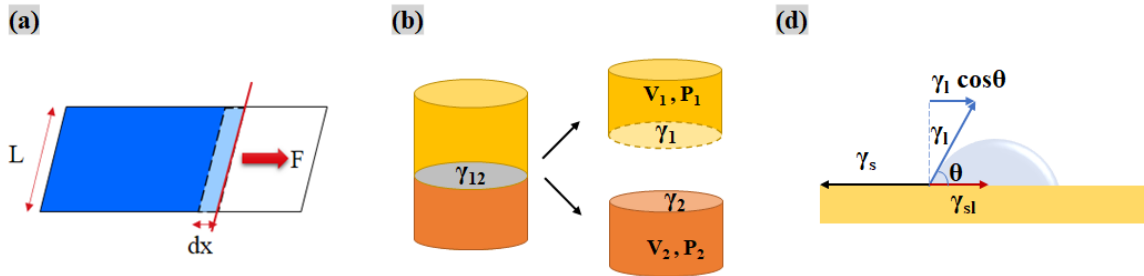


Figure 3.10. a) Surface tension, b) Adhesion energy, c) Contact angle

The hydrophobicity/hydrophilicity of molecules plays a key role in determining the surface energy and the energy adhesion between the interface of materials with which they are coming into contact. In order to understand the mechanism of hydrophobicity/hydrophilicity or wetting characteristic of a surface, a simple model is defined by Young's equation or the Young–Dupré equation [95]. This model is based

on thermodynamic equilibrium between the solid, liquid and gas phases, which defines a relationship between contact angle of a liquid droplet in contact with a solid surface with three tensors: the surface tension, the interfacial tension between a liquid and a solid surface, and the surface free energy of the solid. Young's equation is defined as:

$$\gamma_S - \gamma_{SL} = \gamma_L \cos \theta \quad (3.8)$$

where  $\gamma_L$  is the surface tension of the liquid,  $\gamma_S$  is the surface free energy of the solid,  $\gamma_{SL}$  is the interfacial tension between the liquid and the solid, and  $\cos \theta$  is the contact angle between the liquid-vapor interface and the solid surface (Fig. 3.10 (c)).

The relation between interfacial tension of solid surface and the solid-liquid interface can determine whether contact angle ( $\theta$ ) is either less or greater than  $90^\circ$ , which is an interpretation of the wettability of the surface.

$$\begin{cases} 0 < \theta < 90^\circ & \text{for } \gamma_S > \gamma_{SL} \\ \theta > 90^\circ & \text{for } \gamma_S < \gamma_{SL} \end{cases}$$

If  $\gamma_S > \gamma_{SL}$ , the right side of equation (3.9) is positive, which means  $\cos \theta$  has to be positive, resulting in  $0 < \theta < 90^\circ$ . It means the liquid partially wets the solid and the surface is said to be hydrophilic. The hydrophobicity rises as the contact angle of the droplets with the surface increases. If  $\gamma_S < \gamma_{SL}$ , the contact angle will be greater than  $90^\circ$  since  $\cos \theta$  has to be negative. Hence, hydrophobic surfaces have contact angles larger than  $90^\circ$ .

As  $\gamma_{SL}$  is hard to be obtained, it is helpful to express it through  $\gamma_L$  and  $\gamma_S$  by considering a relation proposed by Girifalco, Good, and Fowkes [96, 97]. Based on their theory, molecules of solids and liquids are held together by van der Waals forces. They separated two materials at the interface. Two new surfaces are formed while the interfacial area disappears. Rearrangement leads to

$$W_{adh} = \gamma_1 + \gamma_2 - \gamma_{12} \quad (3.9)$$

Where,  $W_{adh}$  is work of adhesion per cross-sectional area.  $\gamma_1$ ,  $\gamma_2$  and  $\gamma_{12}$  are the surface free energy of phase 1, the surface free energy of phase 2 and the interfacial tension between phase 1 and 2, respectively ((Fig. 3.10 (b))).

Also, the work required to separate two solids to an infinite distance apart, is given by:

$$W_{adh} = \frac{A_{12}}{12\pi D_0^2} \quad (3.10)$$

Here,  $A_{12}$  is the Hamaker constant for the van der Waals interaction between two materials in vacuum (air) and  $D_0$  is a typical interatomic spacing. The "mixed" Hamaker constant can be expressed by  $A_{12} \approx \sqrt{A_{11} \cdot A_{22}}$  [98, 99]

From here the surface tensions of a single material can be defined by:

$$\gamma_1 = \frac{A_{11}}{24\pi D_0^2} \text{ and } \gamma_2 = \frac{A_{22}}{24\pi D_0^2}$$

Finally,  $\gamma_{12}$  will be expressed by:

$$\gamma_{12} = \gamma_1 + \gamma_2 - 2\sqrt{\gamma_1 \cdot \gamma_2} \quad (3.11)$$

The model of Girifalco, Good, and Fowkes has been extended to other interactions. For example, if we assume that the surface energies are the sum of van der Waals (dispersive) and polar interactions, one often uses the equation

$$\gamma_{SL} = \gamma_L + \gamma_S - 2\sqrt{\gamma_S^p \cdot \gamma_L^p} - 2\sqrt{\gamma_S^d \cdot \gamma_L^d} \quad (3.12)$$

Where,  $\gamma_S = \gamma_S^p + \gamma_S^d$  and  $\gamma_L = \gamma_L^p + \gamma_L^d$ . The superscripts “d” and “p” indicate dispersive and polar interactions [100].

To evaluate the interfacial tension between polymer and graphene, one of the common methods is measuring the contact angle of each polymer coating film. In fact, the contact angle increases with decreasing the polymer film hydrophilicity. Therefore, the lower hydrophilicity of the polymer, the less adhesion energy between graphene and polymer.

Surface energy of graphene by using the Girifalco-Good-Fowke’s Young equation [101]:

$$\gamma_S = \frac{[\gamma_L(1 + \cos\theta)]^2}{4\gamma_L^d} \quad (3.13)$$

The surface tension of polymer can be estimated by the molar parachor, which was introduced by Sugden (1924), who defined a list of atom-groups’ contributions [102];

$$\gamma_P = \left(\frac{P_s}{V}\right)^4 = \left(\frac{P_s \times \rho}{M}\right)^4 \quad (3.14)$$

where  $\gamma_P$  is surface tension of polymer,  $P_s$  is molecular parachor, V is molar volume, M is molecular weight and  $\rho$  is density.

In this work, we blended PMMA with polyfuranone chain products (PCPs) to improve The efficiency of graphene transfer. PCPs has a lactone ring and makes non-covalent  $\pi$ - $\pi$  interaction with graphene. The interaction is expected to be weak compared to one with pure PMMA. Hence, the long polymer chains might remove easily during solvent treatment, resulting in obtaining a clean graphene. Alternatively, blending the two polymers (tagged as polyblend; PB) reduces adhesion energy (Ea) of PMMA.

### 3.3.1 Method and Materials

- Synthesis of polyfuranone chain products (PCPs):

PCPs was synthesized via di/trimerization reaction of angelica lactone (AL) in the presence of  $K_2CO_3$  catalyst and the mixture was heated to  $80^\circ C$  under constant stirring (300 rpm) for 5 min [103]. A highly viscous liquid was obtained after cooling of the reactor and the catalyst was removed via multiple DI water treatment.

- Transferring graphene

The CVD grown graphene on Cu foil (purchased from Graphenea) was covered by a thin film of polymers through a spin coating process (Laurell EDC-650-8TF). To dry the polymer films on graphene, samples were left at the lab overnight. Graphene was elaminated form the Cu foil by electrochemical method, after rinsing in DI water the graphene/PMMA was transferred to  $SiO_2/Si$  substrate. Sample was put on hot plate to be dried ( $95^\circ C/ 10 \text{ min}$ ) and then to be baked ( $135^\circ C/ 30 \text{ min}$ ). The polymer removal from the top layer of graphene was carried out by the acetone immersion (Sigma Aldrich, U.S.A; 99.9 %) subsequently isopropyl alcohol (IPA) and DI water rinsing was done to remove more impurities (Fig. 3.11).

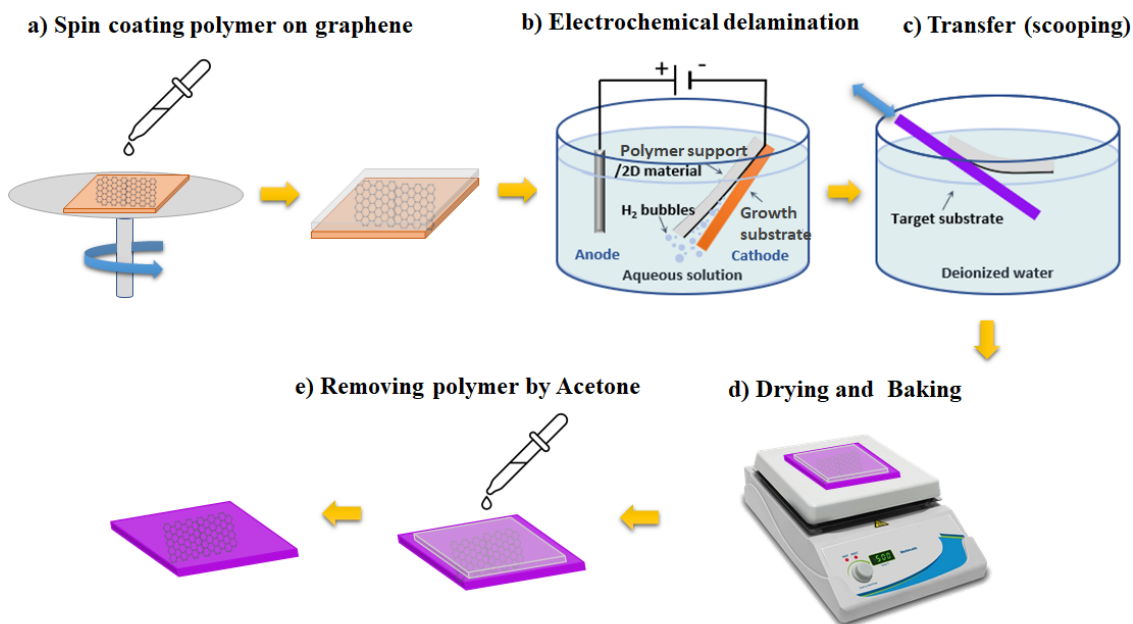


Figure 3.11. Graphene transfer schematic

- DFT simulations:

Density functional theory (DFT) simulations are employed using Gaussian 16 software [104] is used to examine the thermodynamics and kinetics of the polymers adhesion to the surface of graphene (courtesy of Jared Averitt). The graphene sheet is modeled after a C54 structure that contains 54 carbon atoms (Fig. 3.12 (e)). This graphene model structure is a compromise between the computational costs of calculations and effectively neglecting edge effects. The hybrid functional, M062X, was paired with the 6-31 + g(d) basis set to compute the optimized geometries and orbitals. Additional modules include implicit solvent (acetone) using the conductor-like polarizable continuum (CPCM) model along with Grimme's dispersion correction (GD3) for dispersion force correction. The dispersion correction is necessary when weak forces such as van der Waals are dominant between molecular fragments. The optimized geometries are given for each graphene/PB, graphene/PCPs, graphene/PMMA and PBPs bound systems from DFT simulations (Fig 3.17).

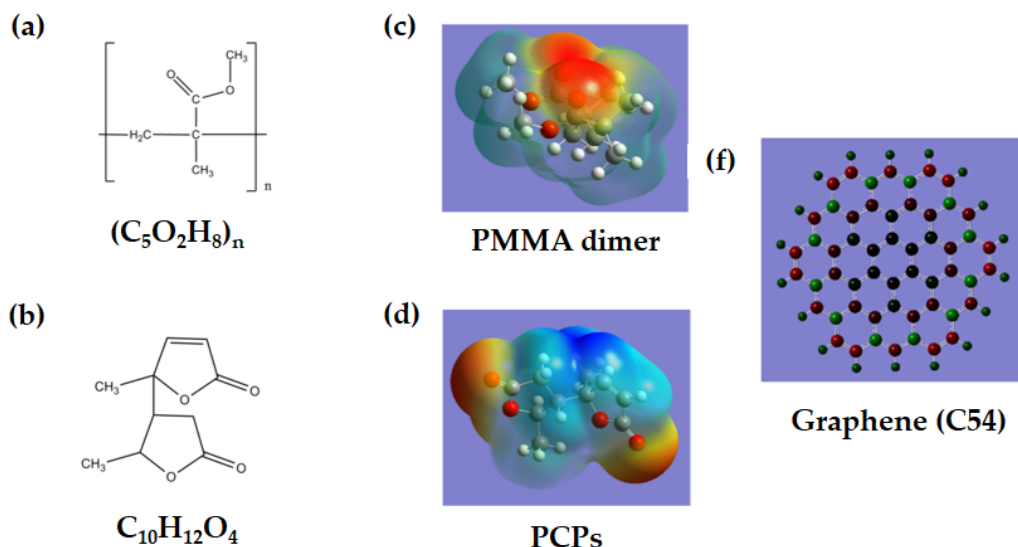


Figure 3.12. Chemical structures, formula and isosurface of electron density overlaid with color map of electric potential from DFT computations. Chemical structures and formula of a) PMMA and b) PCPs. Isosurfaces of c) PMMA and d) PCPs. The shape and size of the surface show electron density cloud of existence up to 95% probability. Red regions of isosurfaces represent most electro-negative regions while blue regions represent relatively electro depleted regions and green regions having a neutral charge. Carbon atoms in grey, hydrogen atoms in white and oxygen atoms in red. Graphene structure e) with 54  $sp^2$  hybridized carbon atoms.

### 3.3.2 Characterization

- Experimental part:

The samples were imaged with a scanning electron microscope (Zeiss Auriga FIB/FESEM), using an accelerating voltage of 5 kV, and a working distance of 5 mm. Raman spectra were taken using Horiba Raman Confocal Spectrometer at 100x magnification. AFM topographical images were obtained with an Oxford Research AFM (MFP-3D infinity) instrument, using the tapping mode under ambient conditions, and Si tips coated with Al (TAP300AL-G probe, Budget Sensors) were used. Contact potential difference (CPD) at the graphene was measured by Kelvin probe force microscopy (KPFM) using amplitude modulation (AM-KPFM). Here, graphene was probed by a conductive Pt/Ir-coated tip (EFM, Nanoword) while silver paint was used for grounding. The contact angle of water drops on the surface of graphene/Cu samples were measured using a Kruss Tensiometer. A water droplet of 3  $\mu\text{L}$  was formed using a syringe and deposited onto the sample surface in an ambient condition. The image was taken by a charge coupled device (CCD) camera. The contact angle was then measured by Drop image advanced software from the contact point of the baseline and the fitted curve to estimate the contact angle of the water droplet on the solid surface based on 5 repeats.

### 3.3.3 Results and discussions:

In this work, we used PMMA with lower molecular weight compared to conventional PMMA since it has shorter chains, leading to easier removal of backbone bonds of polymer [93]. Despite these results, the graphene transferred lacks desirable quality due to the PMMA residue, tears, and holes. To overcome this issue, Wood et al. examined bilayers of PMMA/poly(lactic acid) (PLA) and PMMA/poly(bisphenol A carbonate) (PC) [26]. We transferred graphene using PMMA/PCPs bend or PB procedure. According to SEM images, PCPs is not a suitable for transferring graphene along but the blend of PCPs and PMMA improved graphene in macro scale compared with PMMA. We blended PCPs and PMMA with ratio 1:2, 1:3, 1:4, 1:6. According to SEM images (Fig. 3.13), the optimal ratio was 1:4 since it has less polymer residue, lower tears and holes, and large-area graphene.

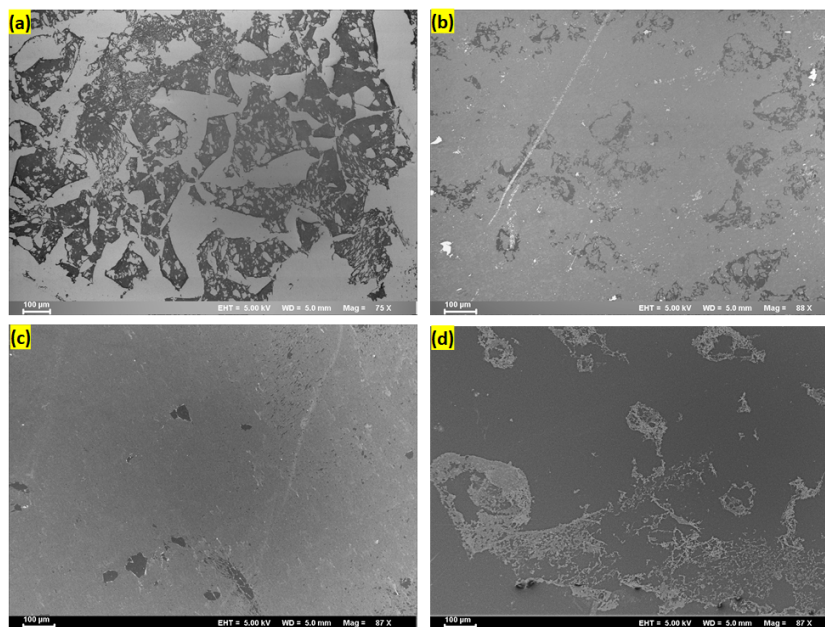


Figure 3.13. SEM images of graphene transferred by (a)PMMA, (b)PCPs/PMMA 1:6, (c)PCPs/PMMA 1:4, (d)PCPs/PMMA 1:2

Observation of the surface morphology by AFM can confirm the SEM images of two samples; PMMA and PCPs/PMMA 1:4 (Fig. 3.14 (a,b)) being fabricated with the same transfer process ( $25 \text{ m}^2$  areas). To statistical analysis, we did image processing by Gwyddion 2.59 freeware (<http://gwyddion.net>). The root mean square (RMS) was calculated through row/column statistical function (Fig. 3.14 (c,d) and table 3.1). Decreasing the surface roughness according to RMS analysis from 2.96 nm to 0.96 nm indicates the increasing quality of graphene transferred by mixed polymers compared with pure polymer. Height profile along the dashed lines shows decreasing the range of fluctuations in height due to wrinkles and polymer residues from 0-8 to 0-4 nm. According to the height profile, both the residues and wrinkles, are more presented in sample S1 compared to the sample S3. It is worth to note that the wrinkles can be formed during graphene synthesis as well as during transfer process [82]. To show accurately the role of polymers in inducing the wrinkles during transfer, we need to do more examination on graphene on Cu.

Raman spectra were fitted using least squares minimization of Lorentzian peaks. The PB transferred graphene has an area of few layer graphene, which has been removed as outliers (green hexagon shape) from scatterplots (Fig. 3.14 (a,c)). Figure 3.14 shows the results of this fitting. In Fig. 3.14 (c,d), we see that there are areas of comparatively high strain and low strain in both samples but the PB sample has more uniformity than the PMMA-only sample. Likewise, in Fig. 3.14 (a,b), the spectra

reveal uniform doping in the mixed polymer sample, but larger variance in the doping of the PMMA-only sample. We can clearly see that the PMMA only sample has a wider 2D peak (Fig. 3.14 (e)), and a significant shift both the G and 2D peak compared to the mixed polymer sample. In Fig. 3.14 (f), we plot the G peak vs the 2D peak of both samples. Using vector decomposition we can obtain the amount of strain and doping that causes the peak shift [105]. Points on the plot which lie at the intersection of the two lines would have zero strain and zero doping. As strain is introduced to the sample, the peak locations will shift along the red curve, with both G and 2D peaks shifting to a lower wave number for tensile strain and shifting to a higher wave number for compressive strain. Higher p-doping values will shift the peak along the magenta curve away from the intersection. We expect our sample to be p-doped and so n-doping is ignored. The Raman spectra shows that the PB has less variation in both strain and doping and is closer to neutrally doped than the PMMA-only sample. We conclude that the Raman spectra of the mixed polymer transfer method shows more uniform, high-quality graphene than the PMMA-only transfer method.

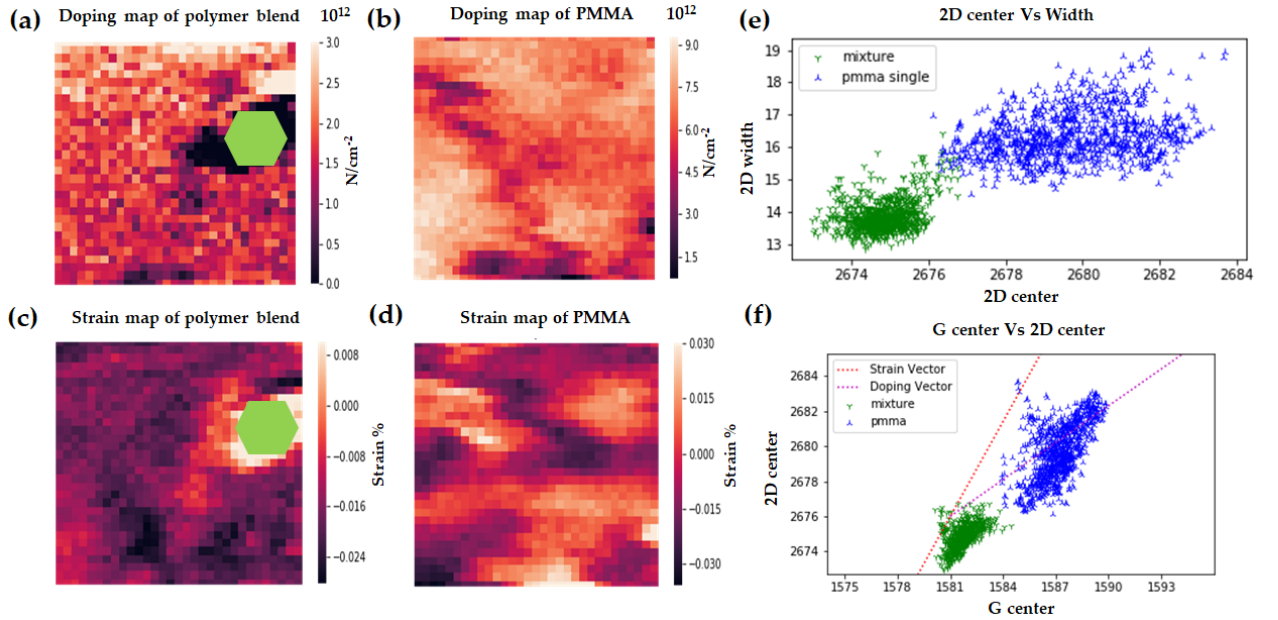


Figure 3.14. Raman map for doping of (a) graphene transferred by PMMA and (b) graphene transferred by 1:4. Raman map for strain of (c) graphene transferred by PMMA and (d) graphene transferred by 1:4. (e) 2D center vs Width plot. (f) correlation plot of G peak vs 2D peak.

To investigate electrical properties of the graphene, Kelvin probe measurements

are performed under ambient conditions. First, the topography of each scan line is recorded using tapping mode for distance control. In a second pass, at a constant distance from the sample (lift height  $< 50$  nm), we perform Kelvin probe force microscopy (KPFM) using amplitude modulation (AM-KPFM). We measured the contact potential difference (CPD) at the graphene. Here, a part of the graphene was grounded by silver paste and CPD was measured. The surface potential map shows some distinct levels of contrast associated with graphene folds, wrinkles, holes, nucleation seeds of graphene synthesis, and polymer residues. CPD profile lines along the dashed lines (Fig. 3.15 (e,f)) show a variation of the local work function of graphene transfer by PMMA and mix polymer support. This reflects the effect of decreasing p-dopant polymer residues and wrinkles due to the different work functions of the materials.

Fig 3.16 illustrates the contact angle (CA) of a water droplet in contact with the surface of graphene, PPMA film, PCPs/PMMA 1:6 film and PCPs/PMMA 1:4 film. The average CA of graphene ( $94.8^\circ$ ) indicates that the graphene used in this research is hydrophobic. This result is in agreement with the previous reports; graphene is hydrophobic 2D material with contact angle of  $95^\circ$  because of nonpolar  $sp^2$  structure. Fresh graphene on Cu (the growth substrate) intrinsically has a mildly polar (hydrophilic) surface because of  $\pi$  hydrogen bonding, surface defects, and partial wetting transparency [106]. The adhesion energy of graphene in contact with a polymer film is directly proportional to the polarity of polymer, i.e. it rises with increasing the polarity of polymer. To achieve a desirable adhesion bonding between graphene and its support polymer, one should manipulate the hydrophobicity of the polymer through increasing the polar component of surface energy [107]. By adding different ratio of PCPs to PMMA, the hydrophobicity of the blend polymer would undergo changes. According to table 3.2, the differentiation of the contact angle of a water droplet on PMMA, PCPs/PMMA 1:6, PCPs/PMMA 1:4 ( $78.4 \pm 1.27$ ,  $86.4667 \pm 0.49$  and  $95.575 \pm 0.55$ , respectively) indicates that the polymers are different in terms of their surface polarity. The CA results support the SEM and AFM images, showing the optimum graphene transferred achieved by using the PCPs/PMMA 1:4.

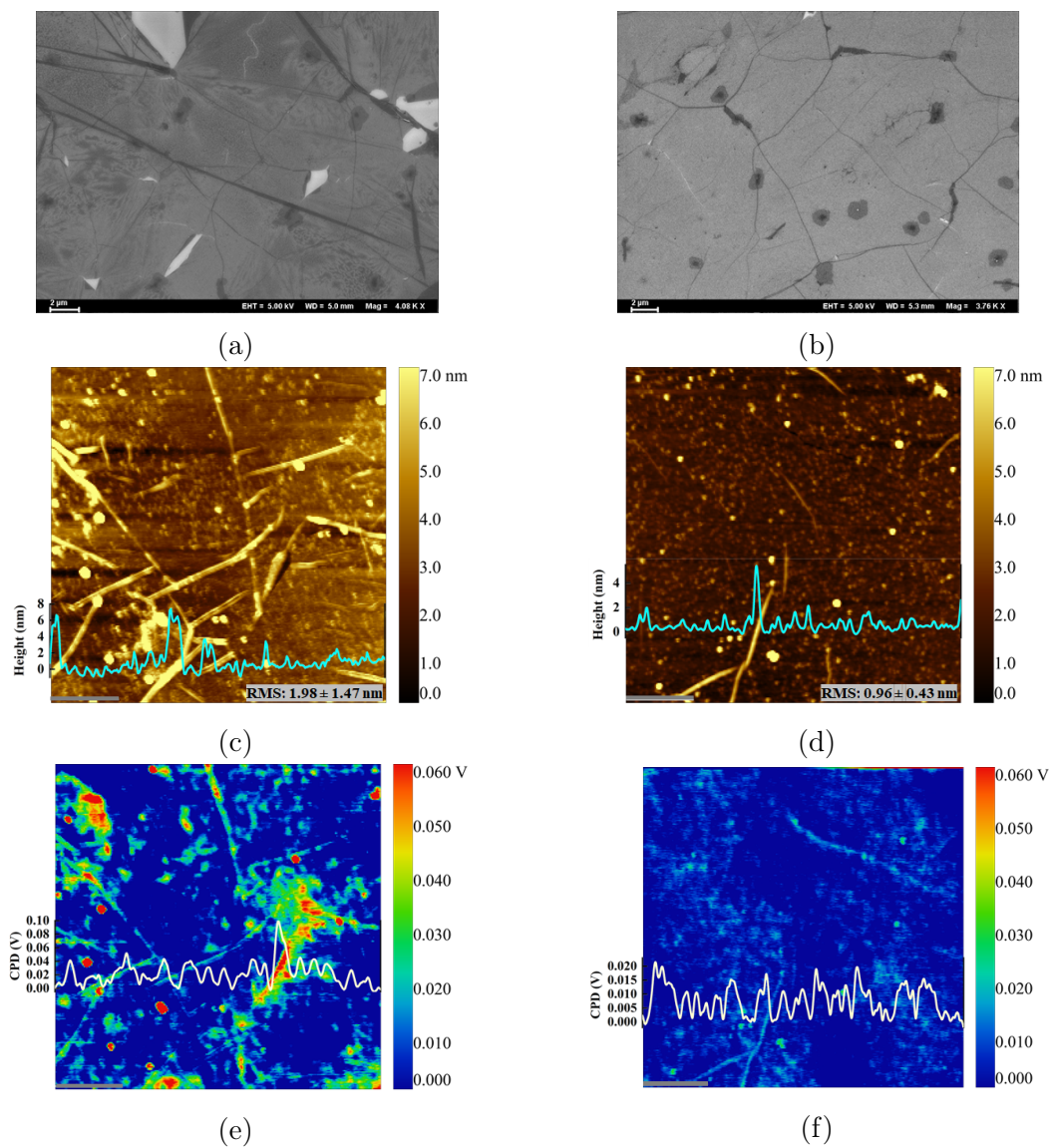


Figure 3.15. Decreasing of polymer residues in graphene transferred because of using mixed polymer of PCPs/PMMA instead of PMMA. SEM (a and b), AFM (c and d) and line profile of samples: S1 and S2, respectively. scale bars are 2  $\mu$ m and 1  $\mu$ m in SEM and AFM images, respectively.

Table 3.1. Summary of topography properties of the samples

| Number | Sample             | RMS(nm)          |
|--------|--------------------|------------------|
| S1     | PMMA               | $2.69 \pm 0.80$  |
| S2     | PCPs/PMMA 1:6      | NA               |
| S3     | PCPs/PMMA 1:4      | $0.96 \pm 0.61$  |
| S4     | PCPs/PMMA 1:2      | NA               |
| S5     | PCPs/PMMA 1:1      | NA               |
| S6     | Si after transfer  | (0.6 - 1.34)     |
| S7     | Si before transfer | $0.13 \pm 0.02A$ |

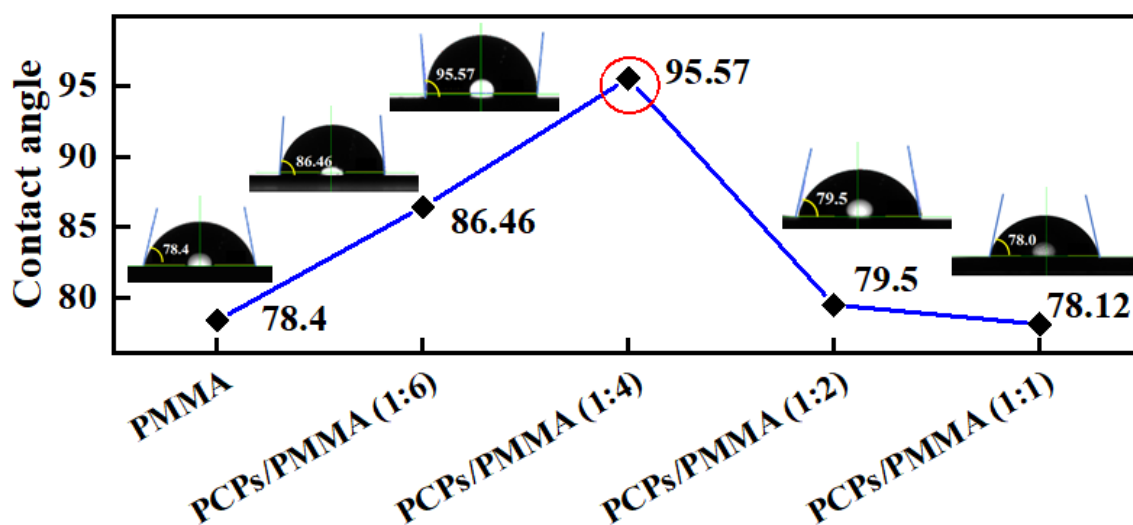


Figure 3.16. Contact angle of DI water droplet on (a) graphene, (b) PMMA film, (c) PCPs/PMMA 1:6 and (d) PCPs/PMMA 1:4.

Table 3.2. Contact angle of water droplet on Graphene, PMMA, PCPs/PMMA 1:6, PCPs/PMMA 1:4

| Sample | Graphene         | PMMA             | PCPs/PMMA 1:6       | PCPs/PMMA 1:4      |
|--------|------------------|------------------|---------------------|--------------------|
| CA     | $94.8 \pm 1.269$ | $78.35 \pm 0.21$ | $86.4667 \pm 0.499$ | $95.575 \pm 0.553$ |

Moreover, calculation of the energy adhesion between graphene and polymers provided more evidence to clear the existence of a weaker adhesion energy between

graphene and blend polymers compared with graphene and PMMA. Surface energy of graphene and the surface tension of the support polymers were calculated by the equations 3.13 and 3.14, respectively. Knowing these amounts, one can calculate the interfacial energy between graphene and support polymers by equation 3.11 and, subsequently determine the adhesion energy, which is  $E_A = -\gamma_{12}$  (table 3.3).

Table 3.3. Surface tension and surface energy, work adhesion between G-polymer

| Sample        | Surface tension and surface energy<br>$\gamma(mJ/m^2)$ | Adhesion energy between<br>G-polymer, $E_A(mJ/m^2)$ |
|---------------|--|---|
| G             | 50.64  | NA  |
| PMMA          | 42.5   | -0.35   |
| PCPs          | 13.22  | -12.11  |
| PCPs/PMMA 1:6 | 38.31  | -0.87   |
| PCPs/PMMA 1:4 | 36.64  | -1.13   |
| PCPs/PMMA 1:2 | 32.74  | -1.94   |
| PCPs/PMMA 1:1 | 27.86  | -3.37   |

- DFT Calculations:

The isosurface plots in Fig. 3.12 show the optimized structures of PCPs and PMMA dimer after DFT computations. This allows us to compare the two polymers and explain their attachment. Both polymers are overall neutral, but the overall distribution of charges is spread out in the case of PCPs (Fig. 3.12 (d)), this may be due to groups of two oxygen atoms at opposite ends of the dimer. In the case of PMMA (Fig. 3.12 (c)), the distribution of negative charges are concentrated on the four oxygen atoms that are close to one another.

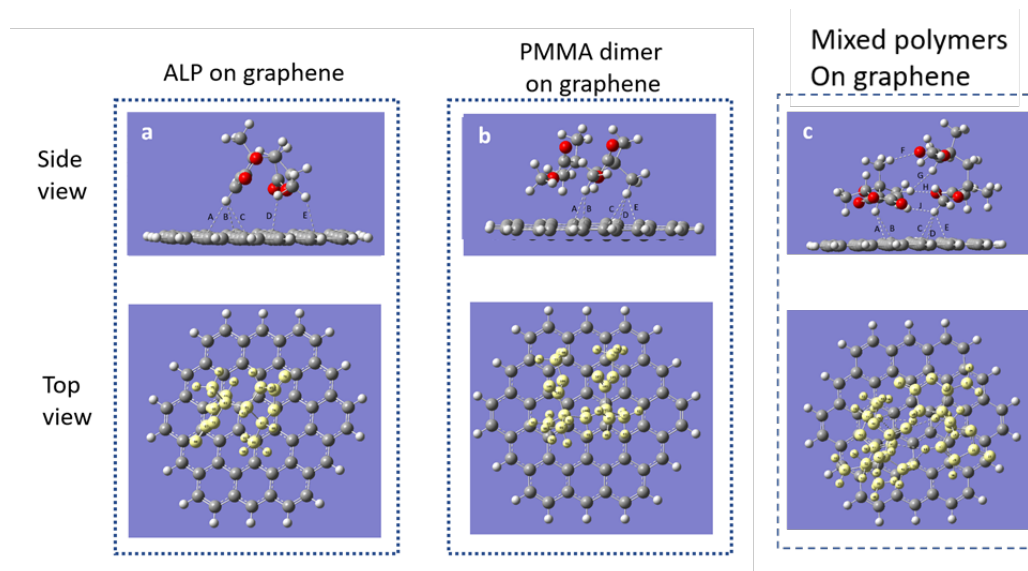


Figure 3.17. Attachment of PCPs and PMMA on hexagonal graphene flake with hydrogen-functionalized edges. Carbon atoms in grey, hydrogen atoms in white and oxygen atoms in red

Moreover, the DFT results show that hydrogen bonding occurs between the polymers and the simulated graphene flake in all three cases shown in figure 3.16. PCPs (Fig. 3.17 (a)) and PMMA Dimer (Fig. 3.17 (b)) show 5 points of hydrogen bonding with graphene. In the case of mixed polymers (Fig. 3.17 (c)) the PMMA dimer shows only 3 points with graphene and PCPs with 2 points with graphene and additional hydrogen bonding between the two polymers. The hydrogen bonding between the two polymers is thought to reduce the adhesion energy of the mixed polymers in graphene, thus enabling a cleaner transfer. Table (3.4)-(3.7) show the average hydrogen bonding lengths for each of the three cases simulated. The hydrogen bonding of PMMA dimer and PCPs without graphene (Fig. 3.18) was also studied and values are shown in table 3.8.

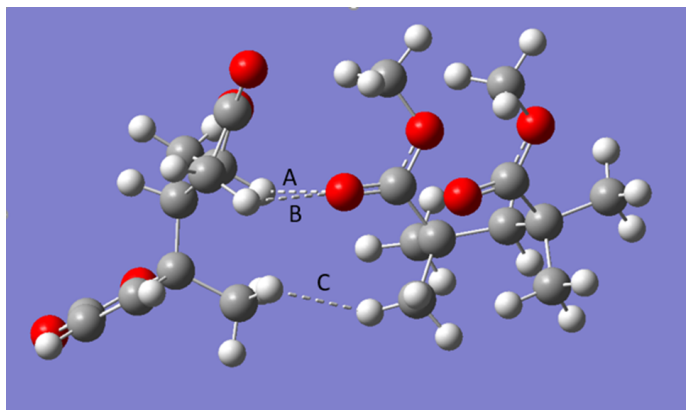


Figure 3.18. Optimized geometry according to DFT calculations of PMMA and PCPs. Carbon atoms in grey, hydrogen atoms in white and oxygen atoms in red.

Table 3.4. Hydrogen bond length of PCPs on graphene (Fig. 3.16 (a))

| Bond | Length (angstroms) | Atoms |
|------|--------------------|-------|
| A    | 2.77123            | C-H   |
| B    | 2.6848             | C-H   |
| C    | 2.80925            | C-H   |
| D    | 2.79164            | C-H   |
| E    | 2.71081            | C-H   |
| Avg  | 2.753546           |       |

Table 3.5. Hydrogen bond length of PMMA Dimer on graphene (Fig. 3.16 (b))

| Bond | Length (angstroms) | Atoms |
|------|--------------------|-------|
| A    | 2.75802            | C-H   |
| B    | 2.66773            | C-H   |
| C    | 2.71867            | C-H   |
| D    | 2.73782            | C-H   |
| E    | 2.72632            | C-H   |
| Avg  | 2.721712           |       |

Table 3.6. Hydrogen bond length of PMMA Dimer and PCPs on graphene (Fig. 3.16 (c))

| Bond | Length (angstroms) | Atoms |
|------|--------------------|-------|
| A    | 2.73983            | C-H   |
| B    | 2.78913            | C-H   |
| C    | 2.68645            | C-H   |
| D    | 2.720253           | C-H   |
| E    | 2.82784            | C-H   |
| Avg  | 2.7527006          |       |

Table 3.7. Hydrogen bond length between PCPs and PMMA Dimer (Fig. 3.16 (c))

| Bond | Length (angstroms) | Atoms |
|------|--------------------|-------|
| F    | 2.4197             | O-H   |
| G    | 2.28661            | H-H   |
| H    | 2.33307            | O-H   |
| J    | 2.34632            | H-H   |
| Avg  | 2.346425           |       |

Table 3.8. Hydrogen bond length between PCPs and PMMA Dimer (Fig. 3.18)

| Bond | Length (angstroms) | Atoms |
|------|--------------------|-------|
| A    | 2.44408            | O-H   |
| B    | 2.43981            | O-H   |
| B    | 2.35956            | H-H   |
| Avg  | 2.414483333        |       |

### 3.3.4 Conclusions

In conclusion, we evaluated the adhesion properties in graphene-polymer systems. The optimization of this process carried out for the purpose of achieving a green support polymer transfer. Our novel combination of polymers enabled us to transfer the graphene film onto a target substrate with minimal surface contamination and damage associated with the conventional PMMA support transfer. The graphene film transferred by PCPs/PMMA 1:4 ratio shows more extensive polymer removal and less structural damage, as indicated by SEM, AFM results compared to the

sample obtained by the conventional polymer support. According to KPFM results the PCPs/PMMA 1:4 ratio polymer support could bring about graphene transferred with superior electrical, optical and mechanical properties.

### **3.3.5 Recommendations for Future research**

PCPs polymer has a lower energy of adhesion that is still enough to attach to graphene. co-polymerization of PMMA and PCPs can be considered as environmental-friendly and biodegradable “green” polymers. Optimization of PCPs-PMMA polymer chain length can solve the problem of incomplete polymer residuals removal that many research groups currently are experiencing during graphene transfer.

# Chapter 4

## Aim two: Internal charge doping effects in vdW hybrid structures

### 4.1 Task one: Fabrication of graphene-MoS<sub>2</sub> vdW hybrids.

Among vdW heterostructures, graphene and the semiconducting transition-metal dichalcogenide MoS<sub>2</sub> have prompted intense research. According to previous reports, graphene was suggested to use as an interlayer electrode connecting 2D device platform with 3D electrodes, similarly how carbon nanotube electrodes in supercapacitors[108, 109]. In other research, some efforts have been made to implement a stacked graphene-MoS<sub>2</sub> junction in field-effect transistors (FETs), in which MoS<sub>2</sub> and graphene are used as a channel and source(S)-drain(D) electrodes, respectively. In FETs, an ohmic contact is usually desired for smooth current flows between semiconductors and S/D electrodes [110, 111]. In fact, a well matched metal-semiconductor is expected to bring down the contact resistance by decreasing the Schottky barrier height (SBH), which in turn increases the charge carrier injection rates [112]. Also, MoS<sub>2</sub> is not air-stable material, so stacking graphene on MoS<sub>2</sub> is able to protect MoS<sub>2</sub> against oxidation [113]. Here, we studied different arrangements of graphene and MoS<sub>2</sub> VdW heterostructures on SiO<sub>2</sub>/Si and Au substrate through different methods to achieve clean hybrid systems.

#### 4.1.1 Method and Materials

We fabricated four types of samples summarized in table 4.1.

1. Growth of MoS<sub>2</sub> on SiO<sub>2</sub>/Si

Table 4.1. Sample preparation and abbreviation.

| No.Sample                            | S1  | S2  | S3  | S4                                 |
|--------------------------------------|---|---|---|------------------------------------|
| Order of 2D material                 | Graphene-MoS <sub>2</sub> -SiO <sub>2</sub> /Si | Graphene-MoS <sub>2</sub> -SiO <sub>2</sub> /Si | MoS <sub>2</sub> -Graphene-SiO <sub>2</sub> /Si | Graphene-MoS <sub>2</sub> -Au      |
| Transfer method for graphene         | polysiloxane film/H <sub>2</sub> bubbling       | PMMA film/ H <sub>2</sub> bubbling              | PMMA film/ H <sub>2</sub> bubbling              | PMMA film/ H <sub>2</sub> bubbling |
| Transfer method for MoS <sub>2</sub> | Direct synthesis                                | Direct synthesis                                | Etching by KOH (wet transfer)                   | Etching by KOH (wet transfer)      |

One-step Chemical Vapor Deposition growth has been designed wherein MoO<sub>3</sub> and sulfur (S) precursors react in vapor phase to achieve a few layers of high quality MoS<sub>2</sub> Nano sheets (done in collaboration with Dr. Aravamudhan students). The growth substrates were silicon with 1μm layer of SiO<sub>2</sub> treated with Perylene-3,4,9,10-tetracarboxylicdianhydrid (PTCDA) aqueous solution which acts as a seeding molecule to trigger growth placed face down above a silica boat containing 15 mg of Molybdenum (VI) oxide (MoO<sub>3</sub>) powder. The silica boat covered with substrates was loaded into a 1- inch quartz tube together with another silica container holding 80 mg of sulfur powder. The container which holds sulfur is 18 cm from the container of MoO<sub>3</sub> and was placed upstream in the tube. The growth process occurred at atmospheric pressure with nitrogen gas flowing. The target temperature was 650° C at a rate of 15° C/ min held at 650° C for 15 min. Then, it was cooled down for at least five hours. MoO<sub>3</sub> was reduced by S vapors to form volatile sub-oxide species. S powder was placed in a separate quartz boat at the entrance of the furnace with temperatures slightly above ~ 100°C such that the powder sublimates readily. Moreover, it is crucial to consider a certain distance between S and MoO<sub>3</sub> boats to maintain a negligible concentration gradient for the substrates.

2. Transfer of 2D materials from their growth substrate to target substrate:
  - Graphene was transferred from Cu foil on MoS<sub>2</sub>-SiO<sub>2</sub>/Si substrate by our novel method, polysiloxane assistant film and H<sub>2</sub> bubbling, to fabricate sample S1.
  - Graphene was delaminated from Cu foil by conventional PMMA assistant polymer and H<sub>2</sub> bubbling to transfer on MoS<sub>2</sub>/SiO<sub>2</sub>/Si, SiO<sub>2</sub>/Si and MoS<sub>2</sub>/Au substrates for fabricating samples S2, S3 and S4, respectively.
  - MoS<sub>2</sub> was etched on the growth substrate by KOH solution, while protected by PMMA. After rinsing with DI water, MoS<sub>2</sub> transferred on Au substrate and finally PMMA was removed by acetone.

### 4.1.2 Characterization:

Raman and PL spectra were measured with XploRATM Confocal Raman microscope using a 532 nm excitation. The morphologies were analyzed using scanning electron microscopy (Zeiss Auriga FIB/FESEM).

### 4.1.3 Results and Discussions

Fig. 4.1 (a) shows optical image of S1 which is partially covered by graphene (right side), in which MoS<sub>2</sub> flakes are easily distinguishable underneath of monolayer graphene. The SEM image indicates a clean transfer of graphene on MoS<sub>2</sub> (Fig. 4.1 (b)). To prove it, we have done Raman spectroscopy. Fig. 4.1 (c) and (d) show the Raman peaks of graphene before and after transfer on MoS<sub>2</sub>, respectively. The 2D peak blueshifted due to gaining electron and undergoing compression from MoS<sub>2</sub>.

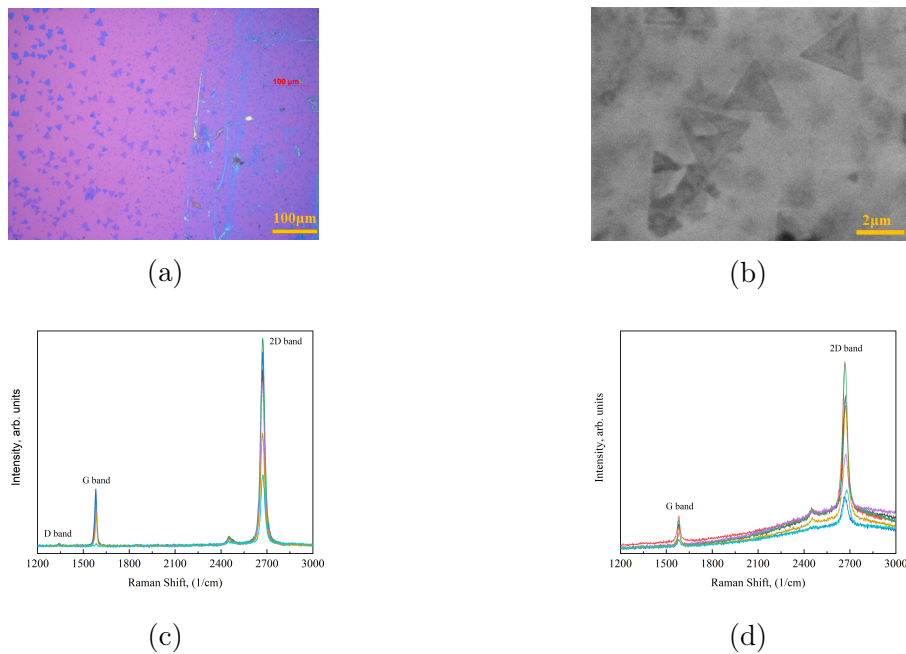


Figure 4.1. (a) and (b) Optical and SEM image of S1, respectively, and Raman spectroscopy of graphene (c) before and (d) after transfer on MoS<sub>2</sub>.

Fig. 4.2 (a,b) show SEM images of S2 before and after transferring graphene on the MoS<sub>2</sub> flakes with the area around 8 μm<sup>2</sup>, respectively. Despite some wrinkles and tears, the transfer was successful which Raman spectroscopy will verify it in the following. The distance between the E<sub>2g</sub><sup>1</sup> and A<sub>1g</sub> peaks is a proof of monolayer MoS<sub>2</sub> (Fig. 4.2 (c)). The effect of p-doping and strain after transfer of graphene is reflected by the blue shift of the A<sub>1g</sub> peak (Fig. 4.2 (d)). Raman spectroscopy of the graphene

in heterostructure revealed that graphene gained electron and slightly shifted to a lower wave number while the 2D peak shifted to a higher wave number (Fig. 4.2 (e)). Also, the sSNOM images indicate graphene prevents MoS<sub>2</sub> from oxidation that results in a significant increase of the durability this heterostructure (Fig. 5.5).

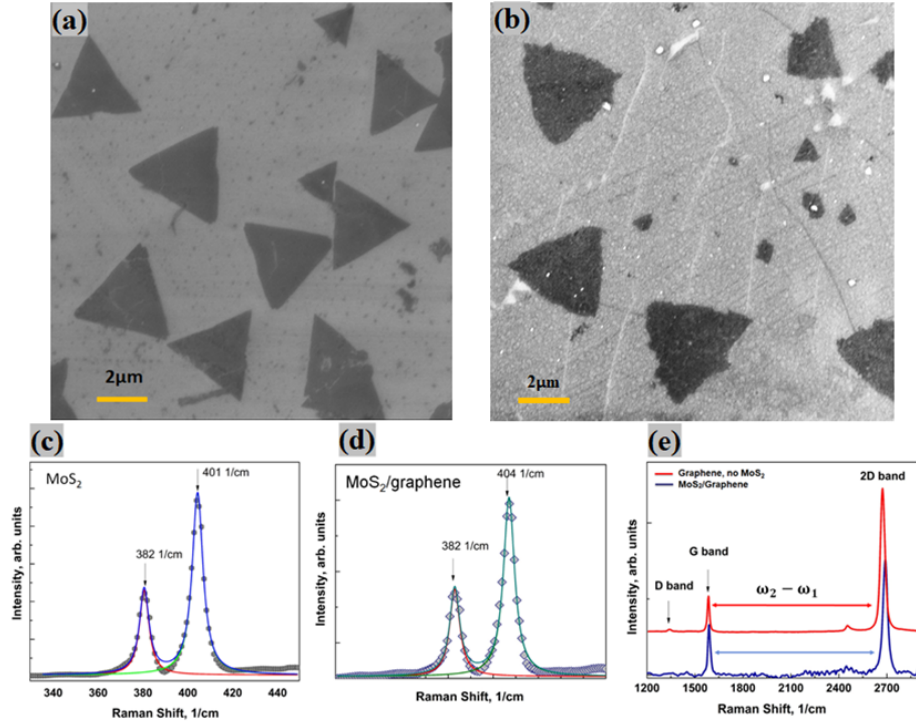


Figure 4.2. SEM images of S2: (a) before transfer of graphene, (b) after transfer of graphene, and Raman spectroscopy of S2: (c) MoS<sub>2</sub>, (d) MoS<sub>2</sub> covered by graphene and, (e) graphene and graphene on MoS<sub>2</sub>.

Fig. 4.3 (a) shows the SEM image of S3 which indicated a successful transfer on graphene. Raman spectrum of this sample (Fig. 4.3 (b)) indicate the  $A_{1g}$  peak shifted to a higher wave number, while the  $E_{2g}^1$  peak did opposite because of losing electron to graphene. But the G peak blueshifted and the 2D peak redshifted respectively, which indicates the graphene gained electron and underwent compression.

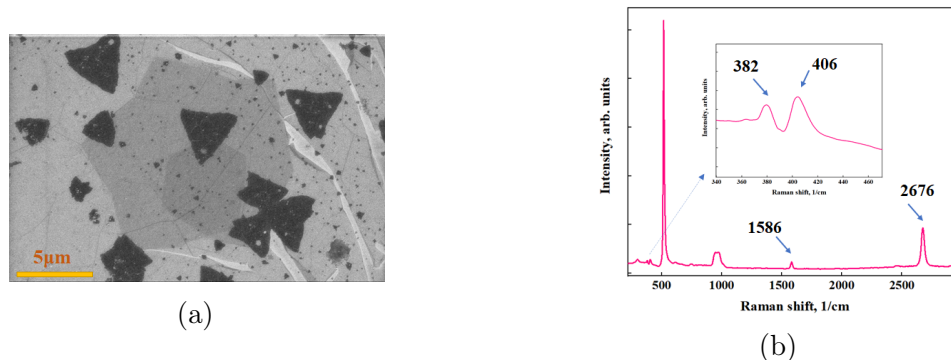


Figure 4.3. (a) SEM image and (b) Raman spectroscopy of S3.

The SEM images of S4 before and after transferring the graphene are shown in Fig. 4.4 (a,b) that indicates successful transfer despite some cracks on graphene. Raman spectra of this sample indicates the  $E_{2g}^1$  and  $A_{1g}$  peaks shifted to a lower and higher wave number, respectively, because  $\text{MoS}_2$  lost electron. On the other hand, graphene gained electron, which was reflected in the blue shift of the graphene peak. Notably, both graphene and  $\text{MoS}_2$  underwent compression.

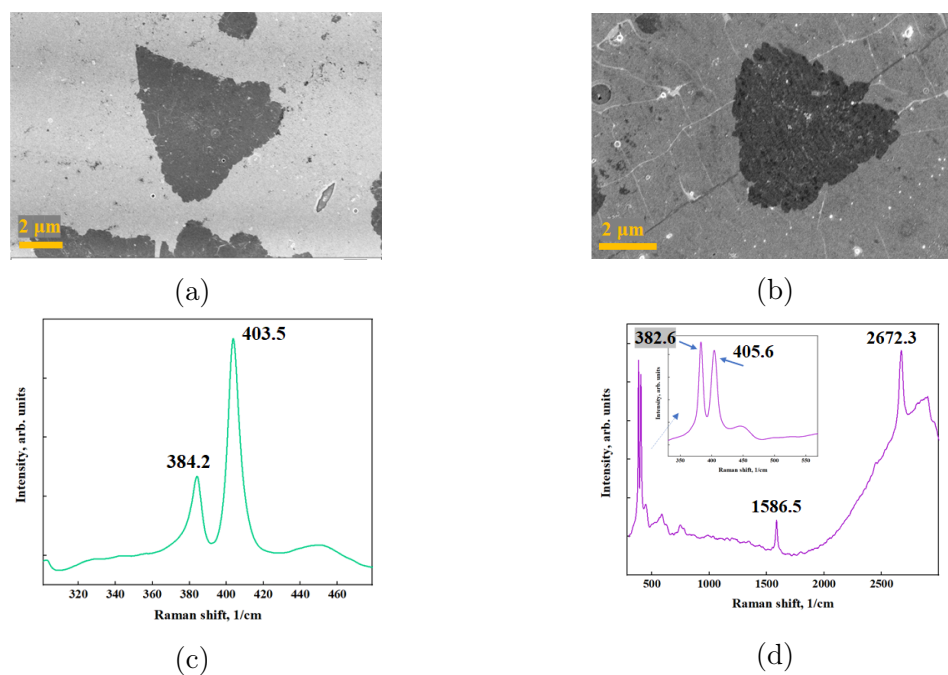


Figure 4.4. SEM images of S4 (a) before transferring graphene (b) after transferring graphene. (c) and (d) are Raman spectroscopy of  $\text{MoS}_2$  before and after graphene coverage.

#### 4.1.4 Conclusions

In conclusion, successful fabrication of vdW heterostructures was reported. We investigated different fabrication methods and designed different architectures for produced samples.

#### 4.1.5 Recommendations for Future Research

The combination of exfoliation and transferred methods, which I have developed during my research, can bring about new heterostructures for the different applications.

### 4.2 Task two: Investigating internal charge doping effect in vdW hybrid structures.

The combination of two or more 2D materials in vertically arranged stacks creating vdW heterostructures which open an avenue to new physical phenomena, which do not exist in mono 3D or mono 2D systems [114]. These include but not limited to: charge and spin density waves [115], topological insulator states [116], light trapping [117], etc. The interlayer interactions in vdW heterostructures play a fundamental role resulting in band structure modulation. Charge transfer between the encapsulated 2D layers can be very significant and influence electronic properties of potential optoelectronic devices [118, 119].

However, the mechanism of interlayer interactions is still unclear despite numerous research in this area. A comprehensive analysis of the electronic band structure of particular configuration is needed. When 2D materials are in close contact with each other, work function (WF) difference results in the charge transferring and the interface dipole inducing. Thus, the Fermi level shifts, and it consequently leads to a work function modulation. In this respect, having control over the WF of 2D components is crucial because it affects the performance of the potential devices. Here, we focus on the study of the band alignment at the graphene-MoS<sub>2</sub> vdW heterostructures.

#### 4.2.1 Method

- The scanning amplitude modulation (AM) Kelvin Probe Force

The scanning amplitude modulation (AM) Kelvin Probe Force Microscopy was used to investigate the band alignment in the graphene-MoS<sub>2</sub> VdW heterostructures. This technique allows us to create of a map of the sample's surface potential, then recalculate to work function map, with the 10 nm lateral resolution and potential resolution depending on bandwidth of preamplifier (in our case, below 10 mV). The

AFM room is equipped with climate control capabilities, keeping constant temperature and humidity over the time of the experiment. Indeed, KPFM is an electrical AFM mode which measures contact potential difference (VCPD) with respect to the Ir/Pt coated AFM tip.

$$V_{CPD} = (WF_{tip} - WF_{sample})/e \quad (4.1)$$

Prior to each set of the experiments, the WF of the tip was calibrated with freshly cleaved highly oriented-pyrolytic graphite (HOPG) at ambient conditions. This value was used for the sample WF calculations:

$$V_{CPD} = (WF_{tip} - WF_{HOPG})/e \quad (4.2)$$

In fact, HOPG doesn't form interface dipoles with ambient contaminations on the surface such as hydrocarbon, waters, etc., because it is chemically inactive[120]. The KPFM measurements are done in dual-pass regime: during the first pass the instrument is measuring topography of the sample surface in tapping mode, during the second pass the AFM tip is hold on distance  $z$  above the surface. To measure VCPD the electrostatic field is created by applying AC voltage between tip and sample (VAC) during second pass and a lock-in amplifier tracks variations in the response amplitude. An additional DC bias (VDC) is applied to the tip, that the force is minimized when  $V_{DC} = V_{CPD}$ . The electrostatic force is related to the capacitance  $C$  between AFM tip and the sample:

$$F_E = \frac{1}{2} \frac{\partial C}{\partial z} (\Delta V)^2 \quad (4.3)$$

Here, the potential difference between the tip and the sample  $\Delta V = V - V_{CPD}$ .  $V$  is the sum of all externally applied voltages to tip or sample. As a result, with both AC voltage and a constant bias,  $V = V_{DC} - V_{AC} \times \sin(\omega_E t)$ , the resulting electrostatic force can be divided into one static and two dynamic spectral components:

$$F_{static} = \frac{1}{2} \left( \frac{\partial C}{\partial z} [(V_{DC} - V_{CPD})^2 + V_{AC}^2/2] \right) \quad (4.4)$$

$$F_{\omega_E} = \frac{\partial C}{\partial z} (V_{DC} - V_{CPD}) V_{AC} \sin(\omega_E t) \quad (4.5)$$

$$F_{2\omega_E} = \frac{1}{4} \frac{\partial C}{\partial z} V_{AC}^2 \cos(2\omega_E t) \quad (4.6)$$

The  $F_{\omega_E}$  is describing AM-KPFM: when  $V_{DC} = V_{CPD}$ , the response at frequency  $E$  vanishes. In AM-KPFM, a feedback loop minimizes the response amplitude by adjusting  $V_{DC}$  [121].

- Calculation of charge density in monolayer graphene and in MoS<sub>2</sub> monolayer

The energy dispersion relation of MoS<sub>2</sub> is defined by:  $E = E_c + \hbar^2 k^2 / (2m^*)$ . Also the density of states (DOS) for each band is given by  $2m^* = (2/\pi\hbar^2)$  carrier density in 2D materials is defined by:

$$n = \int_{E_c}^{E_{top}} f_0(E) D_{2D}(E) dE dx \quad (4.7)$$

$$f_0(E) = \frac{1}{1 + \exp((E - E_F)/K_B T)} \quad (4.8)$$

$$D_{2D}(E) = g_v m_n^* / \pi \hbar^2 \quad (4.9)$$

So on the Fermi level (spin and valley degeneracy included) is defined by:

$$n_F = \frac{2m^* kT}{\pi \hbar^2} \log(1 + \exp[\frac{F - E_c}{kT}]) = N_c \log(1 + \exp[\frac{|E_c| - |F|}{kT}]) \quad (4.10)$$

where F is Fermi level and  $E_c = 4.21$  eV, respect to the vacuum level.

The conduction band DOS is given by:

$$N_c = \frac{2m^* kT}{\pi \hbar^2} = \frac{2m^*}{m_o} \frac{kT}{\pi a_B^2 E_B} \simeq 7.610^{12} cm^{-2} \quad (4.11)$$

with  $m_o$  being the free electron mass,  $a_B = 0.53$  Å,  $E_B = 27$  eV, and effective mass in MoS<sub>2</sub> is taken to be  $0.35m_o$ .

if non-degenerate doping ( $|F| > |E_c|$ , i.e., Fermi lever is place below conduction energy level) then  $\log(1 + x) \simeq x$  so n equals to:

$$n = N_c \exp[-\frac{|F| - |E_c|}{kT}] \quad (4.12)$$

if degenerate doping ( $|E_c| - |F| \gg kT > 0$ , Fermi level is within the CB), then the charge density is linear dependence on the Fermi level. So n by approximately is equal to:

$$n \simeq N_c \frac{|E_c| - |F|}{kT} \quad (4.13)$$

As the charge carriers in graphene obey a linear dispersion relation  $E = \hbar v_F k$ , we derive:

$$n_g(F) = \frac{(E_D - F)^2}{\pi \hbar^2 v_F^2} = N_g (E_D - F)^2 \quad (4.14)$$

where the Dirac point  $E_D = 4.57$  eV, and Fermi velocity  $v_F \simeq 1.16 \times 10^6$  m/s and  $N_g \simeq 5.4610^{13} cm^{-2} eV^{-2}$ .

When 2D materials are in contact with an insulated substrate (e.g.  $SiO_2$ ) they are electrically isolated, causing a floating potential, leading to the charge transfer which generates 2D charge densities  $\pm en_1$ , equal (by magnitude and opposite by sign) in both layers, and generates  $2\delta V$ , a potential difference between TMDC and monolayer graphene ( $\varphi(z \pm d/2) = \pm\delta V$ ).

This potential difference is linearly proportional to the surface charge formed at each of the materials, as the result of charge transfer. Then, the positions of the Fermi levels, both defined with respect to the higher vacuum level in monolayer graphene, are:

where the differences:  $\delta F = F_g^o - F > 0$  is the Fermi level (up)shift in graphene, which can be measured as work function difference taken on and off the TMDC island, and  $\delta F_{MoS_2}$ , the Fermi level (down)shift in  $MoS_2$ .

When we know the expression of DOS of  $MoS_2$  and graphene, it leads to calculating the charge transfer and potential difference between them when they are in contact with each other in vertical heterostructure form.

## 4.2.2 Results and Discussion

The most important rule when a heterojunction is formed that the Fermi levels must line up at equilibrium (no external bias) due to contact potential between two objects coming into contact. This contact potential is related to the difference in the work functions. In fact, electron moves from layer with lower work function to one with higher work function.

KPFM characterization of monolayer graphene transferred on  $SiO_2/Si$  substrate is shown on Fig.4.5a. The graphene WF profile is flat and in a good agreement with previously reported value of 4.715 eV [122]. The WF of  $MoS_2$  on original growth substrate is highly dependent number of layers, level of oxidation, inclusions of seed nanocrystals (partially sulfurized molybdenum oxide rhomboid crystals), and grain boundaries. Fig. 4.5c presents the “freshly cooked”  $MoS_2$  WF variation over a single flake with the mean value 4.67 eV. The height of the flake suggest that sample is trilayer  $MoS_2$ [123]. The presented data is in good agreement with previously published results. Upon decreasing number of layers,  $MoS_2$  WF increase up to value 5.12 eV for single layer[124].

In the (monolayer graphene - monolayer  $MoS_2$ ) VdW heterostructure, we found significant modulation of the graphene WF activated by  $MoS_2$  charge doping effect and strongly dependent on  $MoS_2$  internal properties/quality. Fig.4.5 (b) show the Fermi level diagram before and after junction of pure monolayer graphene and  $SiO_2/Si$ . Graphene is p-doped as our Raman characterization confirm (Fig. 4.2), While  $MoS_2$  on  $SiO_2/Si$  Fig.4.5 (d) is n-doped.

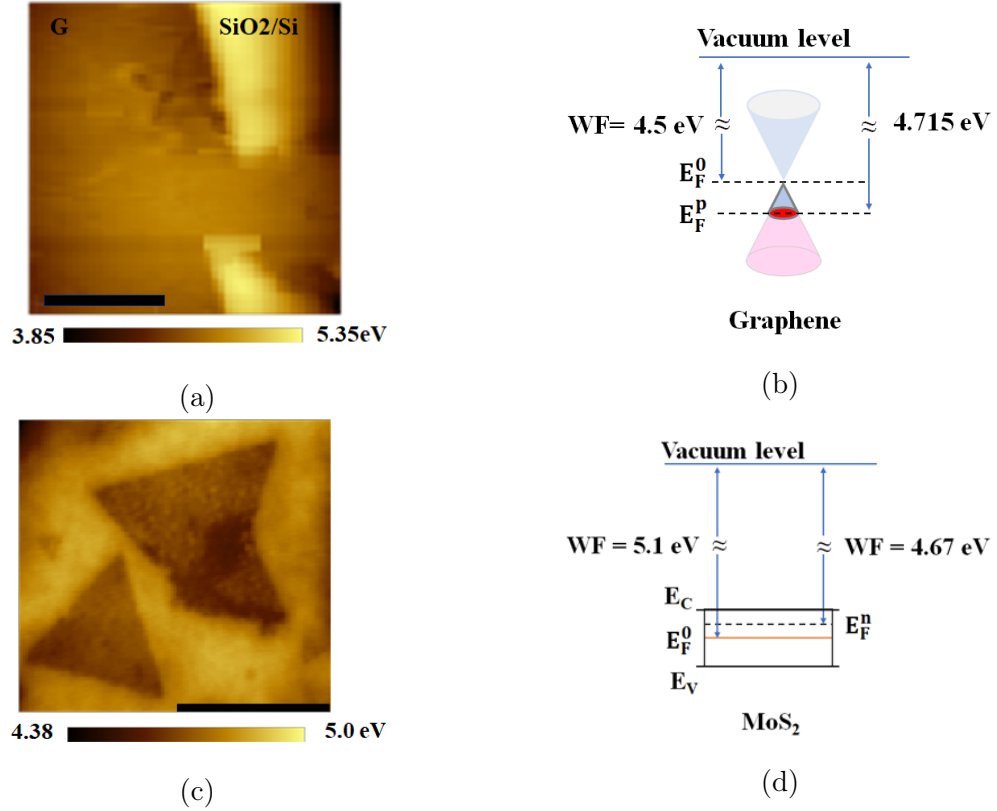


Figure 4.5. KPFM of Graphene-SiO<sub>2</sub>/Si (a), electronic band structure energy diagram of graphene (c), KPFM of MoS<sub>2</sub>-SiO<sub>2</sub>/Si (d), and electronic band structure energy diagram of MoS<sub>2</sub>.

Fig. 4.6 is an example of WF modulation of graphene on the top of MoS<sub>2</sub> which is decreased to 4.617 eV due to charge doping effect and increased 4.632 eV on top of the MoS<sub>2</sub> oxidized spots (line profiles Fig. 4.6 (d,e)). Outside of MoS<sub>2</sub> area, graphene shows standard p-doped value of  $\sim 4.6$  eV. Our findings are consistent with other studies. Pendy et.al., reported the electrical structure of graphene/MoS<sub>2</sub> vertical heterostructure underwent some charge depletion and accumulation at the interface of 2 layers because of redistribution of charge density from graphene toward MoS<sub>2</sub> even without applying pressure graphene became p-doped[125].

These results are extremely important to study minimization the contact resistance of the metal/MoS<sub>2</sub> junction for MoS<sub>2</sub>-based devices. Among the common contact metals with MoS<sub>2</sub>, we can note Pd with the work function for different crystal orientation ranges from 5.12 eV to 5.9 eV[112] and Au with work function of 5.1 eV[109] (5.10 – 5.47) that both of them have the work function more than graphene. It is worth noting that Nucleation spots, oxidized edges of MoS<sub>2</sub>, and molybdenum oxysulfide crystals in heterostructure area tune graphene WF to the lowest value ( $\sim$

4.67 eV). It could be explained by oxygen electronegativity. Consequently, the case of oxide bonds are less covalent than metal-chalcogen bonds and the decrease covalency leads to short (narrow) valence and condition bands with an energy gap generally wider than MoS<sub>2</sub>[7].

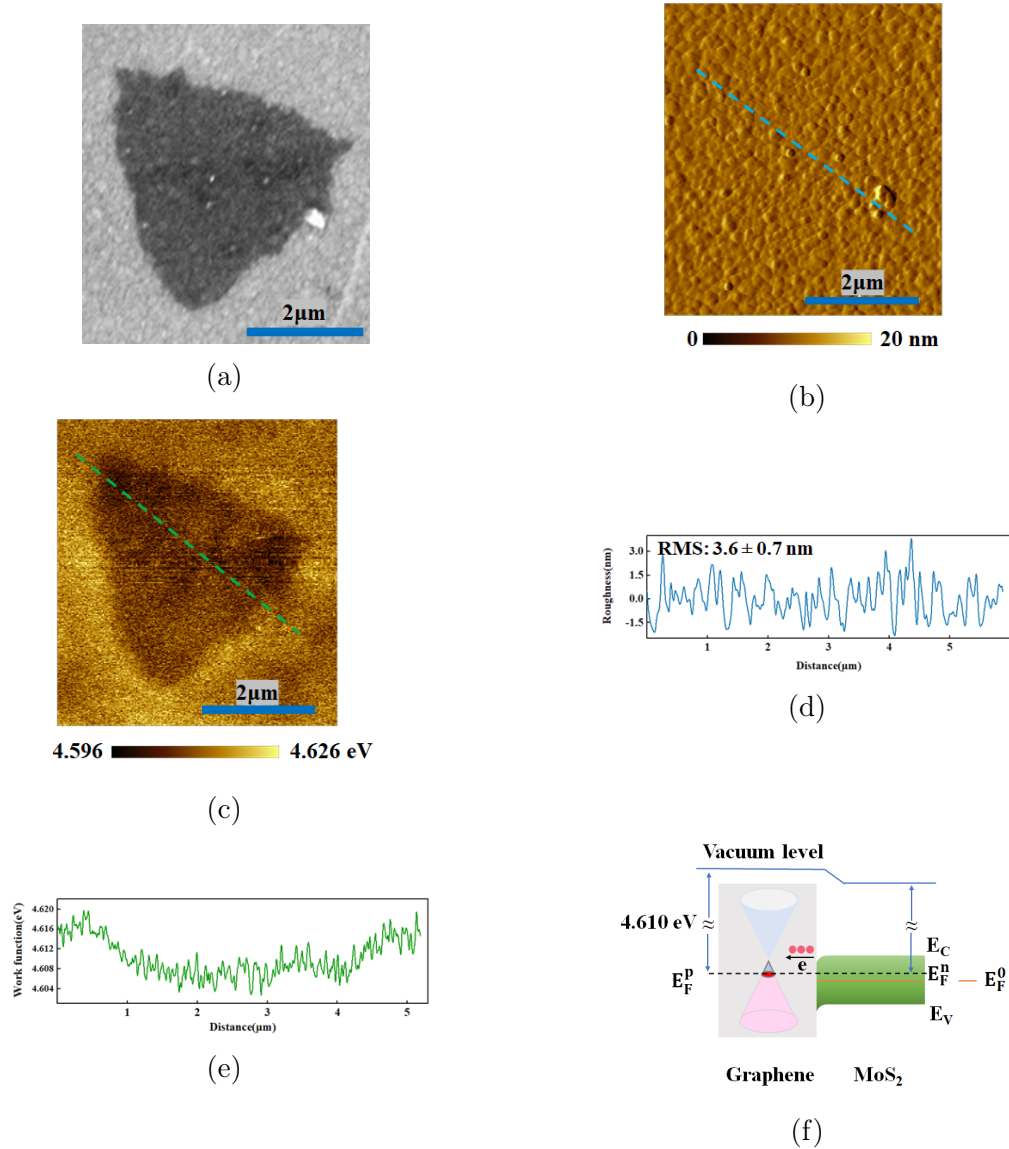


Figure 4.6. SEM image (a), AFM map (b), and KPFM map (c) of Graphene-MoS<sub>2</sub>-SiO<sub>2</sub>/Si. Corresponding line profile of AFM and KPFM (d) and (e), respectively. Electronic band structure energy diagram of heterostructure of graphene and MoS<sub>2</sub> (f).

Fig. 4.7 (a,b) show the SEM and AFM topography of graphene/MoS<sub>2</sub> hybrids on SiO<sub>2</sub>/Si substrate. All area is completely covered with graphene. Monolayer MoS<sub>2</sub> flakes are invisible in AFM topography since the SiO<sub>2</sub> surface roughness ( $3.6 \pm 0.7$  nm according to RMS analysis in Fig 4.7 (d)) is dominating over MoS<sub>2</sub> thickness (0.8 nm) and graphene perfectly conforms the underlying substrate [126,127]. This effect is common result of SiO<sub>2</sub> etching during CVD growth of MoS<sub>2</sub>. The surface also contains nucleation seeds (10-20 nm) of molybdenum oxysulfide like MoS<sub>2</sub>O or MoO<sub>2</sub>S as crystalline intermediates in stepwise sulfurization of MoO<sub>3</sub> to the final product of MoS<sub>2</sub> but remain on substrate due to sulfur vapor deficiency [128,129]. To study work function, we considered both graphene and MoS<sub>2</sub> as an individual 2D in a Vander Waals heterostructure (Fig. 4.7 (c)). While work function of Graphene and MoS<sub>2</sub> on SiO<sub>2</sub>/Si were 4.715 eV and 4.67 eV, respectively (SiO<sub>2</sub>  $\sim$  5 eV) and are in agreement with other reports that work function values of monolayer graphene supported on SiO<sub>2</sub> (with no gate bias) vary significantly from 4.2 eV to 5.1 eV, with a commonly accepted range of 4.5–4.6 eV [129]. Work function of graphene on MoS<sub>2</sub> decreased to  $4.608 \pm 0.004$  eV and graphene around of the heterostructure was calculated 4.620 eV as it can be seen in line profile (Fig. 4.7 (e)). These results confirm the tuning of graphene work function in heterostructure. Fig. 4 (f) shows the energy band diagram of heterostructure of graphene and MoS<sub>2</sub>.

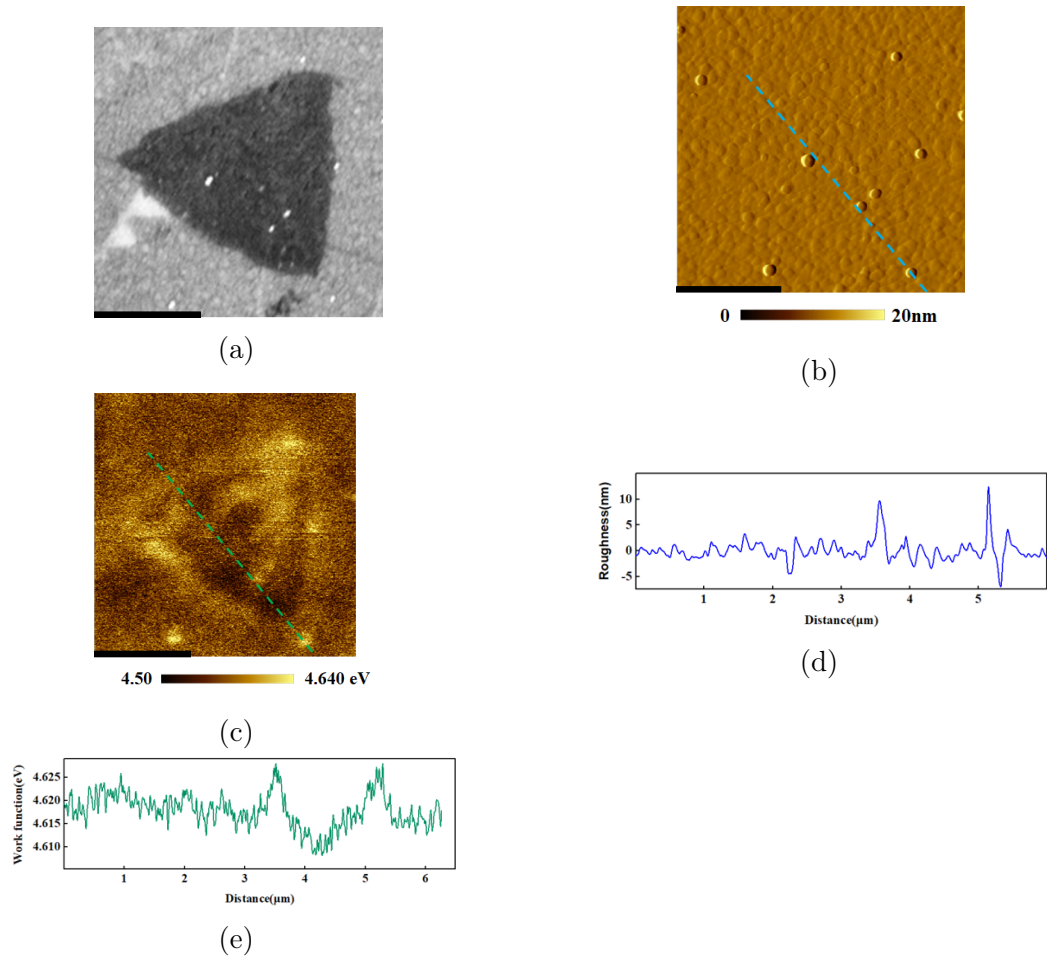


Figure 4.7. SEM image (a), AFM map (b), and KPFM map (c) of Graphene-MoS<sub>2</sub>-SiO<sub>2</sub>/Si. Corresponding line profile of AFM and KPFM (d) and (e), respectively

### 4.2.3 Conclusions

Heterostructure of a few layers of graphene/MoS<sub>2</sub> has been demonstrated as a promising candidate for diverse unique optoelectronic devices. The tunable Fermi level in graphene allows excellent work-function match with MoS<sub>2</sub>, resulting in low contact resistance. Here, the lateral redistribution of charge transfer with nanoscale resolution were investigated in a graphene/MoS<sub>2</sub> heterostructure. Hence, confocal Raman spectroscopy showed the strain and p-doping of graphene. Also, by KPFM mapping, I identified the direction of charge transfer in graphene/MoS<sub>2</sub> heterostructure.

#### 4.2.4 Recommendations for Future research

As our KPFM measurement was carried out in ambient condition, studying the effect of water meniscus formation between KPFM tip and the 2D material allows one to understand the effect of humidity in charge redistribution in the interface of 2D material in vdW heterostucture (i.e., diminishing  $\Delta\text{CPD}$ ).

# Chapter 5

## Aim three: External doping on two dimensional interface

### 5.1 Task one: Study the chemical doping and photo etching interaction in 2D MoS<sub>2</sub>.

MoS<sub>2</sub> is one of the most studied two-dimensional layered semiconductor TMDCs, having gained great attention due to its electronics and optoelectronics applications. Sulfur vacancies are the most common defects represented by dangling bonds which provide more chemically active sites than the perfect MoS<sub>2</sub> does [130]. The Photoluminescence (PL) of MoS<sub>2</sub> undergoes the quenching and broadening because of the present of these defective states [131–133]. The sulfur vacancies significantly change the electronic structure of MoS<sub>2</sub> through the free-charge carrier trap and exciton generation.

In the absence of sulfur vacancy, K and K' point Brillouin zone for the MoS<sub>2</sub> lattice are the host-site for exciton A and B around 1.8 eV and 2 eV, respectively. Sulfur vacancies lead to creating a three-body bound state called a trion (A<sup>-</sup>), arising from the exciton (A) interacting with the free-charge carriers. According to previous reports, reducing the electron density leads to enhancement of the PL of monolayer MoS<sub>2</sub> due to the conversion from excitons to trions [134, 135]. Manipulating the carrier concentration can be carried out by employing several methods such as electrical gating, ionic-liquid gating [136], gas physisorption [134, 137], and chemical doping [138, 139], laser photodoping [140, 141].

One of the well known p-type dopants is 2,3,5,6-tetrafluoro-7,7,8,8-tetracyanoquinodimethane (F4TCNQ), which is used to control carrier concentration in various semiconductors. F4TCNQ is a strong organic electron-acceptor because it has a close proximity of the lowest unoccupied molecular orbital (LUMO) level of 5.2 eV to the highest occupied molecular orbital (HOMO) level of many semiconductors [142].

To calculate the carrier concentration in TMDC systems, J. Ross et al., introduced a model called Mass Action [143]. Using a steady state model of all the particles in their system and the law of action, they found an equation between carrier concentration and the relative intensity of the photoluminescence (PL) signals.

the free-electron concentration ( $n$ ) can be approximated by the law of action

$$n = N_c \exp\left[-\frac{E_c - E_F}{KT}\right] \quad (5.1)$$

, where  $E_c$  is the energy of the conduction band,  $E_F$  is the energy of the Fermi level,  $k$  is the Boltzmann constant,  $T$  is the temperature in kelvins,  $N_c$  is the effective density of states at the conduction band edge given by  $N_c = 2\left(\frac{2\pi m_e^* kT}{h^2}\right)^{3/2}$  with  $m_e^*$  being the electron effective mass and  $h$  being Planck's constant.

from here for trions we have

$$\frac{n_A n_c}{n_{A^-}} = N_t K_B T \exp\left(\frac{-E_T}{k_B T}\right) \quad (5.2)$$

, where  $E_T$  is the trion binding energy  $\sim 20$  meV [144] and  $N_t = \frac{4M_A m_e}{\pi h^2 M_{A^-}}$ . The effective mass of electron is  $m_e = 0.35 m_o$  and the effective mass of holes is  $m_h = 0.45 m_o$ . The  $m_o$  is the free electron mass. The effective masses of an exciton and trion can be calculated as  $m_A = m_e + m_h = 0.8m_o$ , and  $m_{A^-} = 2m_e + m_h = 1.15m_o$ .

We denote  $n_A, n_{A^-}$  and  $n_e$  for the concentration of  $A, A^-$  and free electrons.

Then, the trion PL intensity is related to the excess electron concentration  $n_e$ :

$$\frac{I_{A^-}}{I_{total}} = \frac{\beta n_e}{1 + \beta n_e} \quad (5.3)$$

here,  $\beta$  is a constant, equal to  $4 \times 10^{-14}$  cm<sup>2</sup>. Using this model, we can calculate the electron concentration before and after doping:

$$n_e = \frac{1}{\beta} \left( \frac{I_{A^-}}{I_{total} - I_{A^-}} \right) \quad (5.4)$$

Also, light can locally modulate optoelectronic properties of MoS<sub>2</sub> [145] and the number of photogenerated electrons created by laser exposure is

$$n_{ph} = \frac{Pt\lambda}{hc} \quad (5.5)$$

, where  $P$  is the laser power,  $t$  is the laser exposure time,  $\lambda$  is wavelength of the laser,  $h$  is Planck's constant and  $c$  is the speed of light in vacuum.

Here, we used the organic solution of F4TCNQ to chemically p-dope the defect sites in order to control the carrier concentration and modulate the bandgap of MoS<sub>2</sub>, consequently enhance the efficiency of light emission. To study the band alignment of

2D MoS<sub>2</sub> before and after doping we used Kelvin Probe Force Microscopy (KPFM). We also investigated the modulation of carrier concentration under light irradiation by PL.

### 5.1.1 Materials and Methods

High quality 2D MoS<sub>2</sub> samples were grown at 650° C on Si/SiO<sub>2</sub> substrates using a home-built CVD setup with a one-inch quartz tube fitted in Lindberg furnace equipment. Then, the sample was soaked in a mixed solution of 0.3 μm/ml of 2,3,5,6-tetrafluoro-7,7,8,8-tetracyanoquinodimethane (F4TCNQ) in Chloroform.

### 5.1.2 Characterizations

The samples were imaged with a scanning electron microscope (Zeiss Auriga FIB/FESEM), using an accelerating voltage of 5 kV, and a working distance of 5 mm. To obtain an AFM topographic image, the sample is scanned by an Oxford Research AFM (MFP-3D infinity) instrument using the tapping mode under ambient conditions, and Si tips coated with Al (TAP300AL-G probe, Budget Sensors) was used. Contact potential difference (CPD) at the graphene was measured by Kelvin probe force microscopy (KPFM) using amplitude modulation (AM-KPFM). Here, graphene was probed by a conductive Pt/Ir-coated tip (EFM, Nanoword) while silver paint used for grounding. PL spectra was obtained using Horiba XploRa Raman Confocal system with 532 nm laser excitation wavelengths.

### 5.1.3 Results and Discussion

SEM images of MoS<sub>2</sub> sample shows the topography of triangular flakes with area  $\sim 8\mu^2$  (Fig.5.1 (a)). To quantify the surface topography, AFM height images were taken for the 25 μ<sup>2</sup> area. The profile lines along the dashed lines indicate the thickness variation of MoS<sub>2</sub> flak. The SiO<sub>2</sub> surface roughness ( $3.6 \pm 0.7$  nm according to RMS analysis in Fig.3. (d)) is dominating over MoS<sub>2</sub> thickness (0.8 nm) [126, 127]. This effect is common result of SiO<sub>2</sub> etching during CVD growth of MoS<sub>2</sub>. The surface also contains nucleation seeds (10-20 nm) of molybdenum oxysulfide like MoS<sub>2</sub>O or MoO<sub>2</sub>S as crystalline intermediates in step wise sulfurization of MoO<sub>3</sub> to the final product of MoS<sub>2</sub> but remain on substrate due to sulfur vapor deficiency [128, 129].

Fig. 5.1 (c) illustrates that CPD of as-grown MoS<sub>2</sub> sample varies from one flake to another. It indicates that different flakes has different charge carrier concentration, stemming from present of different number of layers, defect sites, nucleation seeds and molybdenum oxysulfide. According to the CPD profile lines along with two dashed lines and table 4.1, the CPD of three different flakes lay within a range of 0.44-1.13 V. After doping the sample, CPD map demonstrates charge Carrier concentrations of

top of MoS<sub>2</sub> confronted with a significant reduction. As the analysis of the CPD in table 5.1 shows, the CPD of doped sample has lower difference in comparison with as-grown sample, i.e., KPFM is sensitive to the surface variations, one can distinguish the differences of CPD of MoS<sub>2</sub> Flakes before doping. However, after doping the CPD of the different layers equalized and all the flakes show a loss of contrast in CPD.

According to previous reports, the KPFM measurement of as-grown sample indicates MoS<sub>2</sub> is natively n-type and the Fermi level shifted towards conduction band. Because the intrinsic structural defects (sulphur vacancies) exist in on CVD grown 2D MoS<sub>2</sub> on Si/SiO<sub>2</sub> [146, 147]. The incubation effect of p-dopant F4TCNQ on as-grown sample led the Fermi energy shifted towards the center of bandgap by only 570, 220 and 1000 meV. Density functional theory calculations (DFT) showed that the interactions between organic molecules (F4TCNQ) and the pristine MoS<sub>2</sub> surface is relatively weak adsorption [148]. Hence, the Fermi level shift is ascribed to interaction between F4TCNQ and the MoS<sub>2</sub> defect sites.

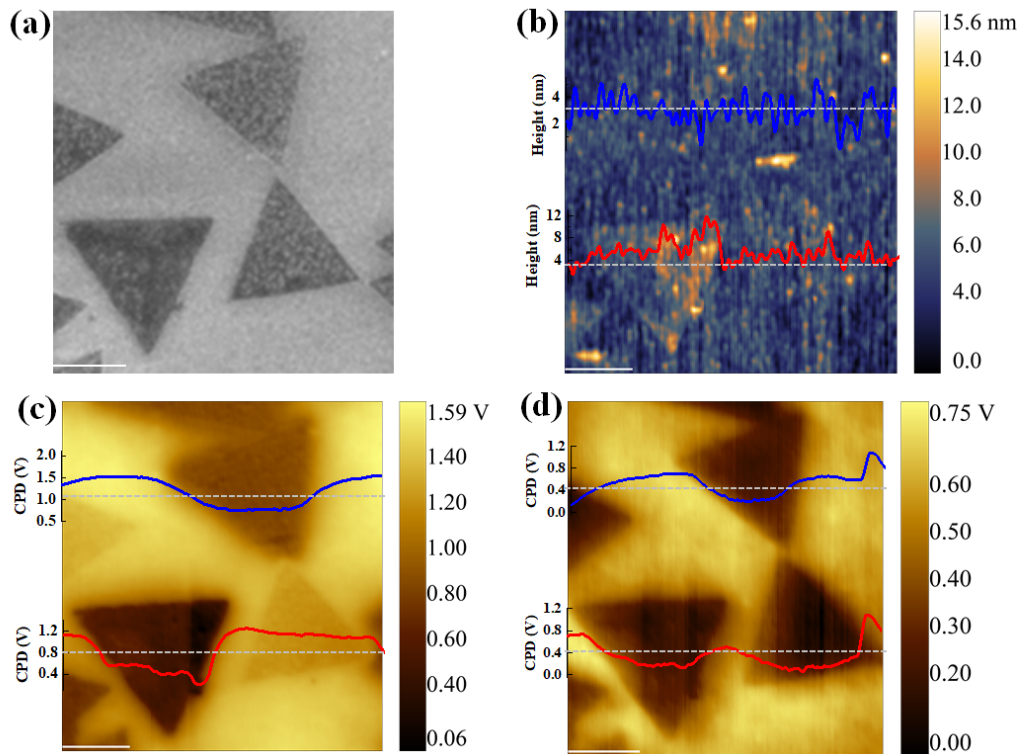


Figure 5.1. (a) Scanning Electron Microscopy image (SEM) of MoS<sub>2</sub> sample (b) AFM and height profile lines (c) KPFM surface potential map of sample as-prepared and CPD profile lines (d) KPFM surface potential map after chemical doping and CPD profile lines.

Table 5.1. CPD of as-grown and doped  $\text{MoS}_2$  flakes

| Number of flakes | $CPD_{as-grown}(V)$ | $CPD_{doped}(V)$ | $\Delta CPD(mV)$ |
|------------------|---------------------|------------------|------------------|
| I                | 0.78                | 0.21             | 570              |
| II               | 0.44                | 0.22             | 220              |
| III              | 1.13                | 0.13             | 1000             |

In addition to chemical doping we exposed the  $\text{MoS}_2$  flakes to the laser exposure. In fact, the laser excitation leads to photo-doping effects. The SEM images of  $\text{MoS}_2$  sample shows the topography of triangular flakes with area  $\sim 8\mu^2$  (fig.5.2a). To quantify the surface topography, AFM height images were taken for the  $5\mu^2$  area. The CPD maps before and after chemical and photo doping demonstrate the reduction of charge carrier concentration of different flakes. According to table the  $\delta CPD$  lies within the range of 100-400 mV. The KPFM measurements confirmed that the laser enhanced-doping led to a photodoping effect, resulting in the redistribution of carriers and consequentially the Fermi level shifts and modulate the work function. The KPFM measurement confirmed that chemical and photo doping caused a shift in the Fermi level (closer to the center of energy gap) and, consequently, an increase in the  $\text{MoS}_2$  work-function (  $WF \sim 100 - 400meV$  )

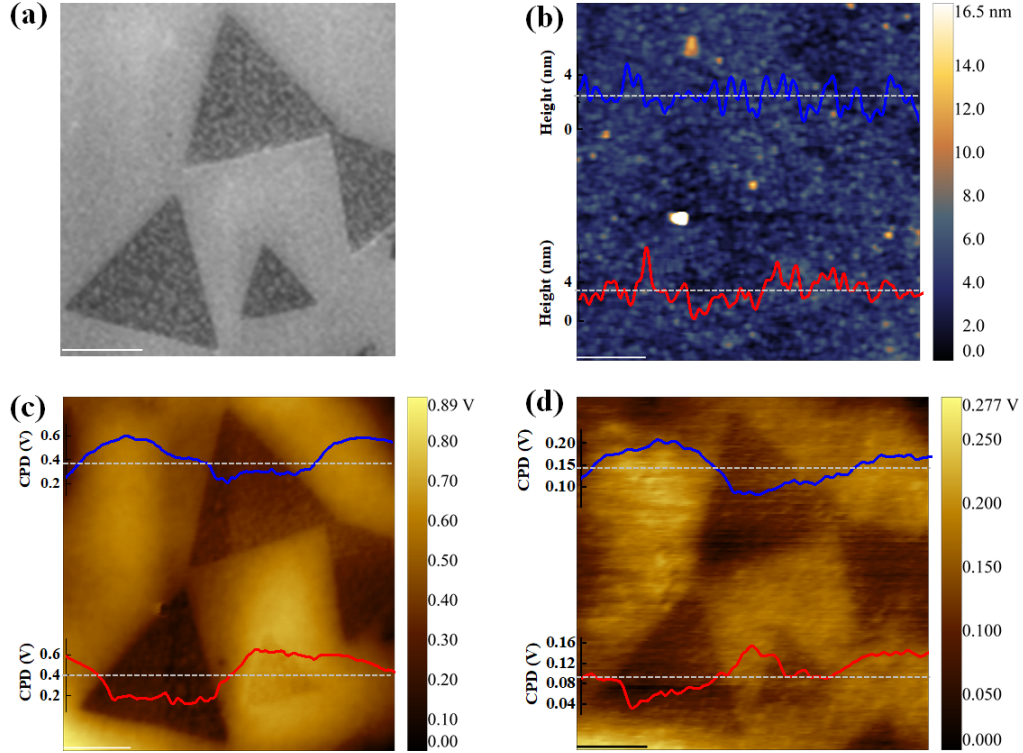


Figure 5.2. (a) SEM of MoS<sub>2</sub> sample. (b) KPFM map of as-prepared sample. (c) KPFM surface potential map with sample after both photodoping (laser illumination) chemically dopant treatments.

Table 5.2. CPD of as-grown and doped MoS<sub>2</sub> flakes

| Number of flakes | $CPD_{as-grown}$ (V) | $CPD_{doped}$ (V) | $\Delta CPD$ (mV) |
|------------------|----------------------|-------------------|-------------------|
| I                | 0.3                  | 0.1               | 200               |
| II               | 0.18                 | 0.08              | 100               |
| III              | 0.61                 | 0.17              | 440               |

The lower the surface potential is, the lower the electron concentration is. According to previous reports, the variation in carrier concentration leads to a corresponding change in PL spectrum [134,135]. The PL spectra are fitted using Lorentzian function to extract the exciton and trion components. For as-grown MoS<sub>2</sub>, the intensity of trion peak is more than the exciton peak which indicates that the sample is n-typed. After chemical and photo doping the height of the exciton peak dominates the trion peaks which indicates the addition of hole to the system leads creating parity between electrons and holes and subsequently reduction of free charge carriers. Photodoping

induces local hole transfer and carrier redistribution in the flake as well. Using equation 5.5, the number of photodoping ( $n_{ph}$ ) is calculated approximately  $3.48 \times 10^{16}$ , when  $P = 13 \text{ mW}$ ,  $t = 0.1 \text{ s}$  and  $\lambda = 532 \text{ nm}$  (green laser). The carrier concentration can be extracted from the photoluminescence and it is in consistency with the KPFM results. The carrier concentration in intrinsic (as-grown) and p-doped  $\text{MoS}_2$  were  $n_{as-grown} = 4.4284 \times 10^{-13} \text{ cm}^{-1}$  and  $n_{doped} = 1.11598 \times 10^{-12} \text{ cm}^{-1}$ , respectively, using mass action model (equation 5.4). The adsorption of p-dopant by 2D  $\text{MoS}_2$  and photodoping resulted in a factor  $\sim 2$  enhancement of the PL signal because of switching between trions and excitons.

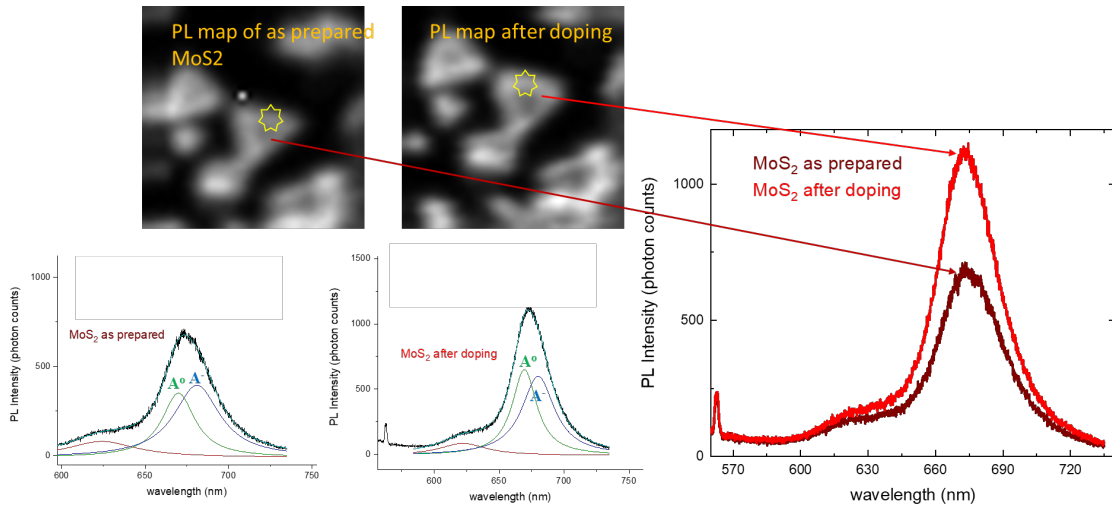


Figure 5.3. (a) Photoluminescence (PL) spectral map of as-prepared sample (b) after photo-chemical doping. (c) PL spectra showing PL intensity before (d) after photo-chemical doping.

### 5.1.4 Conclusions

In conclusion, the adsorption of p-dopant (F4TCNQ molecules) by 2D  $\text{MoS}_2$  and photo doping resulted in PL enhancement by factor  $\sim 2$  due to decrease of excess electron concentration, resulting in an switching between trions and excitons. This study has a promising prospect for enhancement of light emission in optoelectronic systems based on  $\text{MoS}_2$ .

### 5.1.5 Recommendations for Future research

During PL measurements we found out that the Laser thinning and cleaning of 2D material is a promising method to achieve a monolayer MoS<sub>2</sub> and improve its quality.

## 5.2 Task two: Studying 2D vdw interaction with external doping and developing design of nanoscale biosensor.

Recently, two-dimensional materials have been developed as label-free biosensors due to their exceptional specificity and sensitivity for detection of analytes [149–152]. 2D materials could be developed and combined together to make VdW heterostructures. Hence, they can create several signals in response to a single analyte or to respond to a group of substances simultaneously via multiple channels. A multi-mode biosensor could distinguish the analyte from background signals in complex mediums with a single test. This happens just as a result of its higher throughput compared with its counterparts [153–155].

However, intrinsic ultrahigh surface-to-volume ratio in 2D materials impose surface non-uniformities at a nanometer scale. Such non-uniformities include impurities, adsorbates, defects, wrinkles and ruptures that might influence the optical properties of 2D materials. The scale of these non-uniformities poses the challenge to understanding the physical mechanisms that influence the performance of 2D materials and devices. The optical microscopy lacks the required resolution to characterize the structure of 2D materials with high spatial resolution. Also, the electron microscopy normally fails to identify the optical characteristics of the 2D materials. As a result, a combination of multiple characterisation methods and correlation analysis is needed to discover such mechanisms [156].

Here, multidimensional imaging, including Raman and near field microscopies, scanning probe and electron microscopies, was applied to decode the physical mechanism of multimodal detection of doxorubicin (DOX) [157–159], an anthracycline cancer drug, by 2D material vertical heterostructures of graphene/MoS<sub>2</sub>/SiO<sub>2</sub>/Si [71].

- Scattering scanning near-field optical microscopy (s-SNOM)

Scattering scanning near-field optical microscopy (s-SNOM) provides images in nanometer with breaking the diffraction limit (20 nm) where the interaction between the probe and the sample is nontrivial [160]. S-SNOM involves an AFM probe with a sharp AFM tip which elastically scattered light over a sample surface in a raster pattern. In near-field, polarization of incident light at the tip apex effects the elastic scattering of light. The wavelength of scattered light is constant. The scattered and reflected

lights either from near-field or far-field (out of tip-sample distance) are collected by the detector. To distinguish the near-field scattered light from far-field background, the tip oscillates at the mechanical resonance of the AFM cantilever. While the system at the tapping-mode frequency, the detector signal is passed to a lock-in amplifier [161].

### 5.2.1 Materials and Methods

The CVD method was used to grow the monolayer MoS<sub>2</sub> onto the 300 nm SiO<sub>2</sub>/Si substrate as described previously. The monolayer graphene grown on the Cu foil by CVD method was provided by NSF 2DCC-MIP center at PSU. Electrochemical technique was employed to transfer graphene on MoS<sub>2</sub> while graphene was covered by PMMA. After transferring graphene on top of MoS<sub>2</sub>/SiO<sub>2</sub>/Si, acetone was used to remove PMMA residue.

### 5.2.2 Characterization

The initial morphology and topography on samples was imaged in a field emission scanning electron microscope Zeiss Auriga FIB/FESEM. PL and Raman spectra were measured using a Horiba Jobin Yvon LabRAM HR-Evolution Raman system (MCL facility at PSU), 488 nm (for Raman) and 532 nm (for PL) laser excitation wavelengths were used; Horiba XploRA Raman system (JSNN facility at UNCG) was used for taking Raman spectra at 532 nm of excitation. To analyze the PL and Raman characterization, a home-written code was applied. The s-SNOM mapping was carried out by using scattering type scanning near-field optical microscope (custom-built Neaspecsystem) in pseudoheterodyne mode (tapping amplitude 70 nm, ARROW-NCPT probes by Nanoworld <25 nm radius, excitation by CW Quantum Cascade Laser (MIR-Cat by Daylight) at power < 2 mW in focal aperture. The AFM/KPFM measurements were done at MCL/PSU using Dimension Icon AFM in PeakForce Kelvin Probe Force Microscopy in frequency modulated mode (PFKPFM-FM, Bruker Nano Inc., Santa Barbara, CA) utilizing a PFQNE-AL probe (Bruker SPM Probes, Camarillo, CA). The probe's KPFM response was compared to an Au-Si-Al reference before the samples were measured and a freshly cleaved highly oriented pyrolytic graphite (HOPG) with work function value of 4.6 eV was used as a reference.

### 5.2.3 Results and Discussion

2D MoS<sub>2</sub> is well-known for its strong PL signal [144] and it can influence adsorption of molecular species [4, 135, 162, 163]. Fig. 5.4 (c) illustrates a change in PL spectrum of MoS<sub>2</sub> photo-luminescence (PL) after incubation to 172 nM solution of DOX for 15

Table 5.3. The PL fit parameters for Fig. 5.4 (d): upper/lower row corresponds to PL with/without DOX.

| Trion             |               |            | A-exciton          |                |             | B-exciton         |                |             |
|-------------------|---------------|------------|--------------------|----------------|-------------|-------------------|----------------|-------------|
| $\omega c, eV$    | $\gamma, meV$ | P, cts.    | $\omega c, eV$     | $\gamma, meV$  | P, cts.     | $\omega c, eV$    | $\gamma, meV$  | P, cts      |
| $1.739 \pm 0.002$ | $60. \pm 3.$  | $32 \pm 4$ | $1.815 \pm 0.0002$ | $82.0 \pm 0.3$ | $793 \pm 4$ | $1.953 \pm 0.001$ | $135.8 \pm 2.$ | $203 \pm 1$ |
| $1.719 \pm 0.003$ | $60. \pm 9.$  | $15 \pm 3$ | $1.806 \pm 0.002$  | $90.7 \pm 0.3$ | $586 \pm 3$ | $1.955 \pm 0.002$ | $135.0 \pm 2.$ | $197 \pm 2$ |

minutes (the large area integrated PL is presented here; to not be confused with local micro-PL discussed below).

The PL band is fitted with individual excitation lines to assist in understanding the physical mechanisms resulting in DOX recognition: inset of Fig. 5.4 (d) shows the MoS<sub>2</sub> optical transitions include typical B- and A-exciton sub-bands, trion (A<sup>-</sup>) and, often, additional localized modes.

This shows a shift in mode peak position ( $\Delta\omega$ ), peak intensity ( $\Delta P$ ) and width ( $\Delta\gamma$ ) are indicative for analyte absorption and also gave rise to a charge transfer/doping and strain imposed in the 2D material. These shifts are specific for an analyte: panel (d) and data in Table 5.3 provide the values for DOX analyte. While upper B-exciton is barely influenced by the drug molecules (a small intensity difference is detected, see red arrow in panel (d)), both A-exciton and trion show red-shift, lower intensity and larger width, that all together lead to the spectral differences in panel (c). Ability to detect DOX at a low (sub-nM) concentration (and distinguish it from other components of a complex solution would depend on amount of signal over the noise for the biosensor. The variation of the signal in the pristine biosensing material importantly adds to the total uncertainty and reduces the device performance as shown in a discussion below. Since there is no calibrated negative control for unknown analyte, agnostic detection of a chemical or biothreat will require multiplexing the receptor signal with additional channels. To explain the difference between the signal from DOX and any other molecule potentially causing PL modulation, the characteristic fingerprint Raman spectrum of DOX was carefully measured as shown in Fig. 5.4 (b) (cyan curve).

Table 5.4. Measured GERS enhancement factors for major fingerprint Raman lines of DOX.

| Raman line position, cm <sup>-1</sup> | 1236 | 1244 | 1260 | 1268 | 1326 | 1434 | 1613 |
|---------------------------------------|------|------|------|------|------|------|------|
| GERS enhancement factor               | 6.4  | 7.0  | 23.3 | 23.3 | 1.8  | 2.9  | 2.1  |

DOX Raman lines (red arrows) are superimposed, mixed, and obscured with DMSO (background) response (cyan arrows). The line intensity of analyte is also comparable

to the background even at a relatively high DOX concentration. On the contrary, when deposited on graphene surface, most of DOX lines become clearly visible, due to a significant GERS enhancement of the Raman signal of DOX (compare red and cyan curves). Table 5.4 summarizes the amount of signal enhancement for lines. During the interaction between our sample with two substances, the intensity of fingerprint lines of DOX confirms the analyte structure and its presence (better than using PL data channel alone). GERS, the second data channel serves as a complementary channel to the PL detection which also gives the concentration of the drug (while intensity of the GERS signal depends on enhancement factors and cannot be used to measure the amount of analyte). As shown in Fig. 5.4 (b), many of the DOX lines which are superimposed with the Raman spectrum of graphene (gray curve corresponds to monolayer graphene reference), specifically with D- and G-lines around  $1350$  and  $1600$   $cm^{-1}$ .

By obscuring some of the DOX modes, Raman spectra of graphene should be analyzed separately, showing another channel to be multiplexed with the PL and GERS data. Fig 5.4 (e-f) portrays the pronounced red-shift and the width increase for two major lines of graphene, G- and 2D-band when interacting with DOX analyte (red). Panels (g-l) entails the statistical information on modulation of both line position and width for both modes; conversely with previous optical data, each data point corresponds to a small local region on the sample, less than  $0.1 \mu m^2$ , diffraction limited. Hence, it remains clear that the data points aggregate into two separate clusters even though point-to-point variability due to the non-uniformity of the signal is the non-negligible for 2D-mode (compare  $(\Delta\gamma)/(\Delta\omega)$  correlation plot in panel (h) and partial distribution functions in panels (k-l)). The statistical distribution of the data from (g-l) lays out various salient information about the sample.

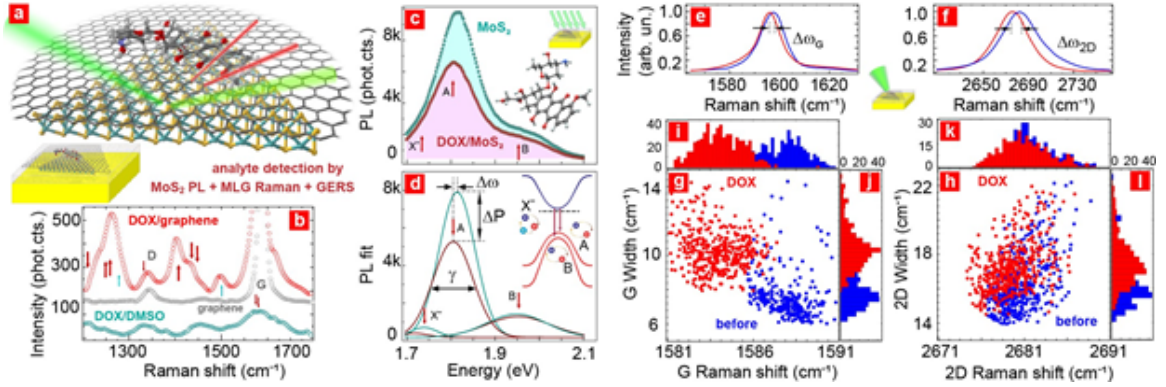


Figure 5.4. Multiplexed detection of doxorubicin drug. (a) Schematics of multimode detection by the combination of MoS<sub>2</sub> photoluminescence, DOX GERS, and Raman shift of monolayer graphene. (b) GERS signal of DOX/monolayer graphene (red), vs. reference Raman spectra of DOX/DMSO solution (cyan) and monolayer graphene (gray); red (cyan) arrows mark DOX (DMSO) lines. (c) Modulation of MoS<sub>2</sub> PL spectrum: with DOX (red) and w/o DOX (cyan); inset shows DOX molecular structure. (d) Fitting of measured PL spectra from (c): A/B-exciton and trion (A<sup>-</sup>) lines are shown; modulation of peak position ( $\Delta\omega$ ) and intensity ( $\Delta P$ ) are indicated using A-exciton fit; inset shows the schematics of optical subbands of MoS<sub>2</sub>. (e-f) Typical Raman spectra of monolayer graphene: with DOX (red) and before incubation (blue); G- and 2D-line intensities were normalized to unity. (g-h) Correlation plots and partial distribution functions for peak position and width for G- and 2D-lines, measured locally, at diffraction limited spots across the sample; same color code as in (e-f); clear line red-shift and broadening are detected with DOX.

Some structural non-uniformities were revealed by studying the electron microscopy of MoS<sub>2</sub>/graphene vertical heterostructure. A few typical images of several randomly selected single layer MoS<sub>2</sub> islands, coated with monolayer graphene, are shown in Fig. 5.5. The charged under e-beam, white nanocrystallites, likely made of insulating molybdenum oxide, are seen either in the center of the island (metal nucleation site) or at the edge (metal precipitation site); in some cases, those grow to microcrystals of Mo<sub>2</sub>O<sub>3</sub> (see Fig 6.2(e)) of characteristic triangular (or rectangular, not shown here) shape and size up to 1/2  $\mu\text{m}$ . Graphene was found to be non-conformal to the substrate, making short wrinkles between nanoscale posts (10-20 nm tall). The surface of MoS<sub>2</sub> islands appears mostly uniform in scanning electron microscopy (SEM) image, however the optical properties of 2DM demonstrate substantial variation, in substantial agreement with PL statistics from Fig. 5.4. The variability of PL in pristine material could produce uncertainty in detection of the analyte. Scattering scanning near-field optical microscopy (sSNOM) has also been applied so as to find

an origin for the variation. By carefully aligning the large area scans of the same heterostructure assists with the correlation of different characterization methods (including SEM, scanning probe imaging, as well as PL and Raman microscopy, having a lower resolution though). Fig. 6.2 (b-d) shows the sSNOM image (2nd harmonic optical amplitude, see Methods for details) reveals variation of surface impedance of monolayer graphene/MoS<sub>2</sub> heterostructure at the sub-micrometer scale, not captured by SEM (or AFM). We propose that a series of bright regions (on the darker background of MoS<sub>2</sub>) correspond to the local defects of the TMDC material. We regularly observe such a contrast at the edge of the island which is known to be prone to partial oxidation.

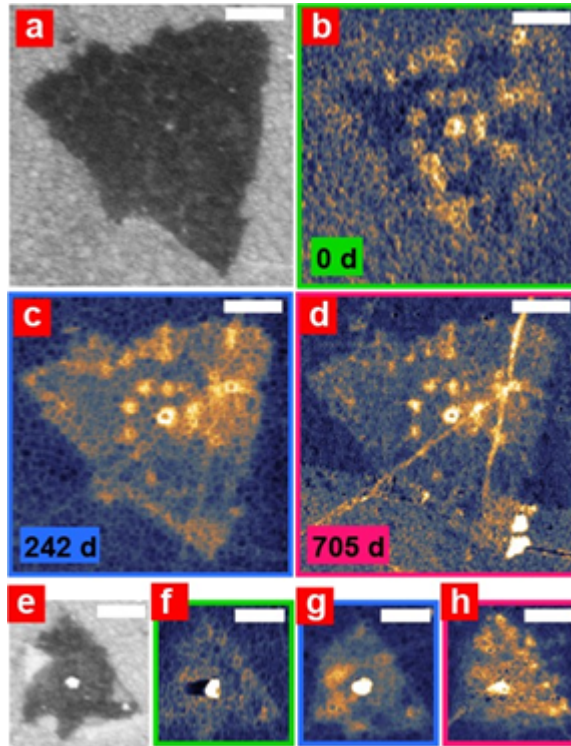


Figure 5.5. Stability test of MoS<sub>2</sub>/graphene vertical heterostructure. SEM (a,e) and sSNOM (b-d,f-h) images of two MoS<sub>2</sub> islands, randomly selected, coated with monolayer graphene. The island (a) shows nearly zero degradation after 242 days in ambient – from (b) to (c), neither after 705 days – from (b) to (d); the island (e) was selected near a tear in monolayer graphene and shows (g) partial oxidation near the central micro-crystallite of molybdenum after 242 days, followed by (h) almost complete oxidation of MoS<sub>2</sub> surface after 705 days. All scale bars are 1  $\mu\text{m}$ .

A multidimensional imaging combining sSNOM and Kelvin probe force microscopy (KPFM) was developed and then compared with PL (and Raman) microscopy. Fig.

5.6 (a-b) shows two maps of the same island where KPFM (work function) channel and sSNOM (optical surface impedance) channel were employed, they were found to be identical. Panel (c) is also a cross section profile which quantifies the variation of the Fermi level of graphene above the MoS<sub>2</sub> layer.

In both graphene and MoS<sub>2</sub>, carrier density decreases as a result of the charge transfer in the vertical heterojunction, thereby decreasing the magnitude of graphene work function and doping level. The KPFM probe is in contact with the outermost layer of the heterostructure, graphene, thus it measures the work function of monolayer graphene. Graphene appears negatively doped by MoS<sub>2</sub> when above the island. The monolayer graphene Fermi level, taken with respect to graphene Dirac point, is negative, corresponding to p-doping.

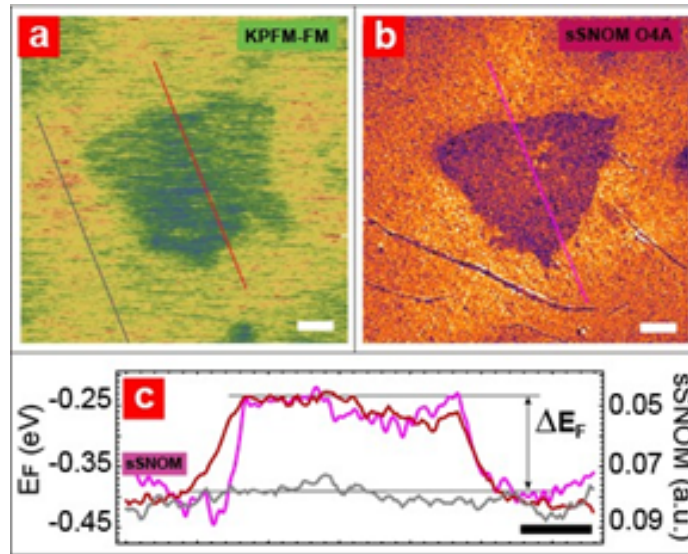


Figure 5.6. Correlation of monolayer graphene work function data with sSNOM optical surface impedance. Aligned maps for (a) KPFM and (b) sSNOM (4th harmonic) amplitude. (c) Cross section profiles across the MoS<sub>2</sub> area (KPFM, red and sSNOM, pink) vs. monolayer graphene reference (KPFM, gray), taken along the lines of the same color in (a-b).

## 5.2.4 Conclusions

In conclusion, multidimensional characterization data above showed existence of non-uniformities in 2D materials at the nanoscale and allowed to identify doping and/or strain variations as the origin of statistical distribution of the optical signals used in all three recognition mechanisms (PL shift, Raman spectroscopy and GERS). When integrated over the device area, such a variability in local response would

translate in a broadening of the biosensing spectral signal, thus, raising device-to-device variability and, ultimately, lowering the sensitivity and the limit-of-detection by increasing background and/or systematic error. While the variability of individual device response often could be addressed by careful calibration against known analytes, such a fluctuation and spread of the integrated response would affect biosensing accuracy and, certainly, reduce ability to precise biosensing in the agnostic detection mode

### **5.2.5 Recommendations for Future research**

Presented study suggests that, in order to improve performance of biosensors based on 2D heterostructures, non-uniformity of doping and strain – two major mechanisms for optical signal variation – must be addressed. Currently, most of 2D heterostructures are fabricated by transfer methods, that are known to produce both strain and doping (especially for wet transfer). New methods of strain-free and doping-free transfer need to be developed. Alternatively, such heterostructure materials should be fabricated in-situ, in synthetic facility, to preserve the layer-epitaxy and exclude contamination between the layers.

# References

- [1] H. A. H. Eid, S. Kovalev, K.-J. Tielrooij, M. Bonn, M. Gensch, and D. Turchinovich, "Terahertz nonlinear optics of graphene: From saturable absorption to high-harmonics generation," *Advanced optical materials*, vol. 8, no. 3, 2020.
- [2] C. Mas-Balleste, "Gomez-navarro, j. gomez-herrero, f. zamora," *Nanoscale*, vol. 3, p. 20, 2011.
- [3] L. Liang and V. Meunier, "First-principles raman spectra of mos 2, ws 2 and their heterostructures," *Nanoscale*, vol. 6, no. 10, pp. 5394–5401, 2014.
- [4] F. Aryeetey, S. Pourianejad, O. Ayanbajo, K. Nowlin, T. Ignatova, and S. Aravamudhan, "Bandgap recovery of monolayer mos 2 using defect engineering and chemical doping," *RSC Advances*, vol. 11, no. 34, pp. 20893–20898, 2021.
- [5] T. Kim, S. Fan, S. Lee, M.-K. Joo, and Y. H. Lee, "High-mobility junction field-effect transistor via graphene/mos 2 heterointerface," *Scientific reports*, vol. 10, no. 1, pp. 1–8, 2020.
- [6] Y. Zhou, W. Xu, Y. Sheng, H. Huang, Q. Zhang, L. Hou, V. Shautsova, and J. H. Warner, "Symmetry-controlled reversible photovoltaic current flow in ultrathin all 2d vertically stacked graphene/mos2/ws2/graphene devices," *ACS applied materials & interfaces*, vol. 11, no. 2, pp. 2234–2242, 2019.
- [7] A. Di Bartolomeo, "Emerging 2d materials and their van der waals heterostructures," 2020.
- [8] F. Giannazzo, S. Lara Avila, J. Eriksson, and S. Sonde, *Integration of 2D Materials for Electronics Applications*. MDPI, 2019.
- [9] L. H. Madkour, *Nanoelectronic Materials: Fundamentals and Applications*, vol. 116. Springer, 2019.

- [10] L. Wang, S. Zihlmann, M.-H. Liu, P. Makk, K. Watanabe, T. Taniguchi, A. Baumgartner, and C. Schonberger, “New generation of moiré superlattices in doubly aligned hbn/graphene/hbn heterostructures,” *Nano letters*, vol. 19, no. 4, pp. 2371–2376, 2019.
- [11] A. Abbas, L. Tian, J. J. Morrissey, E. D. Kharasch, and S. Singamaneni, “Hot spot-localized artificial antibodies for label-free plasmonic biosensing,” *Advanced functional materials*, vol. 23, no. 14, pp. 1789–1797, 2013.
- [12] L. Guo, J. A. Jackman, H.-H. Yang, P. Chen, N.-J. Cho, and D.-H. Kim, “Strategies for enhancing the sensitivity of plasmonic nanosensors,” *Nano Today*, vol. 10, no. 2, pp. 213–239, 2015.
- [13] Y. Feng, Y. Liu, and J. Teng, “Design of an ultrasensitive spr biosensor based on a graphene-mos 2 hybrid structure with a mgf 2 prism,” *Applied optics*, vol. 57, no. 14, pp. 3639–3644, 2018.
- [14] G. Zheng, X. Zou, Y. Chen, L. Xu, and W. Rao, “Fano resonance in graphene-mos2 heterostructure-based surface plasmon resonance biosensor and its potential applications,” *Optical Materials*, vol. 66, pp. 171–178, 2017.
- [15] M. Focsan, A. Campu, A.-M. Craciun, M. Potara, C. Leordean, D. Maniu, and S. Astilean, “A simple and efficient design to improve the detection of biotin-streptavidin interaction with plasmonic nanobiosensors,” *Biosensors and Bioelectronics*, vol. 86, pp. 728–735, 2016.
- [16] K. Novoselov, “Nobel lecture: Graphene: Materials in the flatland,” *Reviews of modern physics*, vol. 83, no. 3, p. 837, 2011.
- [17] K. S. Novoselov, “Graphene: materials in the flatland (nobel lecture),” *Angewandte Chemie International Edition*, vol. 50, no. 31, pp. 6986–7002, 2011.
- [18] A. C. Neto, F. Guinea, N. M. Peres, K. S. Novoselov, and A. K. Geim, “The electronic properties of graphene,” *Reviews of modern physics*, vol. 81, no. 1, p. 109, 2009.
- [19] F. Xia, H. Yan, and P. Avouris, “The interaction of light and graphene: basics, devices, and applications,” *Proceedings of the IEEE*, vol. 101, no. 7, pp. 1717–1731, 2013.
- [20] J. T. Robinson, J. Culbertson, M. Berg, and T. Ohta, “Work function variations in twisted graphene layers,” *Scientific reports*, vol. 8, no. 1, pp. 1–9, 2018.

- [21] X. Li, W. Cai, J. An, S. Kim, J. Nah, D. Yang, R. Piner, A. Velamakanni, I. Jung, E. Tutuc, *et al.*, “Large-area synthesis of high-quality and uniform graphene films on copper foils,” *science*, vol. 324, no. 5932, pp. 1312–1314, 2009.
- [22] N. Mishra, J. Boeckl, N. Motta, and F. Iacopi, “Graphene growth on silicon carbide: A review,” *physica status solidi (a)*, vol. 213, no. 9, pp. 2277–2289, 2016.
- [23] S. Gorantla, A. Bachmatiuk, J. Hwang, H. A. Alsalman, J. Y. Kwak, T. Seyller, J. Eckert, M. G. Spencer, and M. H. Rümmeli, “A universal transfer route for graphene,” *Nanoscale*, vol. 6, no. 2, pp. 889–896, 2014.
- [24] H. C. Lee, W.-W. Liu, S.-P. Chai, A. R. Mohamed, A. Aziz, C.-S. Khe, N. M. Hidayah, and U. Hashim, “Review of the synthesis, transfer, characterization and growth mechanisms of single and multilayer graphene,” *RSC advances*, vol. 7, no. 26, pp. 15644–15693, 2017.
- [25] M. Chen, R. C. Haddon, R. Yan, and E. Bekyarova, “Advances in transferring chemical vapour deposition graphene: a review,” *Materials Horizons*, vol. 4, no. 6, pp. 1054–1063, 2017.
- [26] J. D. Wood, G. P. Doidge, E. A. Carrion, J. C. Koepke, J. A. Kaitz, I. Datye, A. Behnam, J. Hewaparakrama, B. Aruin, Y. Chen, *et al.*, “Annealing free, clean graphene transfer using alternative polymer scaffolds,” *Nanotechnology*, vol. 26, no. 5, p. 055302, 2015.
- [27] R. Mas-Balleste, C. Gomez-Navarro, J. Gomez-Herrero, and F. Zamora, “2d materials: to graphene and beyond,” *Nanoscale*, vol. 3, no. 1, pp. 20–30, 2011.
- [28] K. Dileep, R. Sahu, S. Sarkar, S. C. Peter, and R. Datta, “Layer specific optical band gap measurement at nanoscale in mos2 and res2 van der waals compounds by high resolution electron energy loss spectroscopy,” *Journal of Applied Physics*, vol. 119, no. 11, p. 114309, 2016.
- [29] Y. Li, Z. Qi, M. Liu, Y. Wang, X. Cheng, G. Zhang, and L. Sheng, “Photoluminescence of monolayer mos 2 on laalo 3 and srtio 3 substrates,” *Nanoscale*, vol. 6, no. 24, pp. 15248–15254, 2014.
- [30] J. Sun, X. Li, W. Guo, M. Zhao, X. Fan, Y. Dong, C. Xu, J. Deng, and Y. Fu, “Synthesis methods of two-dimensional mos2: A brief review,” *Crystals*, vol. 7, no. 7, p. 198, 2017.
- [31] J. Yue, J. Jian, P. Dong, L. Luo, and F. Chang, “Growth of single-layer mos2 by chemical vapor deposition on sapphire substrate,” in *IOP Conference Series: Materials Science and Engineering*, vol. 592, p. 012044, IOP Publishing, 2019.

- [32] K. Kośmider and J. Fernández-Rossier, “Electronic properties of the mos 2-ws 2 heterojunction,” *Physical Review B*, vol. 87, no. 7, p. 075451, 2013.
- [33] Y. Jia, X. Gong, P. Peng, Z. Wang, Z. Tian, L. Ren, Y. Fu, and H. Zhang, “Toward high carrier mobility and low contact resistance: laser cleaning of pmma residues on graphene surfaces,” *Nano-micro letters*, vol. 8, no. 4, pp. 336–346, 2016.
- [34] J. Kang, D. Shin, S. Bae, and B. H. Hong, “Graphene transfer: key for applications,” *Nanoscale*, vol. 4, no. 18, pp. 5527–5537, 2012.
- [35] A. Ambrosi and M. Pumera, “The cvd graphene transfer procedure introduces metallic impurities which alter the graphene electrochemical properties,” *Nanoscale*, vol. 6, no. 1, pp. 472–476, 2014.
- [36] S. D. Sarma, “Shafhque adam,” *EH Hwang, and Enrico Rossi. Electronic transport in two-dimensional graphene. Rev. Mod. Phys*, vol. 83, no. 2, p. 407, 2011.
- [37] X. Deng and W. Jiang, “Evaluating green supply chain management practices under fuzzy environment: a novel method based on d number theory,” *International Journal of Fuzzy Systems*, vol. 21, no. 5, pp. 1389–1402, 2019.
- [38] W. Choi, Y.-S. Seo, J.-Y. Park, K. Kim, J. Jung, N. Lee, Y. Seo, and S. Hong, “Effect of annealing in ar/h 2 environment on chemical vapor deposition-grown graphene transferred with poly (methyl methacrylate),” *IEEE Transactions on Nanotechnology*, vol. 14, no. 1, pp. 70–74, 2014.
- [39] W. S. Leong, C. T. Nai, and J. T. Thong, “What does annealing do to metal-graphene contacts?,” *Nano letters*, vol. 14, no. 7, pp. 3840–3847, 2014.
- [40] Y.-D. Lim, D.-Y. Lee, T.-Z. Shen, C.-H. Ra, J.-Y. Choi, and W. J. Yoo, “Si-compatible cleaning process for graphene using low-density inductively coupled plasma,” *ACS nano*, vol. 6, no. 5, pp. 4410–4417, 2012.
- [41] H. Sun, D. Chen, Y. Wu, Q. Yuan, L. Guo, D. Dai, Y. Xu, P. Zhao, N. Jiang, and C.-T. Lin, “High quality graphene films with a clean surface prepared by an uv/ozone assisted transfer process,” *Journal of Materials Chemistry C*, vol. 5, no. 8, pp. 1880–1884, 2017.
- [42] B. Son, H. Kim, H. Jeong, J.-Y. Park, S. Lee, and Y. H. Ahn, “Electron beam induced removal of pmma layer used for graphene transfer,” *Scientific reports*, vol. 7, no. 1, pp. 1–7, 2017.

- [43] Y. Ahn, H. Kim, Y.-H. Kim, Y. Yi, and S.-I. Kim, "Procedure of removing polymer residues and its influences on electronic and structural characteristics of graphene," *Applied Physics Letters*, vol. 102, no. 9, p. 091602, 2013.
- [44] Z. Cheng, Q. Zhou, C. Wang, Q. Li, C. Wang, and Y. Fang, "Toward intrinsic graphene surfaces: a systematic study on thermal annealing and wet-chemical treatment of sio<sub>2</sub>-supported graphene devices," *Nano letters*, vol. 11, no. 2, pp. 767–771, 2011.
- [45] H. Van Ngoc, Y. Qian, S. K. Han, and D. J. Kang, "Pmma-etching-free transfer of wafer-scale chemical vapor deposition two-dimensional atomic crystal by a water soluble polyvinyl alcohol polymer method," *Scientific reports*, vol. 6, no. 1, pp. 1–9, 2016.
- [46] B. Marta, C. Leordean, T. Istvan, I. Botiz, and S. Astilean, "Efficient etching-free transfer of high quality, large-area cvd grown graphene onto polyvinyl alcohol films," *Applied Surface Science*, vol. 363, pp. 613–618, 2016.
- [47] S. Chen, Y. Wei, S. Wei, Y. Lin, and L. Liu, "Ultrasensitive cracking-assisted strain sensors based on silver nanowires/graphene hybrid particles," *ACS applied materials & interfaces*, vol. 8, no. 38, pp. 25563–25570, 2016.
- [48] B. William, "The original of the soxhlet extractor," *Chemical education*, vol. 84, pp. 1913–1915, 2007.
- [49] W. S. Leong, H. Wang, J. Yeo, F. J. Martin-Martinez, A. Zubair, P.-C. Shen, Y. Mao, T. Palacios, M. J. Buehler, J.-Y. Hong, *et al.*, "Paraffin-enabled graphene transfer," *Nature communications*, vol. 10, no. 1, pp. 1–8, 2019.
- [50] A. K. Geim and I. V. Grigorieva, "Van der waals heterostructures," *Nature*, vol. 499, no. 7459, pp. 419–425, 2013.
- [51] L. Xu, W.-Q. Huang, W. Hu, B.-X. Zhou, A. Pan, and G.-F. Huang, "2d mos<sub>2</sub>-graphene-based multilayer van der waals heterostructures: Enhanced charge transfer and optical absorption, and electric-field tunable dirac point and band gap," *arXiv preprint arXiv:1611.02510*, 2016.
- [52] B. Qiu, X. Zhao, G. Hu, W. Yue, J. Ren, and X. Yuan, "Optical properties of graphene/mos<sub>2</sub> heterostructure: first principles calculations," *Nanomaterials*, vol. 8, no. 11, p. 962, 2018.
- [53] J.-W. Choi, J. Yoon, J. Lim, M. Shin, and S.-N. Lee, "Graphene/mos<sub>2</sub> nanohybrid for biosensors," *Materials*, vol. 14, no. 3, p. 518, 2021.

- [54] H. C. Diaz, R. Addou, and M. Batzill, “Interface properties of cvd grown graphene transferred onto mos 2 (0001),” *Nanoscale*, vol. 6, no. 2, pp. 1071–1078, 2014.
- [55] D. Pierucci, H. Henck, C. H. Naylor, H. Sediri, E. Lhuillier, A. Balan, J. E. Rault, Y. J. Dappe, F. Bertran, P. Le Fèvre, *et al.*, “Large area molybdenum disulphide-epitaxial graphene vertical van der waals heterostructures,” *Scientific reports*, vol. 6, p. 26656, 2016.
- [56] R. Rao, A. E. Islam, S. Singh, R. Berry, R. K. Kawakami, B. Maruyama, and J. Katoch, “Spectroscopic evaluation of charge-transfer doping and strain in graphene/mos 2 heterostructures,” *Physical Review B*, vol. 99, no. 19, p. 195401, 2019.
- [57] X. Sun, B. Zhang, Y. Li, X. Luo, G. Li, Y. Chen, C. Zhang, and J. He, “Tunable ultrafast nonlinear optical properties of graphene/mos2 van der waals heterostructures and their application in solid-state bulk lasers,” *ACS nano*, vol. 12, no. 11, pp. 11376–11385, 2018.
- [58] C.-H. Chen, C.-T. Lin, Y.-H. Lee, K.-K. Liu, C.-Y. Su, W. Zhang, and L.-J. Li, “Electrical probing of submicroliter liquid using graphene strip transistors built on a nanopipette,” *Small*, vol. 8, no. 1, pp. 43–46, 2012.
- [59] C.-H. Chen, C.-T. Lin, W.-L. Hsu, Y.-C. Chang, S.-R. Yeh, L.-J. Li, and D.-J. Yao, “A flexible hydrophilic-modified graphene microprobe for neural and cardiac recording,” *Nanomedicine: Nanotechnology, Biology and Medicine*, vol. 9, no. 5, pp. 600–604, 2013.
- [60] F. Schwierz, “Graphene transistors,” *Nature nanotechnology*, vol. 5, no. 7, pp. 487–496, 2010.
- [61] H. Liu, A. T. Neal, and P. D. Ye, “Channel length scaling of mos2 mosfets,” *ACS nano*, vol. 6, no. 10, pp. 8563–8569, 2012.
- [62] Y. Dong, T. Zhang, X. Lin, J. Feng, F. Luo, H. Gao, Y. Wu, R. Deng, and Q. He, “Graphene/aptamer probes for small molecule detection: from in vitro test to in situ imaging,” *Microchimica Acta*, vol. 187, no. 3, pp. 1–18, 2020.
- [63] L. Tang, Y. Wang, and J. Li, “The graphene/nucleic acid nanobiointerface,” *Chemical Society Reviews*, vol. 44, no. 19, pp. 6954–6980, 2015.
- [64] O. O. Ayodele, A. O. Adesina, S. Pourianejad, J. Averitt, and T. Ignatova, “Recent advances in nanomaterial-based aptasensors in medical diagnosis and therapy,” *Nanomaterials*, vol. 11, no. 4, p. 932, 2021.

- [65] J. Ji, Y. Pang, D. Li, Z. Huang, Z. Zhang, N. Xue, Y. Xu, and X. Mu, "An aptamer-based shear horizontal surface acoustic wave biosensor with a cvd-grown single-layered graphene film for high-sensitivity detection of a label-free endotoxin," *Microsystems & Nanoengineering*, vol. 6, no. 1, pp. 1–11, 2020.
- [66] J. Ge, E.-C. Ou, R.-Q. Yu, and X. Chu, "A novel aptameric nanobiosensor based on the self-assembled dna-mos 2 nanosheet architecture for biomolecule detection," *Journal of Materials Chemistry B*, vol. 2, no. 6, pp. 625–628, 2014.
- [67] C. Zhu, Z. Zeng, H. Li, F. Li, C. Fan, and H. Zhang, "Single-layer mos2-based nanoprobe for homogeneous detection of biomolecules," *Journal of the American Chemical Society*, vol. 135, no. 16, pp. 5998–6001, 2013.
- [68] R.-M. Kong, L. Ding, Z. Wang, J. You, and F. Qu, "A novel aptamer-functionalized mos 2 nanosheet fluorescent biosensor for sensitive detection of prostate specific antigen," *Analytical and bioanalytical chemistry*, vol. 407, no. 2, pp. 369–377, 2015.
- [69] C. T. Lim, "Enhancing the sensing specificity of a mos2 nanosheet-based fret aptasensor," 2017.
- [70] X. Liu, Y. Tang, P. Liu, L. Yang, L. Li, Q. Zhang, Y. Zhou, and M. Z. H. Khan, "A highly sensitive electrochemical aptasensor for detection of microcystin-lr based on a dual signal amplification strategy," *Analyst*, vol. 144, no. 5, pp. 1671–1678, 2019.
- [71] T. Ignatova, S. Pourianejad, X. Li, K. Schmidt, F. Aryeetey, S. Aravamudhan, and S. V. Rotkin, "Multidimensional imaging reveals mechanisms controlling label-free biosensing in vertical 2dm-heterostructures," 2021.
- [72] W. I. Lee, I. Y. Sohn, B. Y. Kim, Y. M. Son, J. H. Shin, H. M. Kim, Y. J. Suh, and N.-E. Lee, "A simple and clean transfer method of chemical-vapor deposited graphene on cu," *Science of Advanced Materials*, vol. 7, no. 8, pp. 1540–1545, 2015.
- [73] X.-D. Chen, Z.-B. Liu, C.-Y. Zheng, F. Xing, X.-Q. Yan, Y. Chen, and J.-G. Tian, "High-quality and efficient transfer of large-area graphene films onto different substrates," *Carbon*, vol. 56, pp. 271–278, 2013.
- [74] A. Eckmann, A. Felten, A. Mishchenko, L. Britnell, R. Krupke, K. S. Novoselov, and C. Casiraghi, "Probing the nature of defects in graphene by raman spectroscopy," *Nano letters*, vol. 12, no. 8, pp. 3925–3930, 2012.

- [75] T. Lee, F. A. Mas'ud, M. J. Kim, and H. Rho, "Spatially resolved raman spectroscopy of defects, strains, and strain fluctuations in domain structures of monolayer graphene," *Scientific reports*, vol. 7, no. 1, pp. 1–8, 2017.
- [76] A. C. Ferrari, J. C. Meyer, V. Scardaci, C. Casiraghi, M. Lazzeri, F. Mauri, S. Piscanec, D. Jiang, K. S. Novoselov, S. Roth, *et al.*, "Raman spectrum of graphene and graphene layers," *Physical review letters*, vol. 97, no. 18, p. 187401, 2006.
- [77] W. B. Jensen, "The origin of the soxhlet extractor," *Journal of chemical education*, vol. 84, no. 12, p. 1913, 2007.
- [78] D. Naviglio, P. Scarano, M. Ciaravolo, and M. Gallo, "Rapid solid-liquid dynamic extraction (rslde): A powerful and greener alternative to the latest solid-liquid extraction techniques," *Foods*, vol. 8, no. 7, p. 245, 2019.
- [79] H. Park, P. R. Brown, V. Bulovic, and J. Kong, "Graphene as transparent conducting electrodes in organic photovoltaics: studies in graphene morphology, hole transporting layers, and counter electrodes," *Nano letters*, vol. 12, no. 1, pp. 133–140, 2012.
- [80] W. Choi, M. A. Shehzad, S. Park, and Y. Seo, "Influence of removing pmma residues on surface of cvd graphene using a contact-mode atomic force microscope," *RSC advances*, vol. 7, no. 12, pp. 6943–6949, 2017.
- [81] K. Shahzad, K. Jia, C. Zhao, X. Yan, Z. Yadong, M. Usman, and J. Luo, "An improved rosin transfer process for the reduction of residue particles for graphene," *Nanoscale research letters*, vol. 15, no. 1, pp. 1–11, 2020.
- [82] Z. Zhang, J. Du, D. Zhang, H. Sun, L. Yin, L. Ma, J. Chen, D. Ma, H.-M. Cheng, and W. Ren, "Rosin-enabled ultraclean and damage-free transfer of graphene for large-area flexible organic light-emitting diodes," *Nature communications*, vol. 8, no. 1, pp. 1–9, 2017.
- [83] T. Nasir, B. J. Kim, M. Hassnain, S. H. Lee, B. J. Jeong, I. J. Choi, Y. Kim, H. K. Yu, and J.-Y. Choi, "Plasticized polystyrene by addition of diene based molecules for defect-less cvd graphene transfer," *Polymers*, vol. 12, no. 8, p. 1839, 2020.
- [84] H.-T. Chin, J.-J. Lee, M. Hofmann, and Y.-P. Hsieh, "Impact of growth rate on graphene lattice-defect formation within a single crystalline domain," *Scientific reports*, vol. 8, no. 1, pp. 1–6, 2018.

- [85] N. Bendiab, J. Renard, C. Schwarz, A. Reserbat-Plantey, L. Djevahirdjian, V. Bouchiat, J. Coraux, and L. Marty, “Unravelling external perturbation effects on the optical phonon response of graphene,” *Journal of Raman Spectroscopy*, vol. 49, no. 1, pp. 130–145, 2018.
- [86] N. S. Mueller, S. Heeg, M. P. Alvarez, P. Kusch, S. Wasserroth, N. Clark, F. Schedin, J. Parthenios, K. Papagelis, C. Galiotis, *et al.*, “Evaluating arbitrary strain configurations and doping in graphene with raman spectroscopy,” *2D Materials*, vol. 5, no. 1, p. 015016, 2017.
- [87] K. S. Kim, Y. Zhao, H. Jang, S. Y. Lee, J. M. Kim, K. S. Kim, J.-H. Ahn, P. Kim, J.-Y. Choi, and B. H. Hong, “Large-scale pattern growth of graphene films for stretchable transparent electrodes,” *nature*, vol. 457, no. 7230, pp. 706–710, 2009.
- [88] I. Calizo, A. Balandin, W. Bao, F. Miao, and C. Lau, “Temperature dependence of the raman spectra of graphene and graphene multilayers,” *Nano letters*, vol. 7, no. 9, pp. 2645–2649, 2007.
- [89] L. Liu, S. Ryu, M. R. Tomasik, E. Stolyarova, N. Jung, M. S. Hybertsen, M. L. Steigerwald, L. E. Brus, and G. W. Flynn, “Graphene oxidation: thickness-dependent etching and strong chemical doping,” *Nano letters*, vol. 8, no. 7, pp. 1965–1970, 2008.
- [90] Y.-C. Lin, C.-C. Lu, C.-H. Yeh, C. Jin, K. Suenaga, and P.-W. Chiu, “Graphene annealing: how clean can it be?,” *Nano letters*, vol. 12, no. 1, pp. 414–419, 2012.
- [91] J. H. Choi, J. Lee, M. Byeon, T. E. Hong, H. Park, and C. Y. Lee, “Graphene-based gas sensors with high sensitivity and minimal sensor-to-sensor variation,” *ACS Applied Nano Materials*, vol. 3, no. 3, pp. 2257–2265, 2020.
- [92] A. E. Islam, D. N. Zakharov, J. Carpena-Nuñez, M.-S. Hsiao, L. F. Drummy, E. A. Stach, and B. Maruyama, “Atomic level cleaning of poly-methyl-methacrylate residues from the graphene surface using radiolized water at high temperatures,” *Applied Physics Letters*, vol. 111, no. 10, p. 103101, 2017.
- [93] S. Kim, S. Shin, T. Kim, H. Du, M. Song, C. Lee, K. Kim, S. Cho, D. H. Seo, and S. Seo, “Robust graphene wet transfer process through low molecular weight polymethylmethacrylate,” *Carbon*, vol. 98, pp. 352–357, 2016.
- [94] K. L. Johnson, K. Kendall, and a. Roberts, “Surface energy and the contact of elastic solids,” *Proceedings of the royal society of London. A. mathematical and physical sciences*, vol. 324, no. 1558, pp. 301–313, 1971.

- [95] T. Young, “Iii. an essay on the cohesion of fluids,” *Philosophical transactions of the royal society of London*, no. 95, pp. 65–87, 1805.
- [96] R. J. Good and L. Girifalco, “A theory for estimation of surface and interfacial energies. iii. estimation of surface energies of solids from contact angle data,” *The Journal of Physical Chemistry*, vol. 64, no. 5, pp. 561–565, 1960.
- [97] F. M. Fowkes, “Attractive forces at interfaces,” *Industrial & Engineering Chemistry*, vol. 56, no. 12, pp. 40–52, 1964.
- [98] H. C. Hamaker, “The london—van der waals attraction between spherical particles,” *physica*, vol. 4, no. 10, pp. 1058–1072, 1937.
- [99] J. Visser, “The concept of negative hamaker coefficients. 1. history and present status,” *Advances in Colloid and Interface Science*, vol. 15, no. 2, pp. 157–169, 1981.
- [100] D. K. Owens and R. Wendt, “Estimation of the surface free energy of polymers,” *Journal of applied polymer science*, vol. 13, no. 8, pp. 1741–1747, 1969.
- [101] Z. Li, Y. Wang, A. Kozbial, G. Shenoy, F. Zhou, R. McGinley, P. Ireland, B. Morganstein, A. Kunkel, S. P. Surwade, *et al.*, “Effect of airborne contaminants on the wettability of supported graphene and graphite,” *Nature materials*, vol. 12, no. 10, pp. 925–931, 2013.
- [102] S. Sugden, “Cxlīi.—a relation between surface tension, density, and chemical composition,” *Journal of the Chemical Society, Transactions*, vol. 125, pp. 1177–1189, 1924.
- [103] O. O. Ayodele, F. A. Dawodu, D. Yan, X. Lu, J. Xin, and S. Zhang, “Hydrodeoxygenation of angelica lactone dimers and trimers over silica-alumina supported nickel catalyst,” *Renewable energy*, vol. 86, pp. 943–948, 2016.
- [104] M. J. Frisch, G. W. Trucks, H. B. Schlegel, G. E. Scuseria, M. A. Robb, J. R. Cheeseman, G. Scalmani, V. Barone, G. A. Petersson, H. Nakatsuji, X. Li, M. Caricato, A. V. Marenich, J. Bloino, B. G. Janesko, R. Gomperts, B. Mennucci, H. P. Hratchian, J. V. Ortiz, A. F. Izmaylov, J. L. Sonnenberg, D. Williams-Young, F. Ding, F. Lipparini, F. Egidi, J. Goings, B. Peng, A. Petrone, T. Henderson, D. Ranasinghe, V. G. Zakrzewski, J. Gao, N. Rega, G. Zheng, W. Liang, M. Hada, M. Ehara, K. Toyota, R. Fukuda, J. Hasegawa, M. Ishida, T. Nakajima, Y. Honda, O. Kitao, H. Nakai, T. Vreven, K. Throssell, J. A. Montgomery, Jr., J. E. Peralta, F. Ogliaro, M. J. Bearpark, J. J. Heyd, E. N. Brothers, K. N. Kudin, V. N. Staroverov, T. A. Keith, R. Kobayashi, J. Normand, K. Raghavachari, A. P. Rendell, J. C. Burant, S. S. Iyengar, J. Tomasi,

- M. Cossi, J. M. Millam, M. Klene, C. Adamo, R. Cammi, J. W. Ochterski, R. L. Martin, K. Morokuma, O. Farkas, J. B. Foresman, and D. J. Fox, "Gaussian~16 Revision C.01," 2016. Gaussian Inc. Wallingford CT.
- [105] J. E. Lee, G. Ahn, J. Shim, Y. S. Lee, and S. Ryu, "Optical separation of mechanical strain from charge doping in graphene," *Nature communications*, vol. 3, no. 1, pp. 1–8, 2012.
- [106] J. Rafiee, X. Mi, H. Gullapalli, A. V. Thomas, F. Yavari, Y. Shi, P. M. Ajayan, and N. A. Koratkar, "Wetting transparency of graphene," *Nature materials*, vol. 11, no. 3, pp. 217–222, 2012.
- [107] S. Ebnesajjad, "Material surface preparation techniques," in *Handbook of Adhesives and Surface Preparation*, pp. 49–81, Elsevier, 2011.
- [108] P. Guo, D. Liu, Z. Liu, X. Shang, Q. Liu, and D. He, "Dual functional mos2/graphene interlayer as an efficient polysulfide barrier for advanced lithium-sulfur batteries," *Electrochimica Acta*, vol. 256, pp. 28–36, 2017.
- [109] D. Zhang, Y. Wu, T. Li, Y. Huang, A. Zhang, and M. Miao, "High performance carbon nanotube yarn supercapacitors with a surface-oxidized copper current collector," *ACS applied materials & interfaces*, vol. 7, no. 46, pp. 25835–25842, 2015.
- [110] L. Yu, Y.-H. Lee, X. Ling, E. J. Santos, Y. C. Shin, Y. Lin, M. Dubey, E. Kaxiras, J. Kong, H. Wang, *et al.*, "Graphene/mos2 hybrid technology for large-scale two-dimensional electronics," *Nano letters*, vol. 14, no. 6, pp. 3055–3063, 2014.
- [111] H. Tian, Z. Tan, C. Wu, X. Wang, M. A. Mohammad, D. Xie, Y. Yang, J. Wang, L.-J. Li, J. Xu, *et al.*, "Novel field-effect schottky barrier transistors based on graphene-mos 2 heterojunctions," *Scientific reports*, vol. 4, no. 1, pp. 1–9, 2014.
- [112] H. Dong, C. Gong, R. Addou, S. McDonnell, A. Azcatl, X. Qin, W. Wang, W. Wang, C. L. Hinkle, and R. M. Wallace, "Schottky barrier height of pd/mos2 contact by large area photoemission spectroscopy," *ACS applied materials & interfaces*, vol. 9, no. 44, pp. 38977–38983, 2017.
- [113] H. S. Sen, H. Sahin, F. Peeters, and E. Durgun, "Monolayers of mos2 as an oxidation protective nanocoating material," *Journal of Applied Physics*, vol. 116, no. 8, p. 083508, 2014.
- [114] M. Velický and P. S. Toth, "From two-dimensional materials to their heterostructures: An electrochemist's perspective," *Applied Materials Today*, vol. 8, pp. 68–103, 2017.

- [115] Z. Xu, H. Yang, X. Song, Y. Chen, H. Yang, M. Liu, Q. Zhang, L. Liu, Y. Wang, *et al.*, “Topical review: Recent progress of charge density waves in 2d transition metal dichalcogenide-based heterojunctions and their applications,” *Nanotechnology*, 2021.
- [116] L. Kou, Y. Ma, Z. Sun, T. Heine, and C. Chen, “Two-dimensional topological insulators: Progress and prospects,” *The journal of physical chemistry letters*, vol. 8, no. 8, pp. 1905–1919, 2017.
- [117] W. Y. Yun-Ben Wu, T.-B. Wang, X.-H. Deng, and J.-T. Liu, “Broadband perfect light trapping in the thinnest monolayer graphene-mos2 photovoltaic cell,”
- [118] W. Zhang, Q. Wang, Y. Chen, Z. Wang, and A. T. Wee, “Van der waals stacked 2d layered materials for optoelectronics,” *2D Materials*, vol. 3, no. 2, p. 022001, 2016.
- [119] M. Yankowitz, Q. Ma, P. Jarillo-Herrero, and B. J. LeRoy, “van der waals heterostructures combining graphene and hexagonal boron nitride,” *Nature Reviews Physics*, vol. 1, no. 2, pp. 112–125, 2019.
- [120] W. N. Hansen and G. J. Hansen, “Standard reference surfaces for work function measurements in air,” *Surface science*, vol. 481, no. 1-3, pp. 172–184, 2001.
- [121] A. Axt, I. M. Hermes, V. W. Bergmann, N. Tausendpfund, and S. A. Weber, “Know your full potential: Quantitative kelvin probe force microscopy on nanoscale electrical devices,” *Beilstein journal of nanotechnology*, vol. 9, no. 1, pp. 1809–1819, 2018.
- [122] E. G. Castanon, A. F. Scarioni, H. W. Schumacher, S. Spencer, R. Perry, J. A. Vicary, C. A. Clifford, and H. Corte-León, “Calibrated kelvin-probe force microscopy of 2d materials using pt-coated probes,” *Journal of Physics Communications*, vol. 4, no. 9, p. 095025, 2020.
- [123] S. Choi, Z. Shaolin, and W. Yang, “Layer-number-dependent work function of mos 2 nanoflakes,” *Journal of the Korean Physical Society*, vol. 64, no. 10, pp. 1550–1555, 2014.
- [124] L. Britnell, R. M. Ribeiro, A. Eckmann, R. Jalil, B. D. Belle, A. Mishchenko, Y.-J. Kim, R. V. Gorbachev, T. Georgiou, S. V. Morozov, *et al.*, “Strong light-matter interactions in heterostructures of atomically thin films,” *Science*, vol. 340, no. 6138, pp. 1311–1314, 2013.
- [125] T. Pandey, A. P. Nayak, J. Liu, S. T. Moran, J.-S. Kim, L.-J. Li, J.-F. Lin, D. Akinwande, and A. K. Singh, “Pressure-induced charge transfer doping of

- monolayer graphene/mos2 heterostructure,” *Small*, vol. 12, no. 30, pp. 4063–4069, 2016.
- [126] M. Ishigami, J. Chen, W. Cullen, M. Fuhrer, and E. Williams, “Atomic structure of graphene on sio<sub>2</sub>,” *Nano letters*, vol. 7, no. 6, pp. 1643–1648, 2007.
- [127] C. H. Lui, L. Liu, K. F. Mak, G. W. Flynn, and T. F. Heinz, “Ultraflat graphene,” *Nature*, vol. 462, no. 7271, pp. 339–341, 2009.
- [128] J. V. Pondick, J. M. Woods, J. Xing, Y. Zhou, and J. J. Cha, “Stepwise sulfurization from moo<sub>3</sub> to mos<sub>2</sub> via chemical vapor deposition,” *ACS Applied Nano Materials*, vol. 1, no. 10, pp. 5655–5661, 2018.
- [129] M. SUGIOKA and F. KIMURA, “Oxidation and reduction of molybdenum disulfide catalyst and their effects on the decomposition of 2-propanol,” *Journal of The Japan Petroleum Institute*, vol. 28, no. 4, pp. 306–311, 1985.
- [130] D. Ma, Q. Wang, T. Li, C. He, B. Ma, Y. Tang, Z. Lu, and Z. Yang, “Repairing sulfur vacancies in the mos<sub>2</sub> monolayer by using co, no and no<sub>2</sub> molecules,” *Journal of Materials Chemistry C*, vol. 4, no. 29, pp. 7093–7101, 2016.
- [131] P. Chow, “Jacobs–gedrim rb, gao j, lu t–m, yu b, terrones h, koratkar n,” *Defect-Induced Photoluminescence in Monolayer Semiconducting Transition Metal Dichalcogenides. ACS Nano*, vol. 9, no. 2, pp. 1520–1527, 2015.
- [132] J. Li, S. Hu, S. Wang, H. Kang, Z. Chen, S. Zhao, Y. Zhang, Y. Sui, and G. Yu, “The degradation of cvd-grown mos<sub>2</sub> domains in atmospheric environment,” *Materials Letters*, vol. 290, p. 129421, 2021.
- [133] M. Erementchouk, M. Khan, and M. N. Leuenberger, “Optical signatures of states bound to vacancy defects in monolayer mos<sub>2</sub>,” *Physical Review B*, vol. 92, no. 12, p. 121401, 2015.
- [134] S. Tongay, J. Zhou, C. Ataca, J. Liu, J. S. Kang, T. S. Matthews, L. You, J. Li, J. C. Grossman, and J. Wu, “Broad-range modulation of light emission in two-dimensional semiconductors by molecular physisorption gating,” *Nano letters*, vol. 13, no. 6, pp. 2831–2836, 2013.
- [135] S. Mouri, Y. Miyauchi, and K. Matsuda, “Tunable photoluminescence of monolayer mos<sub>2</sub> via chemical doping,” *Nano letters*, vol. 13, no. 12, pp. 5944–5948, 2013.
- [136] J. Ye, Y. J. Zhang, R. Akashi, M. S. Bahramy, R. Arita, and Y. Iwasa, “Superconducting dome in a gate-tuned band insulator,” *Science*, vol. 338, no. 6111, pp. 1193–1196, 2012.

- [137] T. Granzier-Nakajima, K. Fujisawa, V. Anil, M. Terrones, and Y.-T. Yeh, “Controlling nitrogen doping in graphene with atomic precision: Synthesis and characterization,” *Nanomaterials*, vol. 9, no. 3, p. 425, 2019.
- [138] D. Pierucci, H. Henck, Z. Ben Aziza, C. H. Naylor, A. Balan, J. E. Rault, M. G. Silly, Y. J. Dappe, F. Bertran, P. Le Fèvre, *et al.*, “Tunable doping in hydrogenated single layered molybdenum disulfide,” *ACS nano*, vol. 11, no. 2, pp. 1755–1761, 2017.
- [139] A. Molle, F. Fabbri, D. Campi, A. Lamperti, E. Rotunno, E. Cinquanta, L. Lazarini, D. Kaplan, V. Swaminathan, M. Bernasconi, *et al.*, “Evidence of native cs impurities and metal–insulator transition in mos2 natural crystals,” *Advanced Electronic Materials*, vol. 2, no. 6, p. 1600091, 2016.
- [140] A. C. Gadelha, A. R. Cadore, L. Lafeta, A. M. de Paula, L. M. Malard, R. G. Lacerda, and L. C. Campos, “Local photodoping in monolayer mos2,” *Nanotechnology*, vol. 31, no. 25, p. 255701, 2020.
- [141] R. Rao, V. Carozo, Y. Wang, A. E. Islam, N. Perea-Lopez, K. Fujisawa, V. H. Crespi, M. Terrones, and B. Maruyama, “Dynamics of cleaning, passivating and doping monolayer mos2 by controlled laser irradiation,” *2D Materials*, vol. 6, no. 4, p. 045031, 2019.
- [142] I. E. Jacobs and A. J. Moulé, “Controlling molecular doping in organic semiconductors,” *Advanced Materials*, vol. 29, no. 42, p. 1703063, 2017.
- [143] J. S. Ross, S. Wu, H. Yu, N. J. Ghimire, A. M. Jones, G. Aivazian, J. Yan, D. G. Mandrus, D. Xiao, W. Yao, *et al.*, “Electrical control of neutral and charged excitons in a monolayer semiconductor,” *Nature communications*, vol. 4, no. 1, pp. 1–6, 2013.
- [144] K. F. Mak, K. He, C. Lee, G. H. Lee, J. Hone, T. F. Heinz, and J. Shan, “Tightly bound trions in monolayer mos 2,” *Nature materials*, vol. 12, no. 3, pp. 207–211, 2013.
- [145] I. Kriegel, N. J. Borys, K. Zhang, A. W. Jansons, B. M. Crockett, K. M. Koskela, E. S. Barnard, E. Penzo, J. E. Hutchison, J. A. Robinson, *et al.*, “Contactless photo-induced carrier density control in nanocrystal mos2 hybrids,” *arXiv preprint arXiv:1810.05385*, 2018.
- [146] I. Sharma and B. R. Mehta, “Kpfm and cafm based studies of mos2 (2d)/ws2 heterojunction patterns fabricated using stencil mask lithography technique,” *Journal of Alloys and Compounds*, vol. 723, pp. 50–57, 2017.

- [147] W. H. Chae, J. D. Cain, E. D. Hanson, A. A. Murthy, and V. P. Dravid, “Substrate-induced strain and charge doping in cvd-grown monolayer mos<sub>2</sub>,” *Applied Physics Letters*, vol. 111, no. 14, p. 143106, 2017.
- [148] O. K. Le, V. Chihaiia, V. Van On, *et al.*, “N-type and p-type molecular doping on monolayer mos<sub>2</sub>,” *RSC Advances*, vol. 11, no. 14, pp. 8033–8041, 2021.
- [149] K. Kostarelos and K. S. Novoselov, “Graphene devices for life,” *Nature nanotechnology*, vol. 9, no. 10, pp. 744–745, 2014.
- [150] A. Bolotsky, D. Butler, C. Dong, K. Gerace, N. R. Glavin, C. Muratore, J. A. Robinson, and A. Ebrahimi, “Two-dimensional materials in biosensing and healthcare: from in vitro diagnostics to optogenetics and beyond,” *ACS nano*, vol. 13, no. 9, pp. 9781–9810, 2019.
- [151] X. Zhu, R. Ding, Z. Wang, Y. Wang, X. Guo, Z. Song, Z. Wang, and M. Dong, “Recent advances in synthesis and biosensors of two-dimensional mos<sub>2</sub>,” *Nanotechnology*, vol. 30, no. 50, p. 502004, 2019.
- [152] A. Daus, S. Vaziri, V. Chen, Ç. Koroğlu, R. W. Grady, C. S. Bailey, H. R. Lee, K. Schauble, K. Brenner, and E. Pop, “High-performance flexible nanoscale transistors based on transition metal dichalcogenides,” *Nature Electronics*, pp. 1–7, 2021.
- [153] C.-W. Yen, H. de Puig, J. O. Tam, J. Gómez-Márquez, I. Bosch, K. Hamad-Schifferli, and L. Gehrke, “Multicolored silver nanoparticles for multiplexed disease diagnostics: distinguishing dengue, yellow fever, and ebola viruses,” *Lab on a Chip*, vol. 15, no. 7, pp. 1638–1641, 2015.
- [154] H. Lee, T. K. Choi, Y. B. Lee, H. R. Cho, R. Ghaffari, L. Wang, H. J. Choi, T. D. Chung, N. Lu, T. Hyeon, *et al.*, “A graphene-based electrochemical device with thermoresponsive microneedles for diabetes monitoring and therapy,” *Nature nanotechnology*, vol. 11, no. 6, pp. 566–572, 2016.
- [155] B. Zhang, B. A. Pinsky, J. S. Ananta, S. Zhao, S. Arulkumar, H. Wan, M. K. Sahoo, J. Abeynayake, J. J. Waggoner, C. Hopes, *et al.*, “Diagnosis of zika virus infection on a nanotechnology platform,” *Nature medicine*, vol. 23, no. 5, pp. 548–550, 2017.
- [156] P. V. Kolesnichenko, Q. Zhang, C. Zheng, M. S. Fuhrer, and J. A. Davis, “Multidimensional analysis of excitonic spectra of monolayers of tungsten disulphide: toward computer-aided identification of structural and environmental perturbations of 2d materials,” *Machine Learning: Science and Technology*, vol. 2, no. 2, p. 025021, 2021.

- [157] M. Norouzi, V. Yathindranath, J. A. Thliveris, B. M. Kopec, T. J. Siahaan, and D. W. Miller, “Doxorubicin-loaded iron oxide nanoparticles for glioblastoma therapy: A combinational approach for enhanced delivery of nanoparticles,” *Scientific reports*, vol. 10, no. 1, pp. 1–18, 2020.
- [158] J. Chen, C. Qian, P. Ren, H. Yu, X. Kong, C. Huang, H. Luo, and G. Chen, “Light-responsive micelles loaded with doxorubicin for osteosarcoma suppression,” *Frontiers in Pharmacology*, vol. 12, p. 1378, 2021.
- [159] Y. Zhong, F. Meng, C. Deng, X. Mao, and Z. Zhong, “Targeted inhibition of human hematological cancers in vivo by doxorubicin encapsulated in smart lipoid acid-crosslinked hyaluronic acid nanoparticles,” *Drug delivery*, vol. 24, no. 1, pp. 1482–1490, 2017.
- [160] Y. Inouye and S. Kawata, “Near-field scanning optical microscope with a metallic probe tip,” *Optics letters*, vol. 19, no. 3, pp. 159–161, 1994.
- [161] H. Wang, L. Wang, D. S. Jakob, and X. G. Xu, “Tomographic and multimodal scattering-type scanning near-field optical microscopy with peak force tapping mode,” *Nature communications*, vol. 9, no. 1, pp. 1–11, 2018.
- [162] S. Catalán-Gómez, M. Briones, S. Cortijo-Campos, T. García-Mendiola, A. de Andrés, S. Garg, P. Kung, E. Lorenzo, J. L. Pau, and A. Redondo-Cubero, “Breast cancer biomarker detection through the photoluminescence of epitaxial monolayer mos 2 flakes,” *Scientific Reports*, vol. 10, no. 1, pp. 1–9, 2020.
- [163] S. Barja, S. Refaely-Abramson, B. Schuler, D. Y. Qiu, A. Pulkin, S. Wickenburg, H. Ryu, M. M. Ugeda, C. Kastl, C. Chen, *et al.*, “Identifying substitutional oxygen as a prolific point defect in monolayer transition metal dichalcogenides,” *Nature communications*, vol. 10, no. 1, pp. 1–8, 2019.